COMPUTATIONAL FRAMEWORK FOR MESO AND MACROSCALE ANALYSIS OF STRUCTURAL MASONRY

By KIANOOSH KOOCHEKI, B.Sc., M.Sc.

A Thesis Submitted to the School of Graduate Studies in Partial Fulfilment of the Requirements for the Degree Doctor of Philosophy

McMaster University DOCTOR OF PHILOSOPHY (2023) Hamilton, Ontario

(Civil Engineering)

TITLE: Computational Framework for Meso and Macroscale Analysis of Structural Masonry AUTHOR: Kianoosh Koocheki, B.Sc. (Tabriz University), M.Sc. (Sharif University of Technology), M.Sc. (University of Nebraska-Lincoln) SUPERVISORS: Professors S. Pietruszczak and P. Guo NUMBER OF PAGES: viii, 87

Abstract

The present research involves the development of a computational framework for numerical analysis of large-scale masonry structures. The main challenges in the analysis of existing structures of historic or strategic importance are the lack of information on the macroscale behaviour of masonry and the high computational cost of mesoscale analysis. The former requires extensive experimental programs that are virtually impossible without significantly affecting the structural integrity of the existing buildings. The latter, i.e. the mesoscale approach, requires only information on the behaviour of masonry constituents; however, it cannot be applied to analysis of structures that span hundreds of meters due to the required computational effort. To address these challenges, first a simplified mesoscale framework was developed incorporating an embedded discontinuity approach to model discrete crack initiation and propagation through masonry constituents. The approach enables the use of a simple unstructured finite element mesh and is computationally accurate and efficient. The proposed framework was validated against various experimental investigations on small-scale masonry assemblages. The second part of the research involved the development of a macroscale formulation for modelling masonry as a continuum with an underlying microstructure that exhibits anisotropic deformation and orientation-dependent strength characteristics. The identification of the constitutive parameters for the macroscale model was accomplished by simulating a series of biaxial and uniaxial tension-compression tests on masonry panels at different orientation of bed joints. Since the macroscale strength properties are highly dependent on the arrangement of masonry constituents and their individual

strength properties, changing any of these parameters requires a repetition of the entire numerical procedure. To address this challenge, a series of artificial neural networks was developed that can predict the macroscale strength and deformation properties of masonry based on the mechanical properties of constituents. In addition, another neural network was developed to assess the average orientation of macrocracks at the onset of failure at the macroscale. The results of the developed macroscale framework were compared with the mesoscale approach for analysis of a large-scale masonry wall.

Acknowledgements

The author wishes to extend his greatest appreciation and gratitude to the Ph.D. supervisors, Drs. S. Pietruszczak and P. Guo, for providing their immense support and valuable experience during the course of the research and studies, and their support during important career decisions.

The author would also like to thank the Ph.D. supervisory committee members, Drs. S. Chidiac and S. Na for providing valuable feedback and discussions during the annual committee meetings.

Co-authorship and Contributions:

The present thesis is prepared in the “sandwich” format with regulations indicated by the School of Graduate Studies. The publication status and co-authorship details of the papers are as follows.

Paper I:

A computational framework for meso and macroscale analysis of structural masonry.

Koocheki, K., Pietruszczak, S., Haghighat, E., 2022.
International Journal of Solid and Structures, 236–237, 111342.
https://doi.org/10.1016/j.ijsolstr.2021.111342

K. Koocheki implemented the constitutive law with embedded discontinuity for modeling the response of masonry at the mesoscale. He also developed and implemented the UMAT subroutine for the macroscale analysis and prepared the first draft of the manuscript. At all stages of work, the key aspects of the formulation were discussed with Dr. S. Pietruszczak. Dr. E. Haghighat was consulted on implementation of the level-set method and crack tracing algorithm. Dr. S. Pietruszczak revised and submitted the manuscript.

Paper II:

Numerical analysis of large masonry structures: bridging meso and macro scales via artificial neural networks

K. Koocheki, S. Pietruszczak
Computers and Structures, [under revision]

K. Koocheki developed and implemented the ANN codes for prediction of macroscale properties of masonry. He conducted the numerical simulations at the macro and mesoscales and prepared a draft of the paper. The research developments were supervised by with Dr. S. Pietruszczak who revised and submitted the final manuscript.

Paper III:
Mesoscale analysis of fracture process in brick masonry structures

K. Koocheki, S. Pietruszczak
Journal of Mathematics and Mechanics of Solids [under review]

K. Koocheki implemented the mesoscale formulation and expanded the user material subroutine capabilities. He conducted the numerical simulations and prepared a draft of the paper. The research developments were supervised by with Dr. S. Pietruszczak who revised and submitted the final manuscript.

Table of Contents

1. Introduction

1.1. Motivation and Scope of Study

One of the oldest structural materials that has become a part of the cultural and historical heritage of many countries is masonry. Over the past centuries, the engineers have constructed complex structures that withstand the test of time and natural hazards. For structures of high strategic importance or historical significance, an in-depth understanding of their mechanical behaviour is an imperative aspect of the maintenance and rehabilitation under potential natural or human-made hazards. However, as shown by years of research in this field, this is not a simple task due to the complexities that arise in predicting the mechanical response under the actual loading conditions.

Even though the geometry of the structure and the arrangement of masonry units can have a significant effect on the mechanical behaviour, there are distinguishable and frequently occurring mechanisms that are predominantly present under typical loading conditions. Those include the onset and propagation of damage along the brick-mortar interfaces, which are the weakest link in the system. In some cases, the cracks may also form within the brick and penetrate through the mortar joints forming a fracture mechanism that triggers the collapse of the structure.

Different deformation and strength properties of constituents and their interactions are the main reasons why the masonry, as a composite material, exhibits strongly anisotropic behaviour. At the macroscale, the masonry is stronger in compression than it is in tension, resulting in good performance in the presence of significant gravitational loads. This

characteristic, however, makes masonry structures susceptible to lateral loads which are usually present during seismic events or blast loads such as explosions.

The variety of local fracture modes at the level of constituents, which include brick-mortar bond sliding or separation, shear or tensile crack propagation inside the bricks, and fracture of mortar joints, render the accurate prediction of mechanical response of masonry at a structural level a complex and difficult challenge. A number of different methodologies for computational analysis of structural masonry have been pursued in the last few decades. The main factors in assessing the suitability of a given method are the amount of information available with regards to mechanical characteristics of the constituents, which can be difficult to obtain in case of existing structures, the dimensional scale of the problem which directly affects the computational cost, and the required input data which depends on the methodology of choice.

Given the ever-increasing capability of computational resources, methods such as finite element analysis have proven to be an effective approach for predicting the nonlinear mechanical response of masonry structures. In order to capture the localization of deformation, which is the fons et origo of the complex nonlinear behaviour of masonry, different approaches such as fracture mechanics, damage mechanics, and plasticity theory have been implemented. They all have their own advantages and drawbacks that need to be taken into account considering the nature of the problem and the data available for a given project.

Computational approaches for analysis of masonry can also be categorized based on the scale of the problem. For small structures and masonry assemblages, *mesoscale* approach is usually taken in which the constituents and their interfaces are modeled individually. In order to yield accurate results, this approach requires the availability of mechanical properties of masonry components as well as the strength properties of the brick-mortar bond. Moreover, the localized deformation within the brick units, which is associated with strain-softening response, may be considered in a discrete or smeared sense depending on the method of choice.

The drawback of mesoscale approach is the high computational cost which becomes a prohibitive factor as the size of the problem increases. In such cases, *macroscale* approaches are used where the masonry is considered as a homogenous anisotropic continuum. The macroscale approach is computationally efficient but is phenomenological in nature, requiring a significant amount of information on the stress-strain response of masonry assemblages large enough (with respect to the size of constituents) to be considered a homogenized medium. Conventionally, this information is obtained through laboratory experiments on masonry panels with loading conditions involving a uniform stress applied at the boundaries of the specimen. The complete formulation of a macroscale constitutive law requires the anisotropic elastic and strength properties of masonry which are obtained through multiple experiments corresponding to different orientations of material axes.

Besides the fact that laboratory experiments are expensive, time consuming, and prone to human errors, another challenging factor in case of existing structures is obtaining proper

samples for multiple experiments without affecting the integrity of the structure. This is an impossible task, especially for historic structures and buildings with strategically sensitive applications. In these cases, only small samples can be extracted which may be suitable to define the properties of constituents, but not the response at the macroscale.

The apparent gap between the mesoscale and macroscale approaches can be bridged through different homogenization techniques, e.g. by considering masonry as a periodic medium or by considering a combination of constituents as a representative elementary volume (REV). Additionally, multiscale approaches may also be employed where the macroscale stress-strain response is obtained by solving the correspondent boundary value problem on a smaller scale. The latter approach is rigorous but computationally expensive in case of large-scale structures.

Given the state-of-the-art methods and the present challenges, the purpose of this study is to develop a computational framework for numerical analysis of large masonry structures using limited input data incorporating the mechanical characteristics of masonry constituents. The main objectives of this task can be summarized as follows:

- Development of a mesoscale approach where discrete crack formation and propagation in masonry constituents is captured by embedding the discontinuities of deformation gradient field in the constitutive laws implemented in finite element analysis.

- Development of a macroscale approach in which masonry is considered as a homogenous continuum with an underlying *microstructure* that describes the anisotropic elastoplastic behaviour.
- Implementing Machine Learning methods that take the constituent properties as input and predict the required information for the description of homogenized anisotropic characteristics used in the macroscale approach.

1.2. Organization of the thesis

The present work is organized in the format of a "sandwich thesis" in accordance with McMaster University School of Graduate Studies regulations.

Chapter 2 (Paper I) introduces both the meso and macroscale framework for analysis of masonry structures and addresses their implementation in finite element (FE) code. The mesoscale analysis includes discrete tracing of crack propagation through brick-mortar interfaces as well as the brick units. Laboratory experiments available in literature are used as a benchmark for verification of the methodology. The macroscale approach incorporates the notion of *microstructure tensor* to describe the orientation-dependent strength characteristics of masonry. The material parameters/functions appearing in this approach are identified by conducting the mesoscale analysis of masonry panels subjected to biaxial tension-compression at different orientation of the bed joint. Thus, the mesoscale analysis serves as a bridge for upscaling to the macrolevel.

Chapter 3 (Paper II) presents the methodology for analyzing large scale masonry structures. The approach incorporates an inelastic macroscopic framework coupled with a series of artificial neural networks (ANNs). The latter serve the purpose of estimating the equivalent elastic properties of masonry from those of the constituents, the ultimate strength at different loading conditions and different orientation of material axes, as well as the average inclination of macrocracks that form at the onset of localization. The ANNs are trained using the data generated through a mesoscale FE analysis. A numerical example is provided involving analysis of a large masonry shear wall with openings. The results of macroscale approach are compared with those based on a detailed mesoscale model.

Chapter 4 (Paper III) provides a comprehensive study on the process of fracture initiation and propagation in small scale masonry structures. A simplified approach is used whereby the brick-mortar interfaces are embedded in the adjacent intact material. The accuracy of this approximation is assessed by comparing the results of uniaxial tension and biaxial tension-compression on masonry panels with those conducted using a detailed FE model that includes discretization of bricks, mortar, and incorporates the interface elements. An extensive numerical study is then provided that involves simulation of various experimental tests conducted on small masonry assemblages as well as full-scale masonry walls, and the results are compared with experimental data.

International Journal of Solids and Structures 236-237 (2022) 111342

Contents lists available at ScienceDirect

International Journal of Solids and Structures

journal homepage: www.elsevier.com/locate/ijsolstr

A computational framework for meso and macroscale analysis of structural masonry

K. Koocheki [a], S. Pietruszczak [a,*], E. Haghighat [b]

[a] McMaster University, Hamilton, ON, Canada
[b] University of British Columbia, Vancouver, BC, Canada

ARTICLE INFO

Keywords:
Brick masonry
Discrete crack propagation
Anisotropy
Failure criterion

ABSTRACT

In this study a computational framework is outlined for modeling the mechanical response of structural masonry at both meso and macroscale. The mesoscale approach accounts for the presence of distinct constituents (i.e., bricks and mortar joints) and their geometric arrangement. A constitutive law with embedded discontinuity, combined with the level-set approach, is used to model the onset and discrete propagation of localized damage in these constituents. The approach is verified against a range of experimental data published in the literature. It is shown that the proposed framework can adequately predict the load-deformation response, as well as the fracture pattern under combined loading conditions. The macroscale approach incorporates the notion of anisotropy parameter whose value depends on the orientation of the principal stress axes in relation to the axes of material symmetry. The material parameters/function appearing in this approach are identified from the 'virtual data' generated by a mesoscale analysis of masonry panels subjected to biaxial tension–compression at different orientations of the bed joint. Thus, the mesoscale considerations serve as a bridge for upscaling to the macrolevel.

1. Introduction

Numerical analysis of masonry structures can be conducted at either meso or macroscale. The former approach is suitable for smaller scale structures (e.g., shear walls, reduced scale models, etc.). For large structures (buildings, arch bridges, etc.), however, examining individual components (i.e., units/joints) and their interaction would be computationally very costly. Therefore, a more reasonable approach is that in which the masonry is considered as a continuum with a microstructure.

In engineering practice, the design and retrofit of masonry structures follows a set of guidelines provided by different building codes. The methodologies employed in these codes, i.e. limit state design and/or empirical methods, are quite simplistic. They do not address the basic issues that govern the mechanical response of masonry at the macroscale, such as the anisotropy of strength and deformation properties, discrete propagation of damage, environmental degradation, etc. Thus, although the general guidelines are useful, they are primarily qualitative and cannot be perceived as a reliable mechanical assessment, particularly when dealing with structures of a strategic importance that often have a complex geometry.

A better representation of the behaviour of structural masonry may be obtained by conducting the finite element (FEM) analysis. In recent years this has become a standard in the engineering design process. For the *mesoscale* simulations, the constituents themselves (i.e. units and mortar joints) may be considered as isotropic (Minga et al., 2018). In this case, the primary difficulty is to deal with the notion of localized deformation. The latter involves the presence of discontinuities in the displacement field or its gradient, referred to as *strong* or *weak* discontinuities (Simo et al., 1993), and is associated with the strain-softening response. In this case, the use of classical continuum approaches, which do not incorporate any measure of internal scale, results in a spurious mesh-dependency of the solution. In order to remedy the problem, the constitutive equations have been enhanced to incorporate non-local theories (Bažant & Jirásek, 2002; Jirásek, 2004) or visco-plastic regularization (Needleman, 1988; Niazi et al., 2012). Both these approaches, however, have limitations that stem from ambiguity in specifying the characteristic length and/or the viscosity parameter, which are not uniquely defined. Moreover, such continuum enhancements do not explicitly incorporate the rate form of traction– displacement discontinuity relation for the fracture zone, which is intrinsic in describing the softening phenomenon.

* Corresponding author.
E-mail address: pietrusz@mcmaster.ca (S. Pietruszczak).

https://doi.org/10.1016/j.ijsolstr.2021.111342
Received 25 March 2021; Received in revised form 23 September 2021; Accepted 2 November 2021
Available online 9 November 2021

An alternative way to deal with localized deformation is to invoke the embedded discontinuity approach (cf. Wells & Sluys, 2000, 2001; Jirasek and Zimmermann, 2001; Alfaiate et al., 2003; Benkemoun et al., 2010). In this approach, the discontinuities are embedded directly within a *finite element*. Both weak and strong discontinuities can be dealt with by addition of discontinuous functions to either strain or displacement fields of standard finite elements. In case of strong discontinuities, additional global degrees of freedom, i.e. nodal displacements associated with enhanced modes, are introduced and additional shape functions are added. There are different versions of the embedded discontinuity formulation including discrete approaches in which the crack path and the displacement jumps are continuous across element boundaries. The literature on this topic is very extensive and a comprehensive survey, which includes a comparison between various approaches, is provided in Jirásek (2000). Another enrichment technique, which has been developed in the context of partition of unity method, is the Extended Finite Element Method (XFEM) (Belytschko et al., 2001; Belytschko & Black, 1999; Moës & Belytschko, 2002). Again, a comparative study of this approach in relation to other FE techniques for capturing strong discontinuities is provided by Oliver et al. (2006).

Both the above-mentioned approaches are rigorous and have been applied to a broad spectrum of engineering problems. Their main limitation, particularly in case of XFEM, is a high computational cost that stems primarily from incorporation of additional degrees of freedom that account for the presence of discontinuities. The approach employed in this work is conceptually different in the sense that the velocity discontinuity is explicitly embedded in the *constitutive law*. The latter incorporates a length scale parameter, which is defined in an explicit manner. The approach was originally proposed in the early 1980′s (Pietruszczak and Mróz, 1981) and was later modified to redefine the internal length parameter (cf. Pietruszczak, 1999). Its implementation in the FEM platform is straightforward, as no enriched degrees of freedom are required. An enhanced version, which incorporates a discrete crack tracing scheme, is provided in Haghighat & Pietruszczak (2015, 2016). The last references also give a direct comparison of the numerical performance of this approach in relation to XFEM methodology.

The *macroscale* analysis requires the assessment of equivalent mechanical properties for a given type of masonry layout. This can be accomplished by application of the mathematical theories of homogenization. The latter have been applied in the context of both periodic (Sacco, 2009; Anthoine, 1997; De Buhan & De Felice, 1997; Pande et al., 1989) as well as non-periodic media (Cluni & Gusella, 2004) and a comprehensive review of different strategies is provided in Lourénço et al. (2007). The main difficulty in this approach is the assessment of properties in inelastic range, which requires a numerical homogenization. In this case, the simulations are carried out using a representative elementary volume (REV) from which the equivalent (i.e., volume averaged) properties are acquired (e.g., Van der Sluis et al., 2000). The computational homogenization techniques have also been extensively used in the context of multiscale modeling of heterogeneous materials with complex microstructures. The literature on this topic is very extensive and a concise review is provided, for example, in Geers et al. (2010). The approach comprises a multi-level finite element analysis, referred to as FE^2 scheme (cf. Smit et al., 1998; Feyel, 2003; Nguyen et al., 2011), which employs meshing at macro-level (entire structure) and micro-level (REVs). An application of this methodology to masonry, involving simulation of some material tests as well as a shear wall test, is provided by Massart et al. (2007). The approach is rigorous, but computationally very expensive and its application in the context of large-scale masonry structures is currently not feasible.

In general, the key issues in modeling the mechanical response of masonry at the macroscale involve a proper description of inherent anisotropy and, once again, the localized nature of damage. The anisotropy manifests itself in the directional dependence of strength and deformation properties. This has been evidenced by testing scaled masonry panels under biaxial load at different orientations of the bed joints (c.f. Drysdale & Khattab, 1995; Page, 1981; Page, 1983). The results of these tests provided a valuable information that has been employed to specify the conditions at failure. The existing formulations defining the phenomenologically based failure criteria usually incorporate linear and quadratic terms in stress components referred to principal material axes (e.g. Tsai & Wu, 1971). Examples of application of this class of criteria to structural masonry include the work of Lourénço et al. (1997) and Berto et al. (2002). A more rigorous approach is associated with incorporating the notion of a fabric tensor and establishing its correlation with the strength properties (Boehler & Sawczuk, 1977; Cowin, 1986). The disadvantage of the latter approach, however, is the fact that the general framework incorporates numerous material functions whose identification requires an elaborated experimental program which cannot be carried out for any practical engineering problem. A simplified and a more pragmatic methodology was introduced by Pietruszczak & Mroz (2001) whereby the classical isotropic criteria have been enhanced by incorporating the concept of a spatial distribution of strength parameters. Two different approaches have been developed, viz. a critical plane and a microstructure tensor approach. In the former, the failure criterion is expressed in terms of traction components, while the orientation of the localization plane is defined as a constrained optimization problem. In the approach incorporating the microstructure tensor, a scalar anisotropy parameter is introduced whose value is a function of relative orientation of the principal stress triad with respect to the eigenvectors of the microstructure tensor. The latter methodology has recently been applied by Pietruszczak and Mohammadi (2020) to define the macroscopic failure criterion using the experimental data reported by Page (1981, 1983).

This paper is a continuation of the work reported by Pietruszczak and Mohammadi (2020). Its primary focus is the development of a reliable computational scheme for the mesoscale analysis of structural masonry. The approach incorporates a novel technique for dealing with the bed and head joints, whose presence is accounted for by employing a constitutive law with embedded discontinuity (Haghighat & Pietruszczak, 2015). This allows the use of a simple structured mesh which significantly reduces the computational cost of analysis. The procedure also accounts for the onset of new macrocracks forming within the masonry units and the discrete tracing of their propagation by means of the level set technique. The purpose of this mesoscale approach is two-fold. First, such an approach can be used for an independent analysis of smaller scale masonry structures. At the same time, it can serve the purpose of generating a 'virtual data' for masonry panels tested at different orientations relative to the direction of loading. The latter information can then be employed in the context of specification of material functions required for the analysis of large masonry structures. Thus, the mesoscale considerations serve as a bridge for upscaling to the macroscale.

In the next section the mesoscale formulation and its numerical implementation are discussed. Subsequently, the framework is verified against some benchmark problems involving simulation of experimental tests on brick–mortar bond and masonry wallets. Later, a comprehensive study is provided investigating the fracture mechanism in masonry panels tested by Page (1981, 1983). Different loading conditions and different orientations of the panels are considered. Finally, the macroscale approach is outlined, and the results obtained from the mesoscale analysis are employed to identify the material functions appearing in the failure criterion incorporating the scalar anisotropy parameter.

2. Mesoscale formulation and its implementation

The mesoscale analysis of structural masonry requires the information on properties of constituents (bricks, mortar joints) and their geometric arrangement. The constituents themselves may be perceived as isotropic and, in the range of homogeneous deformation, their

mechanical properties can be described by standard continuum approaches. The weakest link in the structural masonry are the brick–mortar interfaces, which require a contact law relating the traction rate to velocity discontinuity. The failure of constituents is often linked with the onset and propagation of localized damage associated with unstable strain-softening response. The onset of localization is usually defined by invoking a stress or energy-based failure criterion or, in case of elastoplastic or damage-based idealization, it may be perceived as a bifurcation problem. The latter involves detection of singularity of the so-called *acoustic tensor* (Rudnicki & Rice, 1975) whose eigenvectors determine the orientation of fracture plane. In this work, the constituents themselves are considered as *elastic*-brittle. Note that there is no conceptual difficulty in considering the bricks/mortar as inelastic. However, in structural masonry the irreversible deformation at the macroscale is primarily due to sliding and separation along the interfaces, so that the former effects seem negligible. In this section, the details on mesoscale modeling are provided. The focus is on the description of deformation process in a domain intercepted by discontinuities, which is relevant for both brick units and interfaces, as the latter are treated as being embedded in the adjacent homogenous continuum.

2.1. Mathematical formulation in the presence of discontinuities

In the presence of localization, the average mechanical properties within a domain containing a fracture may be assessed by incorporating a constitutive law with embedded discontinuity (CLED, cf. Haghighat & Pietruszczak, 2015; Pietruszczak, 1999). For this purpose, consider a referential volume $\Delta\Omega$, which includes the intact parts $\Delta\Omega^+$ and $\Delta\Omega^-$, intercepted by a fractured region of surface area of $\Delta\Gamma_d$ and a negligible thickness (compared to other dimensions). In this case, the discontinuous velocity field $\boldsymbol{v}$ may be defined as a sum of two continuous functions $\widehat{\boldsymbol{v}}$ and $\widetilde{\boldsymbol{v}}$, combined with a discontinuous Heaviside step function $\mathcal{H}_{\Gamma_d}$ as

$$\boldsymbol{v} = \widehat{\boldsymbol{v}} + \mathcal{H}_{\Gamma_d}\widetilde{\boldsymbol{v}}; \quad [\![\boldsymbol{v}]\!] = \boldsymbol{v}^+ - \boldsymbol{v}^- = [\![\mathcal{H}_{\Gamma_d}]\!]\widetilde{\boldsymbol{v}} \tag{1}$$

where $[\![\boldsymbol{v}]\!]$ is the velocity jump across the localized zone. Using Eq. (1), the average velocity gradient in a referential volume $\Delta\Omega$ can be defined as

$$\begin{aligned}\nabla_{\mathbf{x}}\mathbf{v} &= \frac{1}{\Delta\Omega}\int_{\Delta\Omega}\nabla_{\mathbf{x}}\boldsymbol{v}\,\mathrm{d}\Omega \\ &= \frac{1}{\Delta\Omega}\int_{\Delta\Omega}\nabla_{\mathbf{x}}\widehat{\boldsymbol{v}}\,\mathrm{d}\Omega + \frac{1}{\Delta\Omega}\int_{\Delta\Omega^+}\nabla_{\mathbf{x}}\widetilde{\boldsymbol{v}}\,\mathrm{d}\Omega + \frac{1}{\Delta\Omega}\int_{\Delta\Gamma_d t_d}\left(\widetilde{\boldsymbol{v}}\otimes\nabla_{\mathbf{x}}\mathcal{H}_{\Gamma_d}\right)\mathrm{d}\Omega\end{aligned} \tag{2}$$

where

$$\nabla_{\mathbf{x}}\mathcal{H}_{\Gamma_d} = [\![\mathcal{H}_{\Gamma_d}]\!]\delta_{\Gamma_d}\mathbf{n} \tag{3}$$

Here, δ_{Γ_d} is the Dirac delta function and $\mathbf{n}$ is the outward normal to the discontinuity surface. Substituting Eq. (3) into Eq. (2) and using the second equation in (1) leads to

$$\begin{aligned}\nabla_{\mathbf{x}}\mathbf{v} \;&= \frac{1}{\Delta\Omega}\int_{\Delta\Omega}\nabla_{\mathbf{x}}\widehat{\boldsymbol{v}}\,\mathrm{d}\Omega + \frac{1}{\Delta\Omega}\int_{\Delta\Omega^+}\nabla_{\mathbf{x}}\widetilde{\boldsymbol{v}}\,\mathrm{d}\Omega \\ &\quad + \frac{1}{\Delta\Omega}\int_{\Delta\Gamma_d}[\![\boldsymbol{v}]\!]\otimes\mathbf{n}\,\mathrm{d}\Gamma_d\end{aligned} \tag{4}$$

The first two terms appearing on the right-hand side of Eq. (4) represent the volume average of the velocity gradient in the intact material, while the last term is proportional to the average value of $[\![\boldsymbol{v}]\!]\otimes\mathbf{n}$ over the crack surface area $\Delta\Gamma_d$, i.e

$$\begin{aligned}\nabla_{\mathbf{x}}\mathbf{v}^{(1)} &= \frac{1}{\Delta\Omega}\int_{\Delta\Omega}\nabla_{\mathbf{x}}\widehat{\boldsymbol{v}}\,\mathrm{d}\Omega + \frac{1}{\Delta\Omega}\int_{\Delta\Omega^+}\nabla_{\mathbf{x}}\widetilde{\boldsymbol{v}}\,\mathrm{d}\Omega; \\ \dot{\mathbf{g}}\otimes\mathbf{n} &= \frac{1}{\Delta\Gamma_d}\int_{\Delta\Gamma_d}[\![\boldsymbol{v}]\!]\otimes\mathbf{n}\,\mathrm{d}\Gamma_d\end{aligned} \tag{5}$$

The *symmetric* parts of these operators define the corresponding average strain rates. Thus, the total strain rate can be expressed as

$$\dot{\boldsymbol{\varepsilon}} = \dot{\boldsymbol{\varepsilon}}^{(1)} + \chi(\dot{\mathbf{g}}\otimes\mathbf{n})^s \tag{6}$$

where $\dot{\boldsymbol{\varepsilon}}^{(1)} = \left(\nabla_{\mathbf{x}}\mathbf{v}^{(1)}\right)^s$ is the average strain rate in the intact material, while the second term gives the contribution associated with the localized deformation. Here, χ^{-1} is a *length scale parameter* defined as the ratio of the referential volume to the surface area of the fractured region (i.e. $\chi^{-1} = \Delta\Omega/\Delta\Gamma_d$).

The velocity jump $\dot{\mathbf{g}}$ is determined by imposing the traction continuity condition across the localized region. Thus,

$$\dot{\mathbf{t}} - \mathbf{n}\cdot\dot{\boldsymbol{\sigma}} = \mathbf{K}\cdot\dot{\mathbf{g}} - \mathbf{n}\cdot\mathbb{D}\cdot\dot{\boldsymbol{\varepsilon}}^{(1)} = 0 \tag{7}$$

where $\mathbf{t}$ is the traction vector, $\mathbf{K}$ is the second order stiffness operator for the fractured zone, $\dot{\boldsymbol{\sigma}}$ is the macroscopic stress rate and $\mathbb{D}$ is the fourth-order elasticity tensor which defines the properties in the intact region. Combining the above equations and rearranging leads to the localization law

$$\dot{\mathbf{g}} = \left[(\mathbf{K} + \chi\mathbf{n}\cdot\mathbb{D}\cdot\mathbf{n})^{-1}\otimes\mathbf{n}\right] : [\mathbb{D} : \dot{\boldsymbol{\varepsilon}}] \tag{8}$$

Finally, using Eqs. (6) and (8), the constitutive relation is obtained as

$$\begin{aligned}\dot{\boldsymbol{\sigma}} &= \overline{\mathbb{D}} : \dot{\boldsymbol{\varepsilon}}; \\ \overline{\mathbb{D}} &= \left\{\mathbb{D} - \chi\mathbb{D} : \left[\mathbf{n}\otimes(\mathbf{K} + \chi\mathbf{n}\cdot\mathbb{D}\cdot\mathbf{n})^{-1}\otimes\mathbf{n}\right] : \mathbb{D}\right\}\end{aligned} \tag{9}$$

where $\overline{\mathbb{D}}$ is the equivalent tangential stiffness operator which depends on the properties of both constituents and the scale parameter χ, the latter defined at the element level based on the orientation and location of the macrocrack.

2.2. Modeling of constituents

2.2.1. Embedded brick–mortar interfaces

The approach advocated here for FEM analysis is to consider the interfaces as being embedded in the adjacent continuum. Thus, a simple structured mesh may be used, Fig. 1, in which the presence of joints is accounted for by employing standard FEM elements in which mechanical properties are defined by the constitutive law with embedded discontinuity (9). In this case, the discontinuity surface $\Delta\Gamma_d$ is explicitly identified with the brick–mortar interface, which represents the weakest

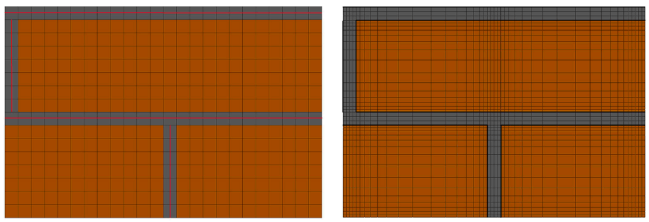

Fig. 1. FEM discretization of structural masonry (a) representation incorporating CLED (red line shows interfaces embedded within elements); (b) standard representation incorporating discretization of mortar joints together with interface elements (thick black lines). (For interpretation of the references to colour in this figure legend, the reader is referred to the web version of this article.)

link in the masonry architecture. Fig. 1a show a schematic discretization of a periodic unit with running bond pattern using the proposed methodology. At the same time, Fig. 1b depicts a typical mesh incorporating the physical presence of mortar joints. The latter requires a finer discretization employing a structured mesh together with a set of interface elements. Apparently, the advocated approach is bound to be computationally more efficient. In addition, the numerical problems inherent to the use of interface elements, such as ill-conditioning of the stiffness matrix, poor convergence of the solution and instability of the numerical integration of stress rate equations (cf. Villard, 1996), can be avoided.

The implementation of the proposed methodology requires the specification of the stiffness operator **K** appearing in the constitutive relation (9). In the present study, the properties of brick–mortar interface have been described using an elastic-strain softening idealization. In particular, the Coulomb failure function with tension cut-off zone has been employed, i.e.

$$F = \begin{cases} \tau - (c - \mu\sigma) & , \quad \sigma < \sigma_t \\ \sigma - \sigma_t & , \quad \sigma \geq \sigma_t \end{cases} \tag{10}$$

where $\mu = \tan\phi$, with ϕ being the friction angle, and σ, τ represent the magnitudes of normal and tangential components of the traction vector **t**. Here, $F < 0$ implies an elastic response, while in the plastic regime the degradation functions have been selected as

$$\begin{aligned} &\sigma_t = f_t \exp\left(-\frac{f_t}{G_f} g_n\right); \; c = c_o \exp(-\alpha g_t) \geq \mu\sigma_t; \\ &\mu = \mu_o + (\mu_r - \mu_o)\left(\frac{c_o - c}{c_o}\right) \end{aligned} \tag{11}$$

Here, the subscripts *o* and *r* refer to initial and residual values of c and μ, G_f the is tensile fracture energy release rate, α is a material parameter, while g_n and g_t are normal and shear components of accumulated *plastic* part of displacement jumps.

The equivalent stiffness operator $\overline{\mathbb{D}}$ is determined using Eq. (9), in which $\mathbb{D}$ defines the elastic properties of the adjacent continuum. Here, for $F < 0$ there is $\mathbf{K} = \mathbf{K}^e$, while for an active loading process **K** is established using functional forms (10) and (11). In the latter case, a standard plasticity procedure is followed, invoking additivity postulate together with the consistency condition. The framework employed here incorporated an associated flow rule in tension and non-associated (zero-dilatancy) rule in compression regime.

2.2.2. Brick units

The bricks have been also considered here as elastic prior to the onset of localization. The transition was defined via a standard Mohr-Coulomb criterion with Rankin's cut-off, which stipulates that in compression regime the macrocracks form at $\mp(45^\circ + \phi/2)$ with respect to the direction of minor principal stress, whereas in tension their direction is orthogonal to that of maximum tensile stress. The crack propagation process was simulated using the CLED framework, viz. Eq. (9). In the strain-softening regime, the representation analogous to that of eqs. (10)-(11) was employed. However, the degradation law for the friction coefficient was rephrased as

$$\mu = \mu_o + (\mu_r - \mu_o)\left(\frac{c_o - c}{c_o}\right); \; \mu_o = \frac{\tau - c_o}{\sigma} \tag{12}$$

Thus, in this case the parameter μ_o is not a material constant but is defined explicitly from the condition that, at the onset of localization, the components of traction vector satisfy $F = 0$, Eq. (10). Again, given the functional form (12), the stiffness operator **K**, Eq. (9), can be determined following the standard plasticity procedure.

As mentioned earlier, for structural masonry the failure mode typically involves fracture along the bed and head joints, whose orientation is defined *a priori*. However, for certain loading histories, the damage process may also involve the onset and propagation of fractures through the brick units. In such a case, a suitable algorithm for a discrete crack tracking is required. In this work, the geometry of propagating crack has been traced by employing the level-set method (Adalsteinsson & Sethian, 1999; Stolarska et al., 2001). The latter is a numerical technique used to represent the location of macrocracks, including the position of their tips. The approach provides information that is particularly useful when dealing with multiple fractures and/or intersecting cracks and allows to quickly locate the potential elements in the vicinity of crack tips, where the fracture is most likely to propagate. The benefits of level-set approach for tracing discrete discontinuities have been discussed extensively in several studies (cf. Stolarska et al., 2001, Belytschko et al., 2001).

According to this approach, a propagating discontinuity surface Γ_d can be defined as the zero level-set of a function $\phi(\mathbf{x}, t)$, i.e., $\Gamma_d = \{\mathbf{x} | \phi(\mathbf{x}, t) = 0\}$. Commonly, the signed distance function expressed as $\phi(\mathbf{x}) = sign\{\mathbf{n}\cdot(\mathbf{x} - \mathbf{x}_\Gamma)\}\min\|\mathbf{x} - \mathbf{x}_\Gamma\|$ is used as a level set function, and it has been employed here for tracing the crack path. The gradient of $\phi(\mathbf{x}, t)$ defines the direction normal to the fracture surface, which is required in implementation of CLED approach. A second level-set is often employed to trace crack tips (Stolarska et al., 2001). Combination of these two level-sets defines a potential zone for fracture propagation and permits tracking of the moving crack without numerical noise.

A schematic example of crack initiation and propagation in a discretized domain is shown in Fig. 2. The initial crack is assumed to pass through the centroid of the element, Fig. 2a, and is shown by the solid red line. The level set function is constructed in the domain, with the zero level-set as depicted by the dashed red line. Elements along the crack path are highlighted in yellow and the crack tip neighbour elements are highlighted in green. An iterative algorithm is then started in which the crack propagates through the crack path elements until equilibrium is reached. Fig. 2b shows the cracked elements (blue) and location of the crack inside the elements. The exact location of the crack in each element is determined using the intercept with the element boundary and the given crack orientation. The level set is updated in the proceeding increment and if stress conditions at the tip elements result in a change in crack direction, the potential elements engaged in further propagation of the cracked zone are identified, as shown in Fig. 2b.

3. Numerical implementation and verification of the mesoscale framework

3.1. Simulation of tests on brick–mortar bond

The first set of numerical examples pertains to simulation of the tensile and shear tests on brick–mortar bond as reported by Van der Pluijm (1997, 2000). The tests were displacement-controlled and

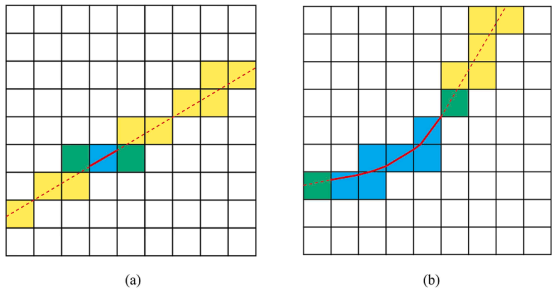

Fig. 2. (a) Schematic crack initiation and (b) Crack propagation involving a change in orientation. Dashed line shows the location of zero level set, solid red line and blue elements show crack location, green elements indicate crack tip, yellow elements identify potential elements for crack propagation. (For interpretation of the references to colour in this figure legend, the reader is referred to the web version of this article.)

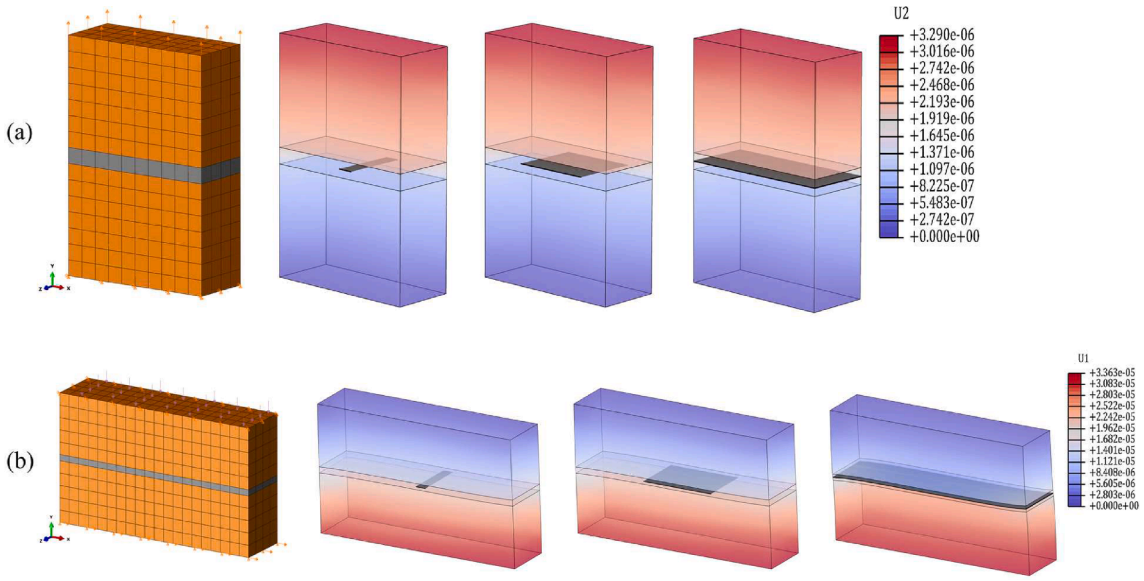

Fig. 3. FEM discretization and evolution of fracture pattern (black) superimposed on (a) vertical displacement field in tension and (b) horizontal displacement field in shear.

were performed on specimens of two brick units, with dimensions 200 × 100 × 50 mm (in shear) and 100 × 100 × 50 mm (in tension), separated by a bed joint. For shear tests, the specimens were subjected to normal stress of intensity between 0.1 and 1.0 MPa, and subsequently sheared by imposing the displacement parallel to the joint. The experimental program was comprehensive, as approx. 50 tests were conducted; however, the scatter of experimental data was significant (i.e., coefficient of variation of 20–40%).

The numerical analysis was conducted using a mesh incorporating 880 and 600 eight-node cubic elements in shear and tension, respectively. The geometry of the problem and the FEM discretization are shown in Fig. 3. For axial tension, the bottom of the specimen was fixed, and a uniform vertical displacement was applied at the top. For simulations of shear test, the top and the bottom of the sample were fixed in horizontal and vertical directions, respectively. The loading process consisted of applying a vertical force, after which the horizontal displacement was imposed at the bottom surface. The material parameters employed in the analysis are provided in Table 1. The values of these parameters were selected based on the data reported by Van der Pluijm (1993, 1997). Note that the experimental results do not include any explicit information on the material constants that govern the strain softening characteristics, viz. Eq. (11). Therefore, some parametric studies have been conducted on assessing their impact on the numerical predictions.

Table 1
Material parameters employed in numerical simulations.

	Brick	Brick-mortar bond
Young's Modulus, E (MPa)	15,000	N/A
Poisson's ratio, υ	0.15	N/A
Tensile Strength, f_t (MPa)	3.5	0.65
Angle of internal friction, ϕ (°)	30	36
Cohesion, c (MPa)	19	0.85
Bond normal stiffness, k_n (N/m)	N/A	1.7×10^8
Bond shear stiffness, k_t (N/m)	N/A	7.6×10^8

The main results of simulations are provided in Figs. 3-4. Fig. 3 depicts the evolution of damage along the brick–mortar interface superimposed on the displacement field. The corresponding mechanical characteristics, i.e. traction vs. displacement, are shown in Fig. 4. Here, Fig. 4a depicts the sensitivity of the post-peak response to the selected value of the tensile fracture energy release rate G_f, while Fig. 4b shows the shear characteristics at different values of the normal stress. For the latter case, the results correspond to $\alpha = 10{,}000\ \mathrm{m}^{-1}$, $\mu_r = 0.85\mu_o$, which gives a fairly close approximation to the experimental data.

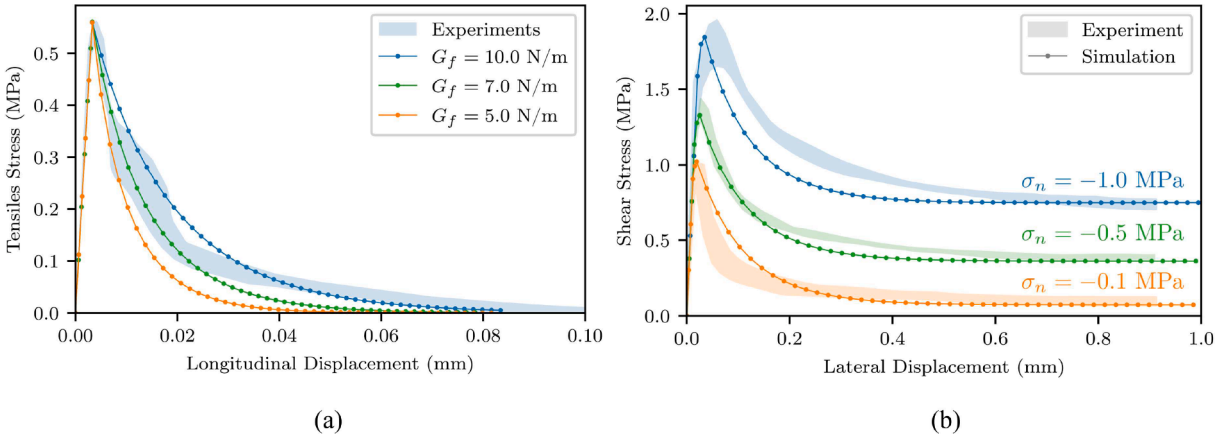

Fig. 4. Mechanical characteristics for the brick–mortar bond in (a) direct tension (influence of fracture energy release, G_f) and (b) shear (influence of normal stress).

Table 2
Material parameters employed in simulations of tensile tests of Backes (1985).

	Brick		Brick-mortar bond	
	Case I	Case II	Case I	Case II
Young's Modulus, E (MPa)	3500	2500	N/A	N/A
Poisson's ratio, υ	0.13	0.13	N/A	N/A
Tensile Strength, f_t (MPa)	0.9	1.44	0.12	0.19
Angle of internal friction, ϕ (°)	30	30	30	30
Cohesion, c (MPa)	2.5	1.5	0.25	0.15
Bond normal stiffness, k_n (N/m)	N/A	N/A	0.7×10^8	1.1×10^8
Bond shear stiffness, k_t (N/m)	N/A	N/A	3.2×10^8	3.8×10^8

3.2. Simulation of tensile tests on brick masonry wallets

In order to provide an insight into the fracture propagation mechanism through the masonry constituents, consider first an illustrative example which involves simulation of tensile tests performed by Backes (1985). The tests were conducted on square masonry wallets (490 × 490 × 113 mm) subjected to tension along the direction of bed joints. The analysis here is focused on simulation of two cases which involve two different sets of mechanical properties of constituents as shown in Table 2. Fig. 5a presents the 3D view and the FEM discretization of the wallets, while Figs. 5b-c show the evolution of fracture pattern. For both sets of properties, the tensile cracks initiate in the head joints. However, the further propagation pattern is affected by the relative values of the shear strength of bed joints and the tensile strength of bricks. A weaker shear strength of brick–mortar bond (e.g. 0.1 – 0.2 MPa) results in a zigzag pattern, while stronger shear bond strength (e.g. 0.2 – 0.9 MPa) leads to formation of tensile cracks inside the bricks. In the latter case, the fracture mode involves formation of a nearly vertical crack penetrating through the head joints and bricks.

Fig. 6 shows the corresponding average stress–strain characteristics. The results correspond to the fracture energy release rates (G_f) of 50 N/m and 10 N/m for the bricks and interface, respectively, while $\alpha = 15{,}000\ \mathrm{m}^{-1}$ for the bed joints. The predicted structural response at the macroscale is very consistent with the experimental data in terms of both the strength and the deformation response.

3.3. Simulation of biaxial tension–compression tests on structural masonry panels

In order to provide a comprehensive verification of the proposed methodology with respect to combined biaxial tension and compression loading, a set of experimental tests conducted by Dhanasekar et al. (1985) and Page (1983) has been simulated. The focus was on the prediction of fracture pattern and the ultimate load in a broad range of testing configurations. The experiments were conducted on square 0.36 m solid brick masonry panels constructed using half-scale units with dimensions of 115 × 35 × 50 mm. To achieve a uniform stress

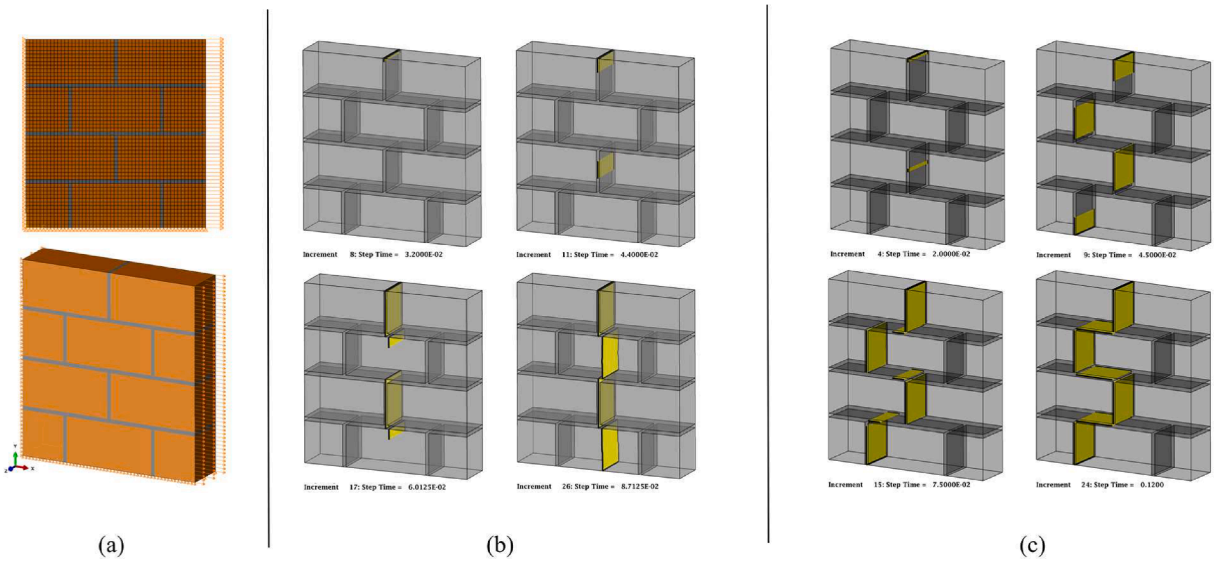

Fig. 5. Uniaxial tension parallel to bed joints: (a) FEM mesh and 3D view; (b) Crack propagation for Case I; (c) Crack pattern for Case II.

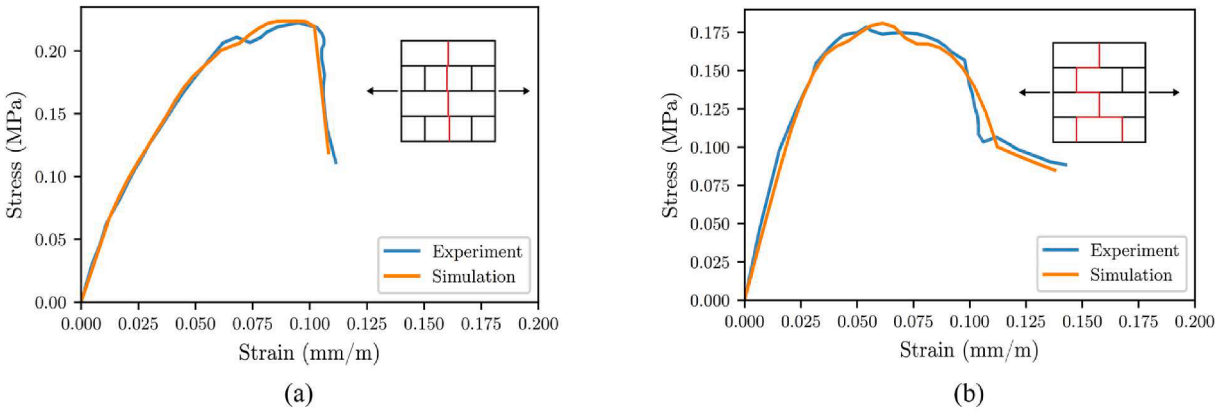

Fig. 6. Average stress–strain characteristics for (a) Case I; (b) Case II (experimental results after Backes (1985); recorded crack patterns are shown schematically).

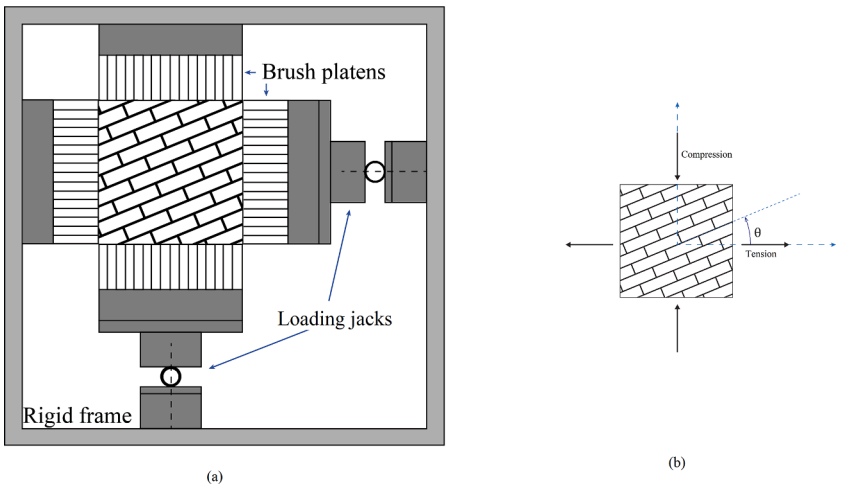

Fig. 7. Experimental setup of Page (1983) and different testing configurations.

distribution along the boundaries and to enable the application of tensile loading, a large number of closely stacked slender elements forming brush-like platens were glued individually to the boundaries of the panel, as illustrated in Fig. 7a. The loading program incorporated uniaxial as well as biaxial tension/compression at different orientations of the bed joints, as shown schematically in Fig. 7b. In all tests, the principal stress directions were fixed while the orientation of the masonry panel was varied. For the majority of tests, the fracture mode involved failure along the masonry joints; however, in some experiments incorporating biaxial loading conditions the onset and propagation of macrocracks within the brick units was also observed.

The geometry of the problem, the boundary conditions and the FEM mesh are shown in Fig. 8. A simple structured mesh, with a total of 15,120 eight-noded cubic elements, was employed in which the presence of brick–mortar bonds has again been accounted for using the CLED formulation. For simulation of uniaxial tests along and normal to bed joints, a displacement-controlled scheme was employed (Fig. 8a); while for other tests, the load-controlled procedure was implemented. The tests on inclined specimens were simulated by transforming the boundary tractions to the principal material axes and applying them as a uniformly distributed load along the respective boundaries, Fig. 8b.

The main challenge in validation of the present approach is a significant variability in the experimental assessment of ultimate load. This stems primarily from a high variation of brick–mortar bond strength as reported in Dhanasekar et al. (1985) and Page (1983). The latter varied between 0.07 and 0.28 MPa with an average of 0.13 MPa. As a result, the bearing capacity of the panel under uniaxial tension perpendicular to bed joints also varied significantly, i.e. between 0.18 and 0.32 MPa with a mean value of 0.24 MPa. An additional issue is incomplete information on properties of constituents. For example, in terms of strength properties of brick units, the only information provided was that on the range of values of compressive strength. Also, no data has been provided on the deformation characteristics of the brick–mortar bond. Given these limitations, some additional parametric studies have been conducted throughout this work. The actual set of material parameters employed in the analysis is provided in Table 3. Here, the properties that were varied through parametric studies (i.e. tensile/shear strength of brick–mortar bond and tensile strength of brick) are displayed in boldface.

Table 3
Material parameters employed in numerical simulations.

Properties	Brick	Brick-mortar bond
Young's Modulus, E (MPa)	6750	N/A
Poisson's ratio, υ	0.17	N/A
Tensile Strength, f_t (MPa)	**1.5**	**0.2**
Angle of internal friction, ϕ (°)	30	39
Cohesion, c (MPa)	4.35	**0.3**
Interface normal stiffness, k_n (N/m)	N/A	1.3×10^8
Interface shear stiffness, k_t (N/m)	N/A	6.2×10^8

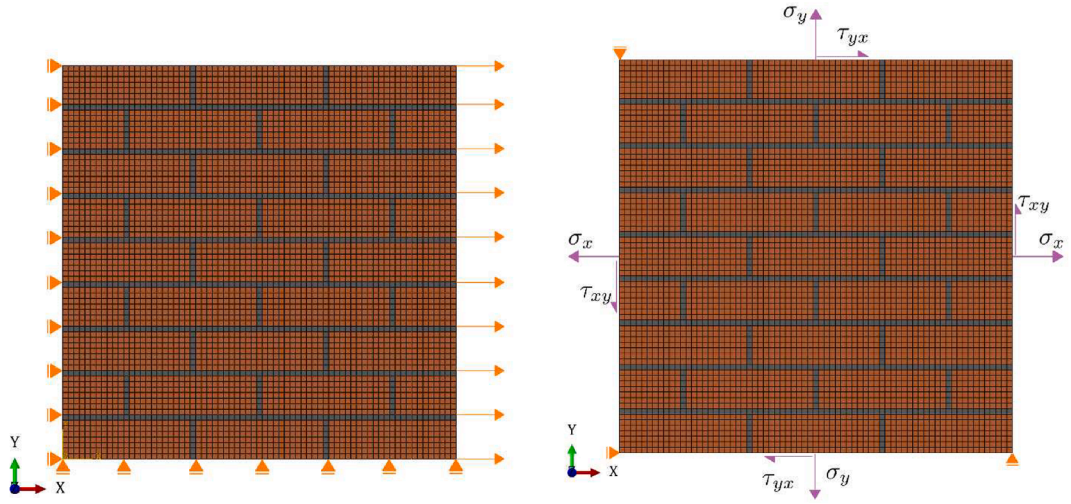

Fig. 8. FEM discretization of the panel and the boundary conditions: (a) uniaxial tension; (b) inclined specimens (tractions applied uniformly along the boundaries).

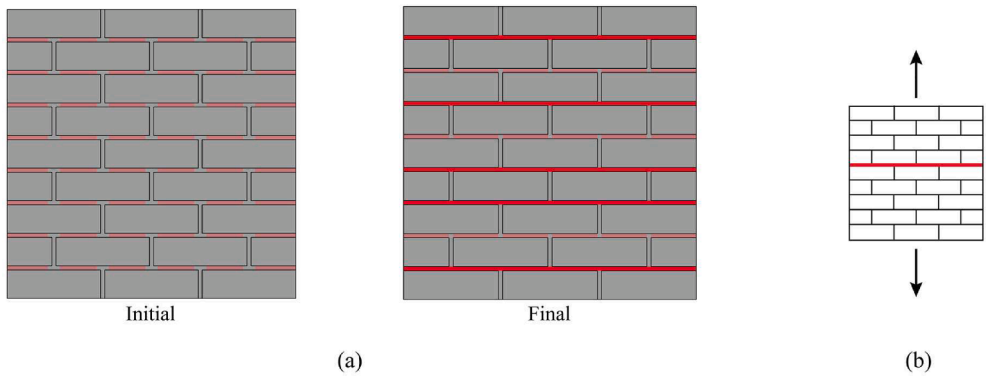

Fig. 9. (a) Evolution of crack pattern and the resulting failure mechanism (bright red colour) for uniaxial tension perpendicular to bed joints ($\theta = 90°$); (b) schematic crack pattern from Page (1983). (For interpretation of the references to colour in this figure legend, the reader is referred to the web version of this article.)

3.3.1. Uniaxial tension tests

The dominant fracture mode in uniaxial tension involves cracking along the brick–mortar interfaces. Depending on the direction of loading with respect to the orientation of bed joints, the tensile fracture in one family of joints may be followed by shear fracture in the perpendicular set of joints. Fig. 9 shows the evolution of damage in case of tension normal to the bedding planes, which are the weakest link within the domain. In this case, the only mode of fracture is a progressive damage along the bed joints, which triggers the failure at the macroscale. The strength of the panel is virtually the same as the tensile strength of the brick–mortar bond. This is shown in Fig. 10 that provides the average macroscopic stress–strain characteristics for the range of values recorded in the experiment, i.e. 0.1–0.3 MPa.

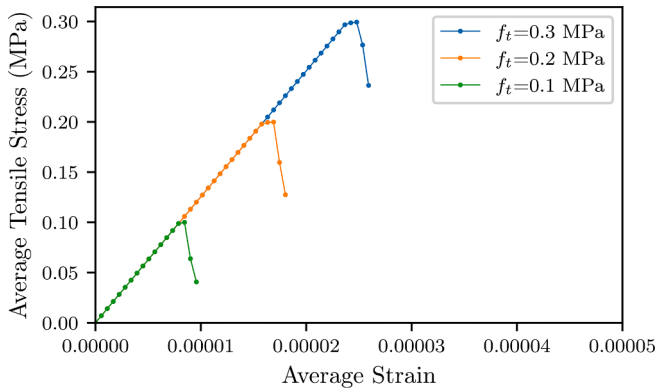

Fig. 10. Average stress–strain characteristics for different tensile strength of brick–mortar bond.

When the direction of uniaxial tension is parallel to the bedding planes, the tensile fractures start developing within the head joints. For the current set of material parameters, the fracture pattern also involves development of shear fractures in the adjacent bed joints. The combined mechanism of sliding along the bed joints and separation along the head joints causes the global failure at the macroscale. Fig. 11 depicts the evolution of the fracture pattern during the deformation process, while Fig. 12 shows the average stress–strain characteristics. It is evident that, in this case, the ultimate load is quite sensitive to the value of the tensile fracture energy G_f. At the same time, the parameter α which governs the degradation of cohesion, viz. Eq. (11), has no influence on the predicted ultimate stress and affects only the stiffness in the post-peak range.

It should be mentioned that for all load-controlled simulations, the bearing capacity was assessed by monitoring a stability factor (SF) defined as the ratio of the second rate of internal work normalized with respect to that corresponding to the elastic solution (Pietruszczak & Oulapour, 1999). In general, the stability factor remains within the range $1 \geq \text{SF} \geq 0$, and $\text{SF} = 0$ implies the singularity in the global stiffness operator, i.e. the loss of stability. Fig. 13 depicts the evolution of SF for the present case, i.e. uniaxial tension parallel to bed joints. The results presented here correspond to $G_f = 1N/m, \alpha = 6000m^{-1}$ (cf. Fig. 12) and include the average stress–strain characteristics up to the ultimate load obtained for both load-controlled (LC) and displacement-controlled (DC) analyses.

In the case of uniaxial tension at 45°, the onset of fracture occurs in bed joints. Again, as the load increases further the cracks along the head joints develop leading eventually to a zig-zag pattern at the macroscale. This is depicted in Fig. 14, which show a progressive evolution of the

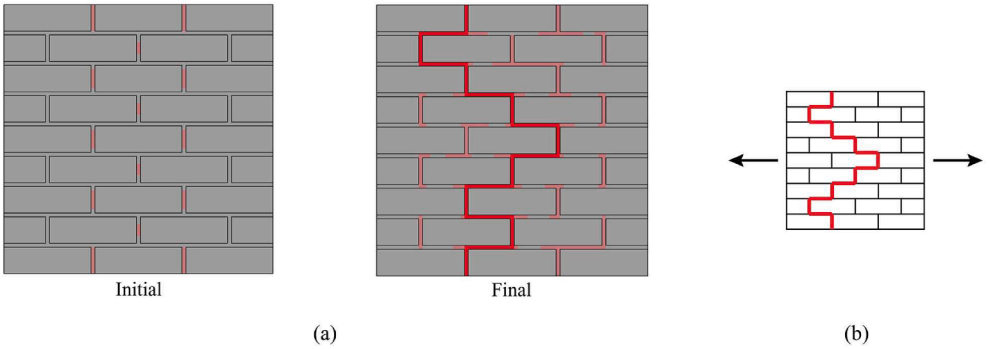

Fig. 11. (a) Evolution of crack pattern and the resulting failure mechanism (bright red colour) for uniaxial tension along the bed joints ($\theta = 0°$); (b) schematic crack pattern from Page (1983). (For interpretation of the references to colour in this figure legend, the reader is referred to the web version of this article.)

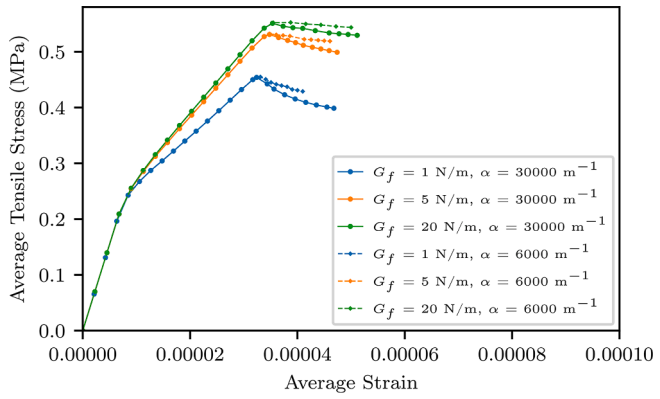

Fig. 12. Average stress–strain characteristics for different values of the tensile fracture energy release G_f and the degradation parameter.α

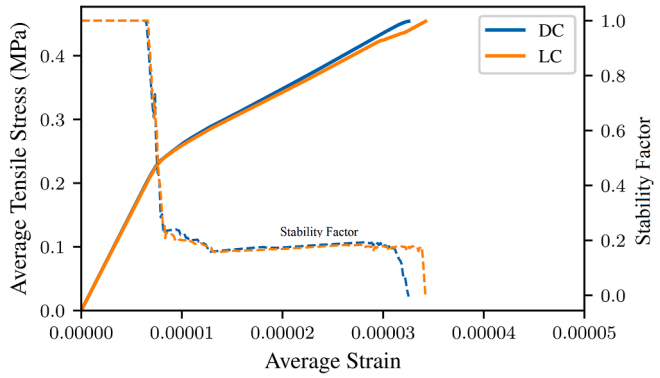

Fig. 13. Evolution of the stability factor (SF) in the panel subjected to uniaxial tension parallel to bed joints.

failure mechanism. The corresponding stress vs. average strain characteristics are presented in Fig. 15. Note that in this case, a load-controlled scheme has been implemented, as described earlier. The ultimate load is significantly affected by the tensile strength of brick–mortar bond, which is evidenced through a parametric study reported in this figure.

3.3.2. *Uniaxial compression tests*

The primary mode of fracture initiation and propagation in this loading scenario is the tensile splitting of the masonry panel, which occurs not only along the brick–mortar interfaces but also, in some cases, within the brick units. When the direction of loading is parallel to bed joints, the joint interfaces undergo a tensile fracture, forming a set of fracture planes that run through the entire panel. For the compression perpendicular to bed joints, however, the tensile fractures develop in head joints, followed by cracking of the adjacent brick units. This results

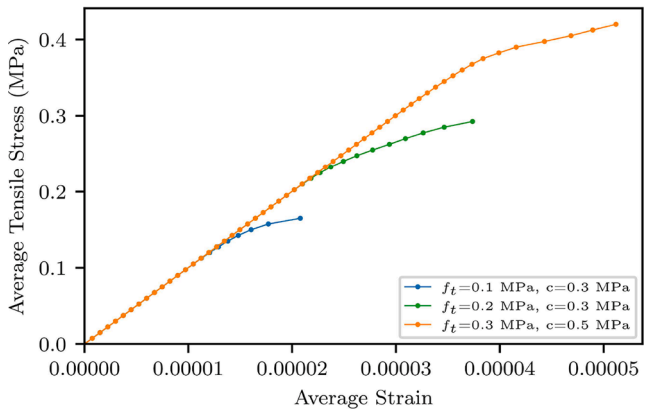

Fig. 15. Average stress–strain characteristics for different values of tensile strength at the brick–mortar interface.

in a higher compressive strength of the panel as compared to other loading directions, as in this case the tensile strength of bricks needs to be attained to trigger a loss of stability.

An important issue to consider in these fracture scenarios is that the failure mechanism does not involve a complete disintegration of the panel at the macroscale. In fact, after formation of tensile splitting planes, the separated parts of the panel act like independent load bearing columns, allowing the panel to sustain significantly higher compressive loads. This part of the mechanical response is not considered in assessing the ultimate bearing capacity in compression, and the formation of a continuous fracture that runs through the panel is perceived as failure. The latter effect is also described in Page (1983) and was used there as the definition of failure at the macroscale. It is noted that this scenario is unlikely to happen in large scale masonry structures, but it is useful for gaining insight into evaluation of the impact of tensile strength of bricks on the ultimate load bearing capacity of masonry panel.

The evolution of fracture mode in uniaxial compression parallel and perpendicular to bed joints is shown in Figs. 16-17. As mentioned earlier, for compression parallel to bed joints, tensile cracks develop in bed joints without triggering the fracture in the bricks. On the other hand, compressive load perpendicular to bed joints causes tensile cracking in head joints followed by initiation of cracks in bricks at the vicinity of the head joints.

3.3.3. *Biaxial tension- compression tests*

The biaxial tension–compression in two perpendicular directions results in a failure mode that is a combination of those discussed previously. The specific mechanism depends on the actual stress ratio. The testing program reported in Dhanasekar et al. (1985) involved the ratios of

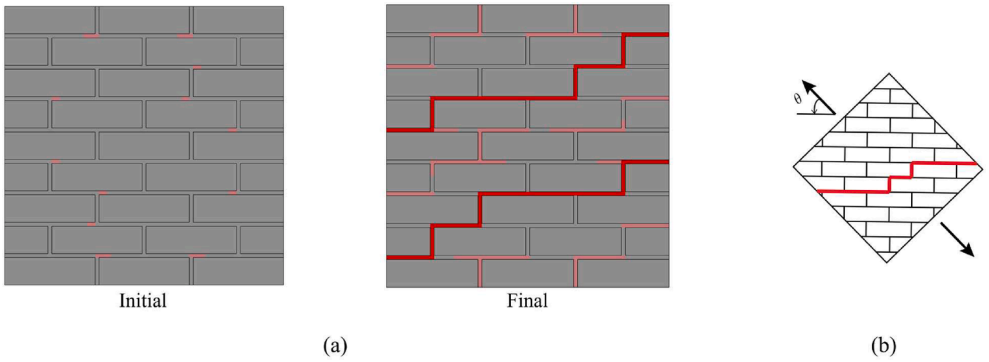

Fig. 14. (a) Evolution of crack pattern and the resulting failure mechanism (bright red colour) for uniaxial tension on inclined panel ($\theta = 45°$); (b) schematic crack pattern from Page (1983). (For interpretation of the references to colour in this figure legend, the reader is referred to the web version of this article.)

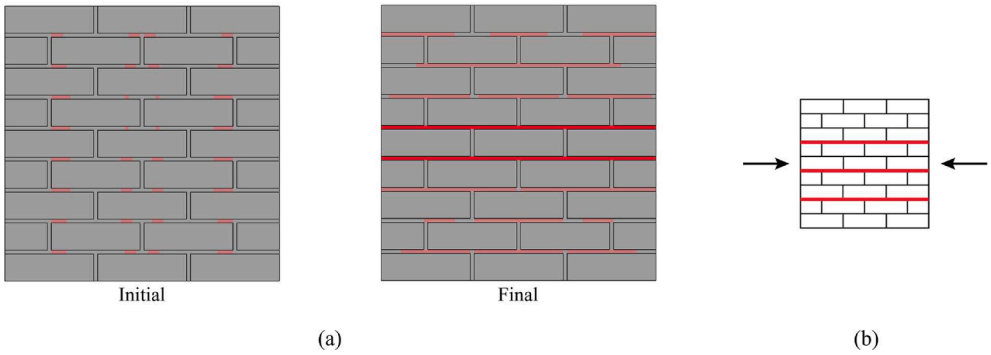

Fig. 16. (a) Evolution of crack pattern and the resulting failure mechanism (bright red colour) (a) for uniaxial compression along the bed joints; (b) schematic crack pattern from Page (1983). (For interpretation of the references to colour in this figure legend, the reader is referred to the web version of this article.)

compressive to tensile load of 2, 5, 10 and 30, and similar values (i.e. 2, 10 and 30) were employed in the current numerical study. The main results of the numerical analysis are provided in Fig. 18, which shows the failure envelopes in the affined space of the major and minor principal stresses. The simulations presented here were carried out for two different values of tensile strength of brick (F_t), i.e. $F_t = 1.0$ and 1.5 MPa, while preserving a constant ratio of 7.5 and 5 between F_t and the tensile and shear strength of brick–mortar bond (f_t), respectively. Thus, for $F_t = 1.0$ MPa for example, there is $f_t = 0.13$ MPa and $c = 0.2$ MPa.

The first plot in Fig. 18 shows the case of compression perpendicular to bed joints and tension parallel to them (i.e., $\theta = 0°$). In this case, the presence of compressive traction increases the shear resistance in bed joints. As a result, after the onset of cracking along the head joints, the tensile cracks in bricks develop, leading to a higher tensile strength

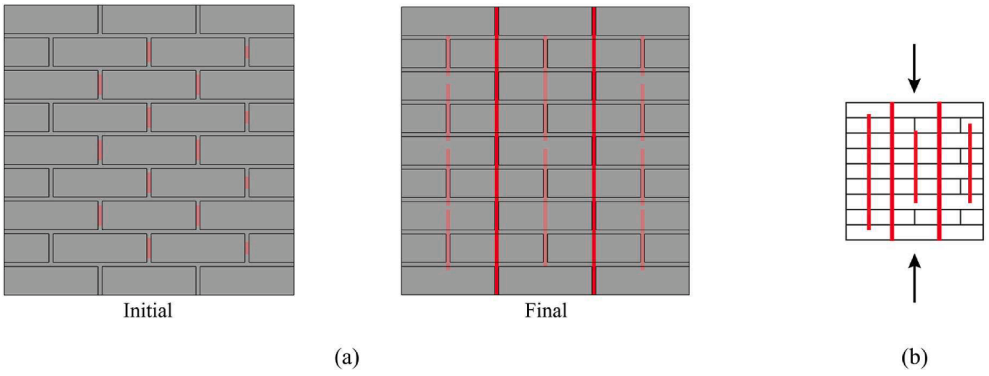

Fig. 17. (a) Evolution of crack pattern and the resulting failure mechanism (bright red colour) (a) for uniaxial compression perpendicular to the bed joints; (b) schematic crack pattern from Page (1983). (For interpretation of the references to colour in this figure legend, the reader is referred to the web version of this article.)

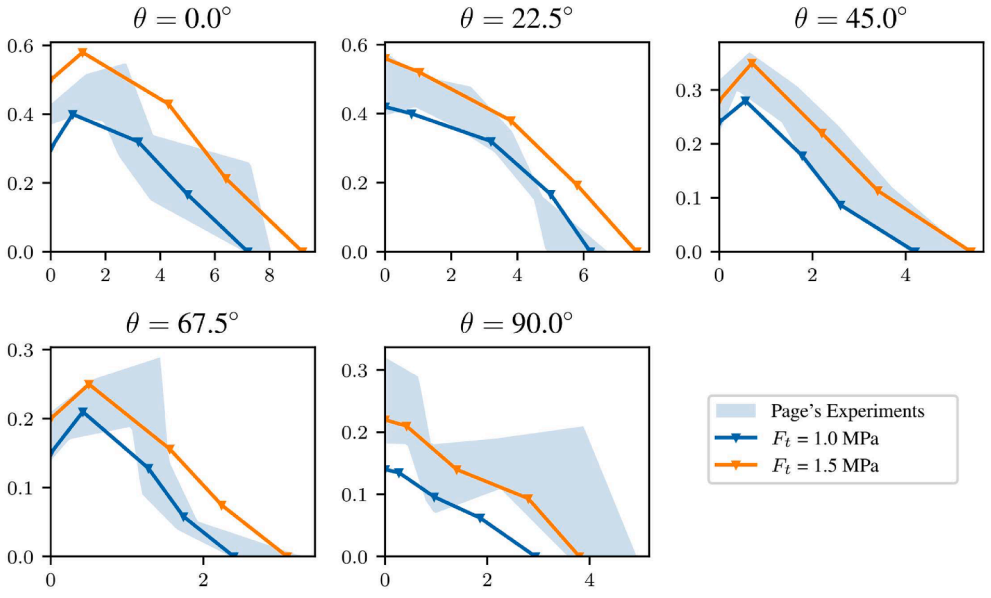

Fig. 18. Failure envelopes for different orientations of the panel (θ) and different tensile strength of masonry units (F_t).

as compared to uniaxial case. As an example, at the stress ratio of 2 and $F_t = 1.5$ MPa, the ultimate tensile and compressive stress values of 0.6 MPa and 1.6 MPa are attained, while the ultimate uniaxial tensile strength is approximately 0.5 MPa.

In the case of compression parallel to bed joints and tension perpendicular to them (i.e., $\theta = 90°$), the response is influenced solely by the bed joints which form a set of continuous weakness planes within the panel. In this situation, an approximately linear transition from ultimate uniaxial compressive strength to ultimate uniaxial tensile strength occurs as the load ratio decreases. The response for other panel orientations, i.e. $\theta = 22.5°$, $45°$, and $67.5°$, has also been simulated and a complete set of results is presented in Fig. 18.

4. Macroscale formulation

The mesoscale approach, as described in Sections 2 and 3, has two primary range of applications; it can be employed for analysis of small-scale masonry structures (e.g. brick walls/arches) and, what is of primary interest here, it can provide a set of 'virtual data' that is required to develop and verify a macroscale approach.

In a macroscale framework, the masonry can be treated as a continuum with a microstructure. In this case, the anisotropic strength/deformation characteristics may be described by adopting a general framework of microstructure tensor approach as outlined in Pietruszczak & Mroz (2001). The approach employs the notion of a scalar anisotropy parameter whose value is a function of relative orientation of the principal stress triad with respect to the preferred directions of microstructure. The macroscopic failure criterion is formulated here by preserving the functional form consistent with mesoscale representation and postulating that the respective strength parameters depend on the orientation of the sample relative to the loading direction. Thus, the mathematical representation incorporates Mohr-Coulomb criterion with Rankine's cut-off in tensile regime, both expressed in terms of stress invariants and enhanced by the notion of directional dependence of strength. The identification of such framework requires the specification of two material functions that describe the variation of friction coefficient and tensile strength with the orientation of the sample relative to the loading direction. Here, an explicit procedure is employed for determination of coefficients of approximation of these functions based on the results of standard axial tension and axial compression tests performed at different orientations of bed joints. For a specific type of masonry, the 'virtual' results of such tests can be generated from the mesoscale simulations, as discussed in Section 3.

Assume that the conditions at failure at the macroscale are governed by the strength criterion expressed in a general form as

$$F = F(I_1, J_2, J_3, \vartheta) = 0 \tag{13}$$

Here, I_1, J_2, J_3, are the basic invariants of stress tensor/deviator, while ϑ is a scalar anisotropy parameter. The latter describes the effect of orientation of principal stress axes in relation to preferred material directions and is defined (after Pietruszczak & Mroz, 2001) as

$$\vartheta = \vartheta_0\left(1 + \xi + b_1\xi^2 + b_2\xi^3 + b_3\xi^4 + \cdots\right); \qquad \xi = \boldsymbol{\ell}\cdot\mathbf{A}\cdot\boldsymbol{\ell} \tag{14}$$

In the above expression, $\boldsymbol{\ell}$ is a unit vector, referred to as a 'loading direction', whose components are the normalized magnitudes of stress vectors acting on planes normal to the material axes. For the structural masonry, the orientation of preferred material axes is defined *a priori* and is identified here with the eigenvectors of the operator $\mathbf{A}$, which is a traceless second-order tensor. Furthermore, the approximation coefficients $\vartheta_0, b_1, b_2, b_3, \cdots$ are constants.

As mentioned earlier, the form of F which is employed in this work, is the Mohr-Coulomb representation with Rankine's cut-off in tensile regime, both incorporating the orientation-dependency of the strength parameters. Thus

$$F = max(F_1, F_2) = 0;$$

$$F_1 = \sqrt{3}\overline{\sigma} - \eta_f g_1(\Theta)(\sigma_m + C) = 0; \tag{15a}$$

$$F_2 = g_2(\Theta)\overline{\sigma} - (\sigma_m + \sigma_t) = 0$$

$$\text{where } \overline{\sigma} = (J_2)^{1/2}, \quad \sigma_m = I_1/3, \quad \Theta = \frac{1}{3}\sin^{-1}\left(\frac{-3\sqrt{3}}{2}\frac{J_3}{\overline{\sigma}^3}\right) \text{ and}$$

$$g_1(\Theta) = \frac{3 - \sin\phi}{2\sqrt{3}\cos\Theta - 2\sin\Theta\,\sin\phi}; \quad \eta_f = \frac{6\sin\phi}{3 - \sin\phi}; \tag{15b}$$

$$g_2(\Theta) = \frac{2}{\sqrt{3}}\sin\left(\Theta + \frac{2\pi}{3}\right); \quad C = c\cot\phi.$$

Here, Θ is the Lode's angle, while ϕ and c represent the angle of friction and cohesion, respectively. For an isotropic medium η_f and σ_t are material constants, while in case of anisotropy both are variables and are defined in the polynomial form (14), i.e.

$$\eta_f = \widehat{\eta}_f\left(1 + \xi + b_1\xi^2 + b_2\xi^3 + b_3\xi^4 + \cdots\right);$$
$$\sigma_t = \widehat{\sigma}_t\left(1 + \xi + c_1\xi^2 + c_2\xi^3 + c_3\xi^4 + \cdots\right) \tag{16}$$

where b's and c's are the approximation coefficients.

For the purpose of identification of material functions (16), it is convenient to express the representation (15) in terms of principal stress values. Thus

$$F_1 = \frac{1}{2}(\sigma_1 - \sigma_2) + \frac{1}{2}(\sigma_1 + \sigma_2)\sin\phi(\xi) - C\sin\phi(\xi) = 0;$$
$$F_2 = \sigma_1 - \sigma_t(\xi) = 0; \ \sigma_1 > \sigma_3 > \sigma_2 \tag{17}$$

where the tensile stresses are considered as positive.

The preliminary step in the identification procedure is the assessment of the value of parameter C appearing in the Mohr-Coulomb failure condition (15). Note that this parameter is associated with *hydrostatic* tension, and as such it is orientation independent. Furthermore, C has no direct physical significance as the strength in tension regime is governed by the cut-off criterion $F_2 = 0$ in which $max\{\sigma_t\} < C$. Thus, an assessment of C is required only to enable the specification of the material function $\eta_f(\xi)$. Fig. 19 shows the linear best-fit approximations to the numerical data plotted in the affined space $\frac{1}{2}(\sigma_1 - \sigma_2)$ *vs.* $\frac{1}{2}(\sigma_1 + \sigma_2)$. An estimate of C was obtained by taking the maximum value over the set of configurations considered, which resulted in $C = 0.95$ MPa.

Given the value of C, the next step is to identify the distribution of strength parameter $\eta_f(\xi)$. Referring the problem to the coordinate system in Fig. 7b, with x-axis along the horizontal, the components of loading vector $\boldsymbol{l}$ and unit loading vector $\boldsymbol{\ell}$, for a plane stress configuration, become

$$l_1^2 = \cos^2\theta\sigma_x^2 + \sin^2\theta\sigma_y^2;$$

$$l_2^2 = \cos^2\theta\sigma_y^2 + \sin^2\theta\sigma_x^2; \ l_3^2 = 0;$$

$$\ell_1^2 = \frac{l_1^2}{l_1^2 + l_2^2} = \frac{\cos^2\theta\sigma_x^2 + \sin^2\theta\sigma_y^2}{\sigma_x^2 + \sigma_y^2}; \tag{18}$$

$$\ell_2^2 = \frac{l_2^2}{l_1^2 + l_2^2} = \frac{\cos^2\theta\sigma_y^2 + \sin^2\theta\sigma_x^2}{\sigma_x^2 + \sigma_y^2}.$$

Assume, as a first approximation, that the material may be perceived as transversely isotropic. In this case, $A_1 = A_3$, which in view of the fact that $\mathbf{A}$ is a traceless operator, implies $A_2 = -2A_1$. Thus, the dyadic product $\xi = \boldsymbol{\ell}\cdot\mathbf{A}\cdot\boldsymbol{\ell}$ may be defined in an explicit form

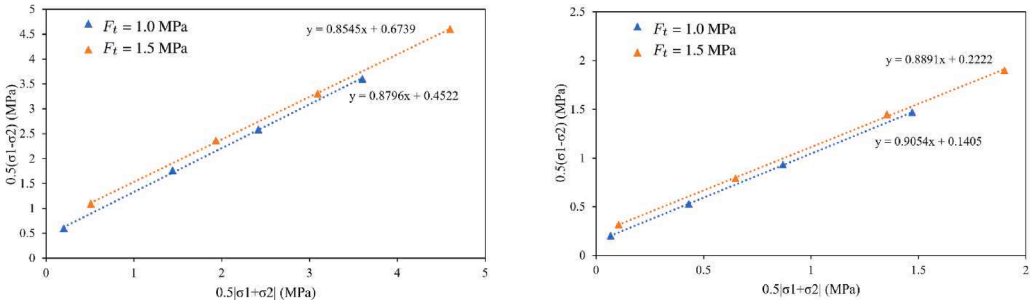

Fig.19. Failure envelopes in compression regime for $\theta = 90^{\circ}$ and $\theta = 0^{\circ}$, respectively.

$$\begin{aligned}\xi &= \boldsymbol{\ell}\cdot\mathbf{A}\cdot\boldsymbol{\ell} = \mathrm{A}_1\left(\mathrm{l}_1^2 - 2\mathrm{l}_2^2\right)\\ &= \mathrm{A}_1\left[\frac{\sigma_x^2\left(1-3\sin^2\theta\right)+\sigma_y^2\left(1-3\cos^2\theta\right)}{\sigma_x^2+\sigma_y^2}\right]\end{aligned} \tag{19}$$

in which A_1 is the only independent eigenvalue of $\mathbf{A}$. It is evident that for the uniaxial load, the above expression simplifies to $\xi = \mathrm{A}_1\left(1-3\sin^2\theta\right)$.

Fig. 20a shows the best-fit approximation for the function $\eta_f(\xi)$. The results are based on the numerical data for uniaxial compression at different orientations of bed joints. Note that in this case

$$\left.\begin{aligned}\sigma_1 &= f_c\\ \sigma_2 &= 0\end{aligned}\right\}\rightarrow \sin\phi = \frac{f_c}{f_c+2C};\qquad \eta_f = \frac{6\sin\phi}{3-\sin\phi} = \frac{3f_c}{f_c+3C} \tag{20}$$

where $f_c = f_c(\xi)$ is the uniaxial compressive strength. The approximations are provided again for two different values of the tensile strength of brick units, viz. $F_t = 1.0$ and 1.5 MPa, which is similar to the parametric study in Section 3.1.3. The mathematical representation incorporates the terms up to the order of three in Eq. (16) and the respective values of coefficients of approximation are given in Table 3.

Fig. 20b shows the best-fit approximation for the function $\sigma_t(\xi)$, which describes the spatial variation of uniaxial tensile strength of the brickwork. Here, the approximations employ again the third-order terms in the dyadic product $\boldsymbol{\ell}\cdot\mathbf{A}\cdot\boldsymbol{\ell}$. The resulting approximation coefficients, for both sets of parameters associated with $F_t = 1.0$ and 1.5 MPa, are given in Table 4.

Finally, Fig. 21 shows the numerical predictions of strength in biaxial tension–compression based on the failure criterion (15). Here, the values of best-fit approximation coefficients provided in Table 4 were employed and the results correspond to $\theta = 0^{\circ}$, 22.5°, and 90°.

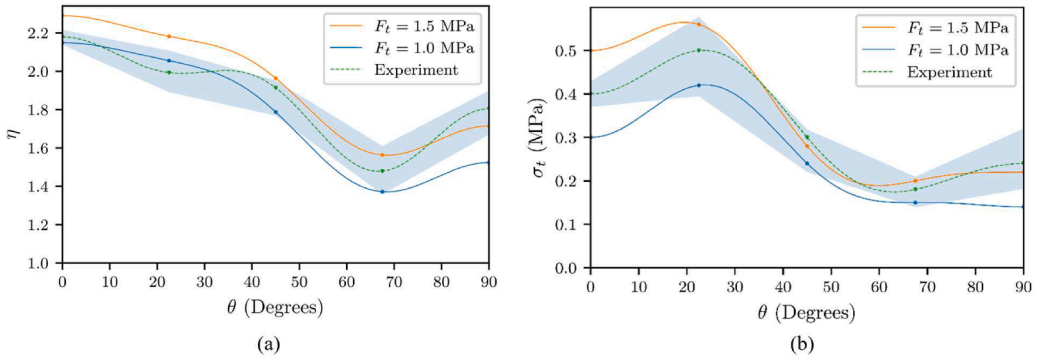

Fig. 20. Best-fit approximations to spatial distribution of strength parameters η_f and σ_t.

Table 4
The coefficients of best-fit approximation for material functions $\eta_f(\xi)$ and $\sigma_t(\xi)$.

	$\widehat{\eta}_f$	A_1	b_1	b_2	b_3	$\widehat{\sigma}_t$	A_1	c_1	c_2	c_3
$F_t =$ 1.5*MPa*	2.11	0.089	−10.67	56.56	639.10	0.20	−0.387	5.83	2.34	−10.67
$F_t =$ 1.0*MPa*	1.96	0.125	−6.09	14.04	159.76	0.17	−0.507	2.84	0.97	−3.93

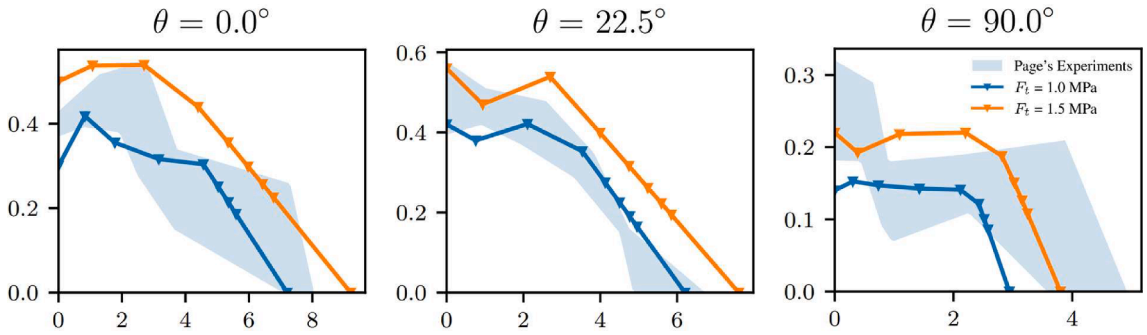

Fig. 21. Estimated macroscale ultimate strength envelopes for different orientations of the panel (θ) and different tensile strength of masonry units (F_t).

5. Final remarks

The main focus in this work was the development of a computational framework for meso and macroscale analysis of structural masonry. The *mesoscale* approach incorporated a constitutive law with embedded discontinuity to deal with the localized deformation in bed/head joints as well as with the onset and propagation of damage in brick units. In this case, a simple structured FEM has been used in which the brick–mortar interface, which represents the weakest link in the masonry panel, is perceived as being embedded in the adjacent intact medium. For bricks, the level-set method has been employed for tracing the location and propagation of cracks. The proposed methodology yields the results that are not affected by the finite element discretization, which is due to the presence of a length-scale parameter. In addition, the treatment of head/bed joints, as being embedded within a structured mesh, significantly improves the computational efficiency as compared to standard approach that explicitly incorporates all constituents and their interfaces.

The objectives of developing the mesoscale approach are two-fold. On one hand, the framework is suitable for the analysis of small-scale masonry structures. At the same time, it provides a bridging between the two scales, i.e. it serves the purpose of generating 'virtual data' that can be employed for identification of material functions appearing in the macroscale approach. Both these aspects have been illustrated by a number of numerical examples that included the simulations of the tensile and shear tests on brick–mortar bond as reported in Van der Pluijm (1997, 2000) as well as a comprehensive analysis of a set of experimental tests conducted by Dhanasekar et al. (1985) and Page (1983). The latter involved masonry panels subjected to biaxial loading at different orientations of bed joints. For all cases considered, the results have been compared with experimental data, thereby providing a proof-of-concept.

For the *macroscale* approach, only some preliminary work has been reported here. In particular, a procedure for identification of material functions embedded in this framework has been outlined. The latter employed the results of axial compression and tension generated through the mesoscale analysis of panels at different orientation of bed joints. Obviously, a more accurate approximation of these functions may be obtained by also considering the biaxial tension–compression loading.

For the macroscale simulations, an important issue is the specification of the conditions for the onset of localization. In this case, the representation (15) may be phrased in the context of elastoplasticity, so that the localization is perceived as a bifurcation problem. Alternatively, if the conditions at failure are defined through Coulomb and/or Rankine type of criterion, the critical plane approach (Pietruszczak and Mroz, 2001) may be employed whereby the orientation of the localization plane is defined as a constrained optimization problem. Finally, one can also use the 'virtual' data generated from the mesoscale analyses and construct a data-driven neural network that would predict the orientation of macro-fracture for a given stress state. Such an approach could potentially prove to be efficient in engineering applications and will be explored in the follow up studies.

Declaration of Competing Interest

The authors declare that they have no known competing financial interests or personal relationships that could have appeared to influence the work reported in this paper.

Acknowledgement

The research presented here was supported by the Natural Sciences and Engineering Research Council of Canada through a Collaborative Research and Development Grant (CRD) in partnership with Hydro-Quebec.

References

Adalsteinsson, D., Sethian, J.A., 1999. The fast construction of extension velocities in Level Set Methods. J. Comput. Phys. 148 (1), 2–22. https://doi.org/10.1006/jcph.1998.6090.
Alfaiate, J., Simone, A., Sluys, L.J., 2003. Non-homogeneous displacement jumps in strong embedded discontinuities. Int. J. Solids Struct. 40 (21), 5799–5817.
Anthoine, Armelle, 1997. Homogenization of periodic masonry: plane stress, generalized plane strain or 3D modelling? Commun. Numer. Methods Eng. 13 (5), 319–326.
Backes, H.P., 1985. Tensile strength of masonry. In: Proceedings of the 7th International Brick Masonry Conference (Melbourne, Australia). Brick Development Research Institute, pp. 779–790.
Bažant, Z.P., Jirásek, M., 2002. Nonlocal integral formulations of plasticity and damage: survey of progress. J. Eng. Mech. 128 (11), 1119–1149. https://doi.org/10.1061/(ASCE)0733-9399(2002)128:11(1119).
Benkemoun, N., Hautefeuille, M., Colliat, J.-B., Ibrahimbegovic, A., 2010. Failure of heterogeneous materials: 3D meso-scale FE models with embedded discontinuities. Int. J. Numer. Meth. Eng. 82 (13), 1671–1688.
Belytschko, T., Black, T., 1999. Elastic crack growth in finite elements with minimal remeshing. Int. J. Numer. Meth. Eng. 45 (5), 601–620. https://doi.org/10.1002/(ISSN)1097-020710.1002/(SICI)1097-0207(19990620)45:5<>1.0.CO;2-V10.1002/(SICI)1097-0207(19990620)45:5<601::AID-NME598>3.0.CO;2-S.
Belytschko, T., Moës, N., Usui, S., Parimi, C., 2001. Arbitrary discontinuities in finite elements. Int. J. Numer. Meth. Eng. 50 (4), 993–1013. https://doi.org/10.1002/1097-0207(20010210)50:4<993::AID-NME164>3.0.CO;2-M.
Berto, L., Saetta, A., Scotta, R., Vitaliani, R., 2002. An orthotropic damage model for masonry structures. Int. J. Numer. Meth. Eng. 55 (2), 127–157.
Boehler, J.P., Sawczuk, A., 1977. On yielding of oriented solids. Acta Mech. 27 (1), 185–204. https://doi.org/10.1007/BF01180085.
Cluni, F., Gusella, V., 2004. Homogenization of non-periodic masonry structures. Int. J. Solids Struct. 41 (7), 1911–1923. https://doi.org/10.1016/j.ijsolstr.2003.11.011.
Cowin, S.C., 1986. Fabric dependence of an anisotropic strength criterion. Mech. Mater. 5 (3), 251–260. https://doi.org/10.1016/0167-6636(86)90022-0.
De Buhan, P., De Felice, G., 1997. A homogenization approach to the ultimate strength of brick masonry. J. Mech. Phys. Solids 45 (7), 1085–1104. https://doi.org/10.1016/S0022-5096(97)00002-1.
Dhanasekar, M., Kleeman, P.W., Page, A.W., 1985. Biaxial stress-strain relations for brick masonry. J. Struct. Eng. (United States) 111 (5), 1085–1100. https://doi.org/10.1061/(ASCE)0733-9445(1985)111:5(1085).
Drysdale, R.G., Khattab, M.M., 1995. In-plane behavior of grouted concrete masonry under biaxial tension-compression. Structural Journal 92 (6), 653–664.
Feyel, F., 2003. A multilevel finite element method (FE2) to describe the response of highly non-linear structures using generalized continua. Comput. Methods Appl. Mech. Eng. 192 (28-30), 3233–3244.

Geers, M.G.D., Kouznetsova, V.G., Brekelmans, W.A.M., 2010. Multi-scale computational homogenization: Trends and challenges. J. Comput. Appl. Math. 234 (7), 2175–2182. https://doi.org/10.1016/j.cam.2009.08.077.

Haghighat, E., Pietruszczak, S., 2015. On modeling of discrete propagation of localized damage in cohesive-frictional materials. Int. J. Numer. Anal. Meth. Geomech. 39 (16), 1774–1790. https://doi.org/10.1002/nag.v39.1610.1002/nag.2368.

Haghighat, E., Pietruszczak, S., 2016. On modeling of fractured media using an enhanced embedded discontinuity approach. Extreme Mech. Lett. 6, 10–22.

Jirásek, M., 2000. Comparative study on finite elements with embedded discontinuities. Comput. Methods Appl. Mech. Eng. 188 (1-3), 307–330.

Jirásek, M., Zimmermann, T., 2001. Embedded crack model: I. Basic formulation. Int. J. Numer. Meth. Eng. 50 (6), 1269–1290.

Jirásek, M., 2004. Non-local damage mechanics with application to concrete. Revue Française de Génie Civil 8 (5–6), 683–707. https://doi.org/10.1080/12795119.2004.9692625.

Lourénço, P.B., De Borst, R., Rots, J.G., 1997. A plane stress softening plasticity model for orthotropic materials. Int. J. Numer. Meth. Eng. 40 (21), 4033–4057.

Lourénço, P.B., Milani, G., Tralli, A., Zucchini, A., 2007. Analysis of masonry structures: review of and recent trends in homogenization techniques. Can. J. Civ. Eng. 34 (11), 1443–1457. https://doi.org/10.1139/L07-097.

Massart, T.J., Peerlings, R.H.J., Geers, M.G.D., 2007. An enhanced multi-scale approach for masonry wall computations with localization of damage. Int. J. Numer. Meth. Eng. 69 (5), 1022–1059.

Minga, E., Macorini, L., Izzuddin, B.A., 2018. A 3D mesoscale damage-plasticity approach for masonry structures under cyclic loading. Meccanica 53 (7), 1591–1611. https://doi.org/10.1007/s11012-017-0793-z.

Moës, N., Belytschko, T., 2002. Extended finite element method for cohesive crack growth. Eng. Fract. Mech. 69 (7), 813–833. https://doi.org/10.1016/S0013-7944(01)00128-X.

Needleman, A., 1988. Material rate dependence and mesh sensitivity in localization problems. Comput. Methods Appl. Mech. Eng. 67 (1), 69–85. https://doi.org/10.1016/0045-7825(88)90069-2.

Nguyen, V.P., Lloberas-Valls, O., Stroeven, M., Sluys, L.J., 2011. Homogenization-based multiscale crack modelling: From micro-diffusive damage to macro-cracks. Comput. Methods Appl. Mech. Eng. 200 (9-12), 1220–1236.

Niazi, M.S., Wisselink, H.H., Meinders, T., 2012. Viscoplastic regularization of local damage models: A latent solution. Key Eng. Mater. 504–506, 845–850. https://doi.org/10.4028/www.scientific.net/KEM.504-506.845.

Oliver, J., Huespe, A.E., Sánchez, P.J., 2006. A comparative study on finite elements for capturing strong discontinuities: E-FEM vs X-FEM. Comput. Methods Appl. Mech. Eng. 195 (37-40), 4732–4752.

Page, A.W., 1981. The biaxial compressive strength of brick masonry. Proceedings of the Institution of Civil Engineers, ICE Publishing 71 (3), 893–906. https://doi.org/10.1680/iicep.1981.1825.

Page, A.W., 1983. The strength of brick masonry under biaxial tension-compression. Int. J. Masonry Construction 3 (1), 26–31.

Pande, G.N., Liang, J.X., Middleton, J., 1989. Equivalent elastic moduli for brick masonry. Comput. Geotech. 8 (3), 243–265. https://doi.org/10.1016/0266-352X(89)90045-1.

Pietruszczak, S., 1999. On homogeneous and localized deformation in water-infiltrated soils. Int. J. Damage Mech. 8 (3), 233–253.

Pietruszczak, S., Mohammadi, M., 2020. A continuum-based strength criterion for masonry : identification of parameters and validation. Int. J. Masonry Res. Innovation 5 (3), 423–440. https://doi.org/10.1504/IJMRI.2020.108004.

Pietruszczak, S.t., Mróz, Z., 1981. Finite element analysis of deformation of strain-softening materials. Int. J. Numer. Meth. Eng. 17 (3), 327–334.

Pietruszczak, S., Mroz, Z., 2001. On failure criteria for anisotropic cohesive-frictional materials. Int. J. Numer. Anal. Meth. Geomech. 25 (5), 509–524. https://doi.org/10.1002/(ISSN)1096-985310.1002/nag.v25:510.1002/nag.141.

Pietruszczak, S., Oulapour, M., 1999. Assessment of dynamic stability of foundations on saturated sandy soils. J. Geotech. Geoenviron. Eng. 125 (7), 576–582. https://doi.org/10.1061/(asce)1090-0241(1999)125:7(576).

Van der Pluijm, R., 1993. Shear behaviour of bed joints. Proceedings of 6th North American Masonry Conference, Philadelphia, Pennsylvania, USA 125–136.

Van der Pluijm, R., 1997. Non-linear behaviour of masonry under tension. Heron Journal-English Edition 42 (1), 25–54. ISSN 0046-7316.

Van der Pluijm, R., Rutten, H., & Ceelen, M. (2000). Shear behaviour of bed joints. *12th International Brick/Block Masonry Conference (Madrid, Spain), Historical and Masonry Structures, Minho University Publication.*

Rudnicki, J.W., Rice, J.R., 1975. Conditions for the localization of deformation in pressure-sensitive dilatant materials. J. Mech. Phys. Solids 23 (6), 371–394. https://doi.org/10.1016/0022-5096(75)90001-0.

Sacco, E., 2009. A nonlinear homogenization procedure for periodic masonry. European Journal of Mechanics-A/Solids 28 (2), 209–222.

Simo, J.C., Oliver, J., Armero, F., 1993. An analysis of strong discontinuities induced by strain-softening in rate-independent inelastic solids. Comput. Mech. 12 (5), 277–296. https://doi.org/10.1007/BF00372173.

van der Sluis, O., Schreurs, P.J.G., Brekelmans, W.A.M., Meijer, H.E.H., 2000. Overall behaviour of heterogeneous elastoviscoplastic materials: effect of microstructural modelling. Mech. Mater. 32 (8), 449–462.

Smit, R.J.M., Brekelmans, W.A.M., Meijer, H.E.H., 1998. Prediction of the mechanical behavior of nonlinear heterogeneous systems by multi-level finite element modeling. Comput. Methods Appl. Mech. Eng. 155 (1-2), 181–192.

Stolarska, M., Chopp, D.L., Moës, N., Belytschko, T., 2001. Modelling crack growth by level sets in the extended finite element method. Int. J. Numer. Meth. Eng. 51 (8), 943–960. https://doi.org/10.1002/nme.201.

Tsai, S.W., Wu, E.M., 1971. A general theory of strength for anisotropic materials. J. Compos. Mater. 5 (1), 58–80. https://doi.org/10.1177/002199837100500106.

Villard, P., 1996. Modelling of interface problems by the finite element method with considerable displacements. Comput. Geotech. 19 (1), 23–45.

Wells, G.N., Sluys, L.J., 2000. Application of embedded discontinuities for softening solids. Eng. Fract. Mech. 65 (2-3), 263–281.

Wells, G.N., Sluys, L.J., 2001. Three-dimensional embedded discontinuity model for brittle fracture. Int. J. Solids Struct. 38 (5), 897–913.

Numerical analysis of large masonry structures: bridging meso and macro scales via artificial neural networks

K. Koocheki, S. Pietruszczak*
McMaster University, Hamilton, ON, Canada

Abstract

This paper presents a methodology for analysis of large-scale masonry structures. The approach involves development of a series of artificial neural networks which enable the identification of main variables employed in the macroscopic formulation that incorporates an inelastic constitutive law with embedded discontinuity. The data required for training of neural networks is generated using 'virtual experiments', whereby the 'equivalent' anisotropic response of masonry is investigated through a mesoscale finite element analysis of masonry wallets. The paper outlines the procedure for identification of approximation coefficients describing the orientation-dependency of strength, and other relevant parameters. A numerical example is provided involving analysis of a large masonry wall with multiple openings. The results of macroscale approach are compared with those based on a detailed mesoscale model for the same geometry and boundary conditions.

Keywords: brick masonry; anisotropic failure criterion; artificial neural network; macroscale modelling; homogenization

1. Introduction

For small scale masonry structures (e.g., shear walls, reduced scale models) the numerical analysis is typically conducted at the meso-level, i.e. by examining all constituents (i.e., brick units, mortar joints, and brick-mortar interface) and their interaction. Such an analysis is fairly accurate but cannot be employed in the context of long-span masonry construction. In the latter case, the masonry may be considered as an anisotropic continuum with a microstructure. Such an approach can significantly reduce the computational effort, it requires however a suitable methodology for assessing the averaged/homogenized properties based on properties of constituents and their geometric arrangement.

---

* Corresponding author: pietrusz@mcmaster.ca

Over the last few decades intensive research has been conducted on estimating the anisotropic properties of masonry in the range of both elastic as well as nonlinear inelastic deformation, including the process of onset and propagation of macrocracks. Considering masonry as a periodic medium, Anthoine [1] and Urbanski et al. [2] employed the mathematical theory of homogenization to assess the elastic properties at the macroscale. A nonlinear homogenization procedure for masonry, based on the transformation field analysis, was proposed in [3] and was implemented in finite element simulations at the macroscale. A homogenization approach for predicting the ultimate strength of brick masonry was developed in [4]. In this approach, the masonry units were considered as rigid and were separated by joint interfaces that captured velocity jumps across the brick-mortar bond. In later work, Cluni and Gusella [5] derived the stiffness tensor for non-periodic masonry using the notion of representative elementary volume (REV). A comprehensive review of various homogenization methods has been provided in [6].

In terms of experimental work, most research has been focused on small scale tests on masonry components. There is a lack of extensive experimental campaigns on full-scale prototypes, although some experimental work in this respect has been carried out by several researchers [7–11]. Those tests have been performed on a shaking table and involved an assessment of seismic response of unreinforced masonry buildings. In particular, the effectiveness of various strengthening interventions has been examined. Apparently, there are no experimental investigations on existing long-span masonry construction, which is due to the physical limitations of testing set-ups. This is actually the main challenge in verification of numerical approaches that are employed for analysis of large-scale structures. Therefore, the numerical investigations usually involve a comparison of the results obtained using different methodologies (cf. [12]).

The methodologies themselves vary in terms of both description of deformation response and the assessment of ultimate strength. Over the last few decades several different continuum models have been proposed, such as [13–16] among others. Lourenço and his co-workers [13] developed plasticity models incorporating a modified Hill and Rankin failure criteria in compression and tension along the orthogonal material axes. Gambarotta and Lagomarsino [14] introduced the homogenized version of their microscale damage model by considering brick masonry as an equivalent stratified medium. Both these approaches have been applied in the context of

macroscale analysis. Brasile and co-workers [15,16] proposed a multi-level iterative formulation where mesoscale interactions between masonry constituents are considered at first at the 'local' level, followed by an equivalent continuum 'global' level iteration accounting for the structural arrangement of bricks. In addition, Cosserat structured continuum models, accounting for the mutual blocks rotations, have been proposed and their performance compared with that of Cauchy material (cf. [17]).

In addition to continuum frameworks, various simplified engineering approaches have been employed. For example, Pietruszczak and Niu [18] used the concept of a superimposed medium. In this approach the brick matrix with head joints was considered as an orthotropic elastic–brittle material and its mechanical properties were determined from Eshelby's solution to an ellipsoidal inclusion problem combined with Mori–Tanaka's mean-field theory [19]. The masonry was then regarded as a continuum stratified with a family of bed joints, which formed the weakest link in the microstructure, and the average constitutive relation for the entire composite system was obtained from Hill's averaging rule. Under simplified hypothesis about microstructure geometry and micro–macro quantities relationships, constitutive laws for the homogenized material were also proposed [20].

An alternative to a continuum approach, involves application of Artificial Neural Networks (ANNs). The latter were used, for example, for specification of the conditions at failure in masonry [21,22]. In general, ANNs have mostly been employed for predicting the load-displacement characteristics in selected type of problems, e.g. masonry walls under shear [23,24] or compressive loads [25–27]. The networks were trained using the collected experimental data, which limits their use to boundary conditions consistent with training.

The aim and novelty of the present study lies in combining ANNs and FEM to provide a computationally efficient scheme for analysis of large-scale masonry structures. An overview of the proposed methodology is given in Section 2. Section 3 describes the development of neural networks for predicting orientation-dependent strength of masonry as well as the assessment of elastic properties at the macroscale. Here, the procedure for generation of a database using a mesoscale approach is outlined and the aspects of training of ANNs are addressed. Section 4 reviews the continuum-level formulation for masonry incorporating a microstructure tensor approach [28,29] and its implementation in plasticity framework. Section 5 presents an example

of numerical analysis of a large masonry wall with multiple openings. Here, the results of macroscale approach are compared with those based on a mesoscale model for the same geometry and boundary conditions. The example clearly demonstrates that the continuum-level representation of structural masonry is not only very efficient but also fairly accurate in relation to its mesoscale counterpart. Final discussion and concluding remarks are presented in Section 6.

2. Methodology for numerical analysis of large-scale structures

As stated earlier, the work presented here is focused on development of a framework that enables modeling of mechanical behaviour of large masonry structures, with a horizontal span that might be of the order of hundreds of meters. In this case the masonry needs to be considered as a continuum with inherent anisotropy attributed to its internal structure. The anisotropy in mechanical response relates to deformation properties, in both elastic and inelastic range, the conditions at failure as well as the orientation of macrocracks at the onset of localization. All these depend on the orientation of material axes with respect to the principal stress directions.

In order to provide a pragmatic approach which can be used for practical engineering applications, the framework is constructed in such a way that the key variables defining the anisotropy effects at the macroscale are established directly from the basic properties of constituents, the latter identifiable from simple mechanical tests. For that purpose, a series of artificial neural networks is developed. It is noted that ANNs are typically trained using a broad range of *experimental* data. In case of masonry, this entails a large number of tests on panels subjected to biaxial loading at different orientation of bed joints relative to loading direction (cf. [30–32]). Such an approach is not only expensive and time consuming but practically impossible in case of existing structures. Therefore, in the present study, the required data is generated using 'virtual experiments', whereby the macroscale response of masonry is obtained through finite element analysis of masonry wallets. The simulations are based on a mesoscale approach that employs a numerical scheme outlined in [33] which incorporates a constitutive law with embedded discontinuity (CLED, cf. [34,35]).

Fig. 1 shows a schematic diagram of the proposed numerical scheme. Given the basic mechanical properties of constituents (viz. elastic constants for brick material and mortar, tensile and shear strength of bricks as well as brick-mortar bond) two types of ANNs are employed. The first one

provides the data for assessment of approximation coefficients which appear in the macroscopic failure criterion that incorporates a microstructure tensor approach [29]. At the same time, other trained networks are employed to predict the homogenized elastic properties of masonry and material parameters that appear in the macroscale plasticity formulation. Given this information, the structural analysis is carried out in the range of homogeneous deformation. Once the transition to localized deformation occurs, the average orientation of macrocrack is estimated using another auxiliary ANN trained, once more, through the mesoscale simulations. The subsequent analysis, which involves localized deformation associated with strain-softening, is carried out using the constitutive law with embedded discontinuity, analogous to that employed in mesoscale approach.

Since the AANs are trained for a broad range of input, i.e. properties of constituents, the proposed scheme can be applied to a variety of large-scale masonry structures provided the architectural layout is consistent with that used for the training process.

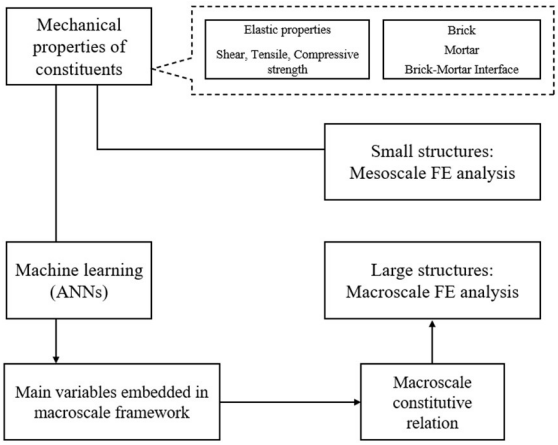

Fig. 1. Summary of the present computational framework for analysis of masonry structures

3. Development of neural networks

Artificial neural networks are one of widely used classes of Machine Learning that were created based on the functioning mechanism of axons in nerve cells. The building-block of ANNs, called the perceptron [36], is in itself a simple one-layer neural network functioning as a linear classifier. Combining the perceptrons, so that the output of one is used as the input of another perceptron, gives multilayer perceptrons [37,38] which are categorized as feed-forward neural networks. The

information originates from the input layer and is transformed through different functions in 'hidden layers' to finally form the output of the network, which is compared to the actual expected values. A single layer in a feed-forward neural network can be described as

$$\mathbf{y}_{(i)} = f_{(i)}\left(\mathbf{W}_{(i)} \cdot \mathbf{y}_{(i-1)} + \mathbf{b}_{(i)}\right), \qquad i = 1, 2, \dots, n_{layers} \tag{1}$$

in which $\mathbf{y}$ is the output vector of the i-th layer, $\mathbf{W}$ and $\mathbf{b}$ are weight and bias vectors, and f is the *activation function*. In this approach which is called 'supervised learning', the error or loss function may be calculated using mean squared error defined as

$$\text{MSE} = \frac{1}{n}\sum_{j=1}^{n}\left(\text{Y}_j - \text{Y}_j^*\right)^2 \tag{2}$$

where n is the number of output nodes, Y is the network output and Y^* is the actual expected value. The loss function is minimized using optimization algorithms.

The ability of ANNs to predict complex nonlinear behaviour, combined with the increasing availability of open-source libraries such as Keras and Tensorflow, makes them an attractive option for computational solid mechanics [39–43]. A comprehensive review of Machine Learning approaches in mechanics of composite materials is presented in [44]. In these approaches, the neural networks were trained using either experimental data or numerical simulations and were used to explicitly predict the underlying constitutive relations. In addition, in several other studies [45–50], the averaged homogenized response of nonlinear elastic materials with complex microstructure was examined based on neural networks coupled with FEM.

In the present study, the primary objective is to develop an ANN that serves as a surrogate model to predict the biaxial strength characteristics of masonry panels for different orientations of bed joints. This information is then employed to estimate the approximation coefficients that define the directional dependency of strength and deformation parameters for the macroscopic elastoplasticity framework, as well as the corresponding orientation of the localization plane. The ANNs were developed using SciANN [51], a Python package for scientific computing with Keras/Tensorflow backend.

3.1. Neural network for predicting orientation-dependent strength of masonry

This neural network has been developed using a broad-spectrum of 'virtual data' generated through mesoscale simulations of running-bond masonry panels. The numerical analysis incorporated a constitutive law with embedded discontinuity (CLED). In this approach, the averaged properties of a referential volume intercepted by a discrete macro-fracture are established. The approach involves volume averaging of gradient of a discontinuous velocity field. The localization law, which relates the velocity jump to the averaged macroscopic strain rate, is obtained by imposing the traction continuity across the discontinuity surface. The constitutive relation, at the level of the referential volume, takes the form [34]

$$\dot{\boldsymbol{\sigma}} = \bar{\mathbb{D}} : \dot{\boldsymbol{\varepsilon}} \tag{3}$$

where the equivalent tangential stiffness operator $\bar{\mathbb{D}}$ is defined as

$$\bar{\mathbb{D}} = \mathbb{D} - \chi\mathbb{D} : \left[\mathbf{n} \otimes (\mathbf{K} + \chi \mathbf{n} \cdot \mathbb{D} \cdot \mathbf{n})^{-1} \otimes \mathbf{n}\right] : \mathbb{D}. \tag{4}$$

Here, $\mathbb{D}$ is the fourth-order stiffness tensor that defines the properties of the intact region, and $\mathbf{K}$ is the second-order stiffness operator for the fractured zone. Moreover, $\mathbf{n}$ is the normal to the discontinuity surface, while χ is a *length scale parameter* defined as the ratio of the surface area of the localization plane to the referential volume at the level of a finite element.

In the mesoscale simulations conducted here, two primary constituents were considered, viz. brick material and the brick-mortar bond. The latter was perceived as being embedded in the adjacent continuum and its properties were described by constitutive law (3). This is a simple and pragmatic approach which is numerically very efficient, as the simulations may be carried out using a simple structured FE mesh [33]. The brick material itself was considered as elastic prior to onset of fracture. It is noted that in masonry the irreversible deformation comes primarily from sliding/separation along the brick-mortar interfaces, so that this simplification seems reasonable. In the range of homogenous deformation, the conditions at failure were described using Mohr-Coulomb criterion with Rankine cut-off in tension regime. After the inception of a macrocrack, the response of the brick material was modeled using again the CLED formulation (4), in which $\mathbf{n}$ refers to the normal to the macrocrack. The crack propagation was traced using the level-set method. The behaviour along the localization plane, for both the pre-existing brick-mortar interface and the bricks, was described using a relation between the rate of traction and velocity

discontinuity. The latter employed strain-softening, and the stiffness operator **K** was defined within the framework of plasticity.

3.1.1. Mesoscale simulations

Mesoscale simulations were carried out on 360×360 mm masonry panels made of half-scale bricks of the size 115×35×50 mm arranged in running bond pattern with mortar joints of thickness of 10 mm. The structural arrangement was analogous to that used by Page in his comprehensive experimental testing program [31,32]. A uniform structured mesh of 8-noded cubic elements of size 10 mm was used. The original experiments employed biaxial loading imposed on the boundaries of specimens that were prepared at different orientation of bed joints relative to the direction of loading. The numerical simulations were carried out using the same FEM discretization and rotating the boundary traction to the desired orientation. In this way, the remeshing for each individual configuration could be avoided. Fig. 2-a shows the loading conditions corresponding to the experimental setup used in [32], while Figs. 2-b and 2-c show the boundary conditions employed in the FEM simulations. It is noted that in the macroscopic framework, as described in the follow up section, the actual zig-zag failure pattern was approximated by an averaged inclination established with reference to the orientation of bed joints (cf. dashed red line in Fig. 2-b).

The loading conditions consisted of uniaxial tension (UT), uniaxial compression (BC), and biaxial tension-compression (BTC). The ratios of the applied compressive to tensile stress magnitudes, $r = \sigma_c/\sigma_t$, used in BTC cases were equal to $r = 2, 5, 10, 30$, respectively, while the considered orientation of bed joints included $\beta = 0^{\circ}, 22.5^{\circ}, 45^{\circ}, 67.5^{\circ}, 90^{\circ}$. Note that according to this notation, $r = 0$ and $r = \infty$ correspond to UT and UC cases, respectively.

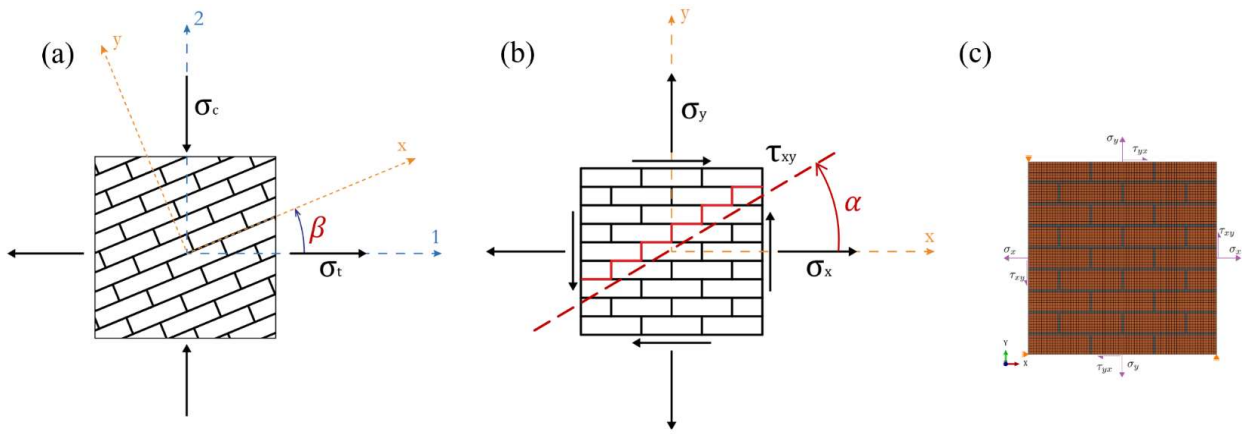

Fig. 2. (a) Biaxial tension-compression with variable orientation of bed joints β; (b) equivalent traction boundary conditions for horizontal bed joints. The zig-zag pattern is a schematic of a failure mechanism approximated by a plane with an average orientation α; (c) FEM mesh and boundary conditions.

The simulations were carried out assuming an elastic strain-softening idealization for the brick-mortar interface. In particular, the Coulomb failure function with tension cut-off has been employed in which the softening effects were attributed to tangential/normal components of irreversible part of velocity discontinuity. As mentioned earlier, the brick material was also considered as elastic prior to onset of localization and the crack propagation was described using representation analogous to that of Eqs. (3)-(4). In this case, exponential degradation functions were used in conjunction with mode I and II fracture energy release. The details pertaining to specification of these functions and the algorithm for a discrete crack tracing within the bricks are provided in [33].

The analysis was focused on predicting the ultimate strength of masonry panels for a broad range of values of tensile and shear strength (cohesion) of brick-mortar interface (f_{ti}, c_i) and the tensile strength of bricks (f_{tb}). The remaining auxiliary material parameters for constituents, viz. elastic properties and the internal friction angles for both the bricks and the bond were selected based on the experimental data [30,32]. The tensile strengths of brick-mortar bond and the brick material were varied within the range of 0.1-1.0 MPa and 0.5-2.0 MPa, respectively, with an interval of 0.1 MPa. The summary of the actual values, which corresponded to a total 80 cases, is provided in Table 1.

The key results of numerical simulations are presented in Fig. 3 which shows the predicted failure envelopes of masonry in tension-compression regime for a number of selected cases. The effect of individual variables on the ultimate strength under biaxial load can be directly assessed by comparing the plots in each row. During the loading process, the increase in external agencies triggers a generation of macrocracks whose pattern depends on the direction of loading in relation to the orientation of bedding planes. The dominant mode is the tensile or shear fracture along the interfaces, however, in some cases (e.g. axial compression) the fracture may extend to bricks as well. The sample fails when the cracks coalescence and a continuous failure mechanism forms. Fig. 4 depicts the global failure patterns and their estimated average orientation under uniaxial loading conditions at different orientation of bed joints.

Table 1. Summary of variable parameters for mesoscale FEM data generation

f_{ti} (MPa)	c_i (MPa)	f_{tb} (MPa)	f_{ti} (MPa)	c_i (MPa)	f_{tb} (MPa)
0.1	0.6 0.8 1.0	0.5 1.0 1.5 2.0	0.6	0.75 1.0 1.3 1.5	1.0 1.5 2.0
0.2	0.4 1.0	0.5 1.0 1.5 2.0	0.7	1.0 1.3 1.5	1.0 1.5 2.0
0.3	0.6 1.0	0.5 1.0 1.5 2.0	0.8	1.15 1.3 1.45	1.0 1.5 2.0
0.4	0.8 1.0 1.4	0.5 1.0 1.5 2.0	0.9	1.15 1.2 1.45	1.0 1.5 2.0
0.5	1.0 1.3 1.5	1.0 1.5 2.0	1.0	1.2 1.3 1.45	1.5 2.0

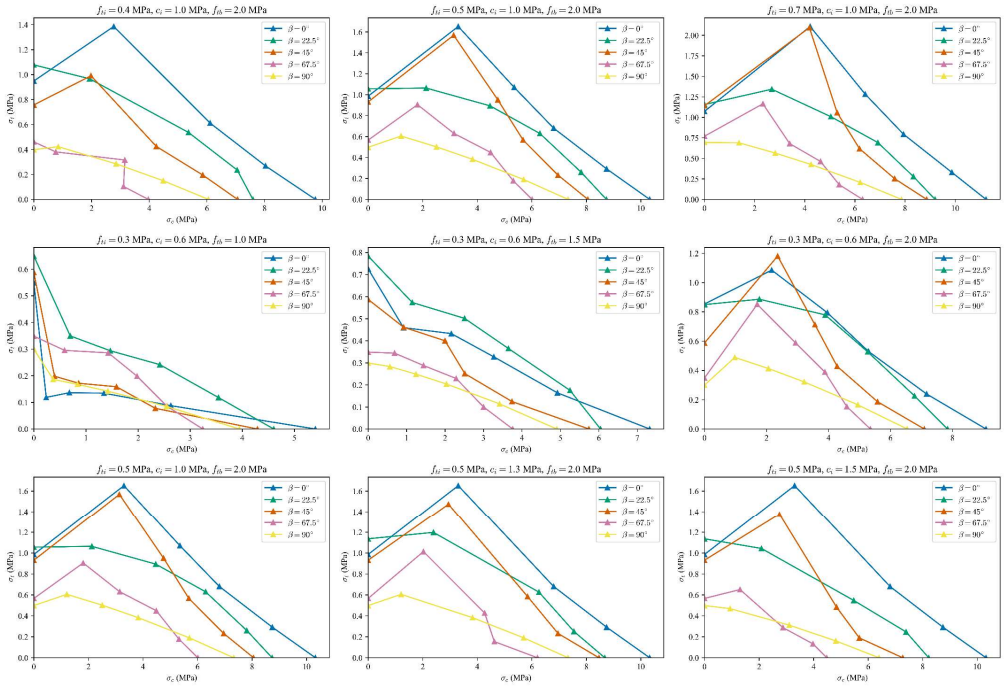

Fig. 3. Sample failure envelopes of masonry panels under biaxial tension-compression. Different colors represent the orientation of bed joints.

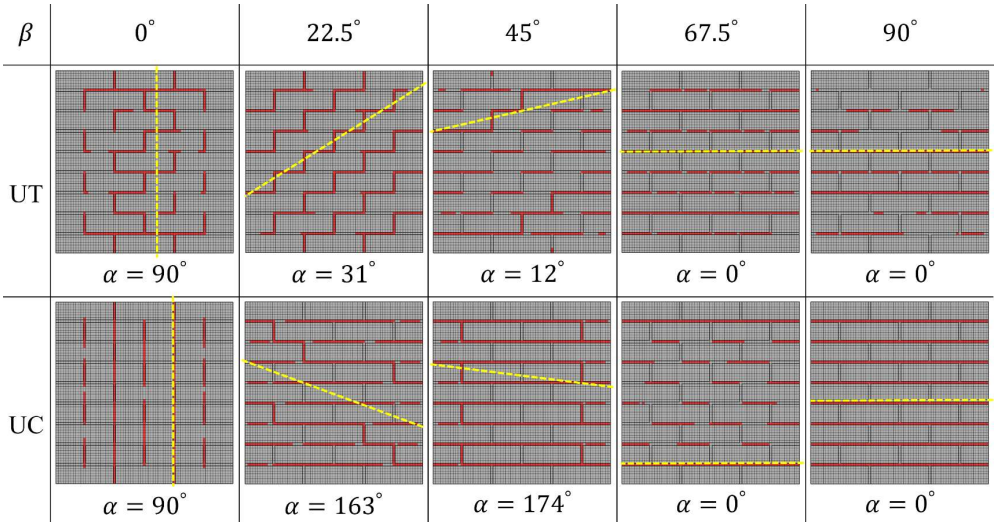

Fig. 4. Average orientation of global failure mechanisms formed in uniaxial tension (UT) and uniaxial compression (UC) at different orientations of bed joints

3.1.2. ANN training and validation

Approximately 75% of the results of mesoscale FEM simulations (i.e. biaxial/uniaxial compression-tension) were randomly selected for training while the reminder was used for testing

the network performance. The input of the network consists of constituent strength properties as well as the bed joint orientation angle and the ratio of compressive to tensile load ($f_{ti}, c_i, f_{tb}, \beta, r$). The outputs are the compressive and tensile strength values at failure (σ_c, σ_t). Since neural networks are trained significantly better by invoking normalization, the data was normalized using the minimum and maximum values of the training set for each given variable. Different network architectures (number of hidden layer and number of neurons in each layer) as well as activation functions were tested in order to find the optimum combination.

For most of the networks tested, the hyperbolic tangent activation function in hidden layers as well a linear activation function in the output layer was used. A case of sigmoid activation function was tested for the sake of comparison. The loss was calculated using the Mean Squared Error (MSE) function optimized using the Adaptive Moment Estimation (Adam) algorithm. Training was performed on roughly 1,700 data points using a batch size (number of samples per gradient update) of 35. Learning rate was reduced exponentially over the maximum number of 50,000 epochs with initial and final values of 10^{-3} and 10^{-5}. The training was stopped before reaching the maximum number of epochs if loss values were below 10^{-8}. Table 2 shows the summary of selected ANNs, while the evolution of their corresponding losses over the training epochs is illustrated in Fig. 5. The ANN predictions of macroscopic failure envelopes at different orientation of bed joints are presented in Fig. 6. The results pertain to a sample set of strength parameters not used for training purposes. The ANN numbers correspond to the network architectures listed in Table 2. It is evident that the results are fairly consistent with those based on mesoscale FEM simulations.

Table 2. Summary of ANN architectures used for predicting strength of masonry

ANN #	Activation Function	Layers	Neurons
ANN 1	Hyperbolic Tangent	3	12
ANN 2	Hyperbolic Tangent	5	15
ANN 3	Hyperbolic Tangent	8	20
ANN 4	Hyperbolic Tangent	10	20
ANN 5	Hyperbolic Tangent	12	36
ANN 6	Sigmoid	5	15

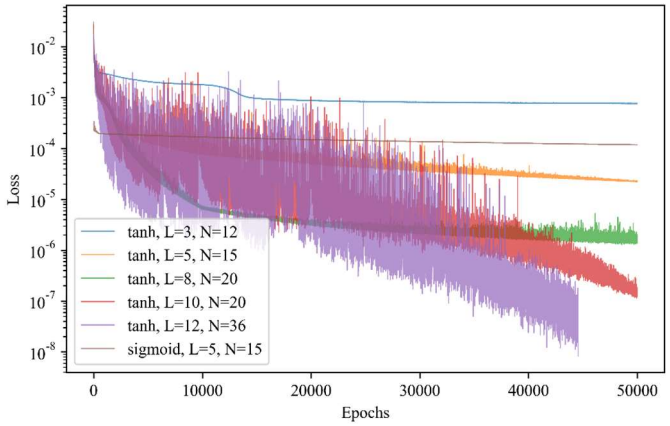

Fig. 5. Evolution of MSE loss values over training epochs for different ANN architectures

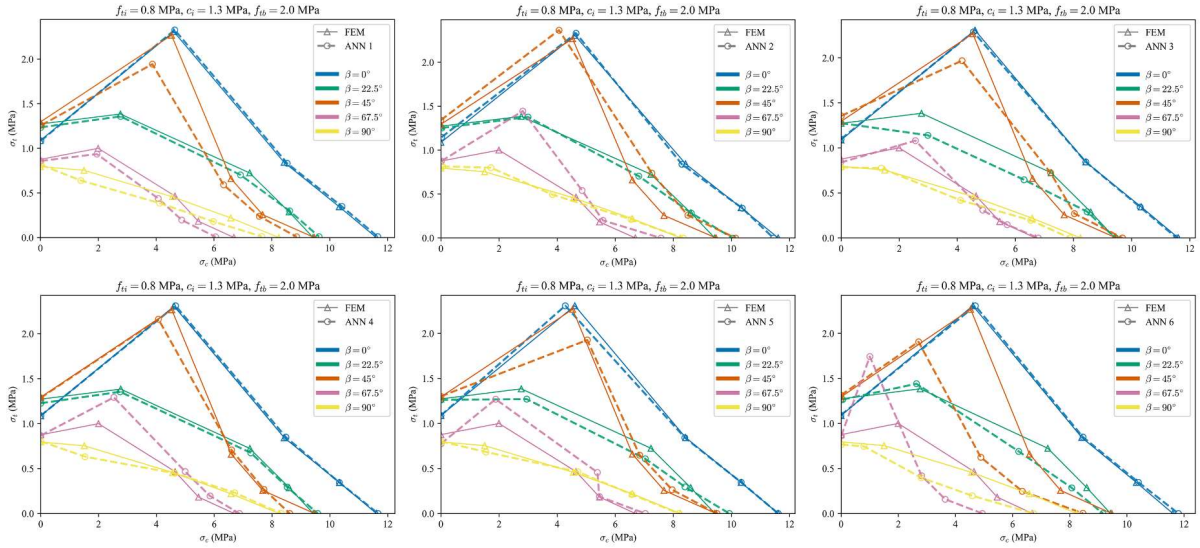

Fig. 6. Examples of ANN predictions of masonry strength compared to mesoscale FEM simulations

3.2. ANN for estimating of average orientation of failure plane

The results of mesoscale analysis were also used in training of another neural network for the assessment of average orientation of failure plane (c.f. Fig. 4). In this case the input consisted of the strength properties of brick-mortar bond, viz. (f_{ti}, c_i), the tensile strength of bricks (f_{tb}) and the components of stress state at failure $(\boldsymbol{\sigma}_f)$. The output were the components of unit vector

normal to the discontinuity plane. Each input vector was normalized using the maximum value of the dataset, while the output vector did not require normalization. The network consisted of 5 hidden layers with 15 neurons using *Hyperbolic Tangent* activation function. Fig. 7 shows an example of neural network predictions for a given set of constituent properties. The information provided by this ANN was explicitly employed in the macroscale framework discussed later in Section 4, in a scenario when the strain localization occurs.

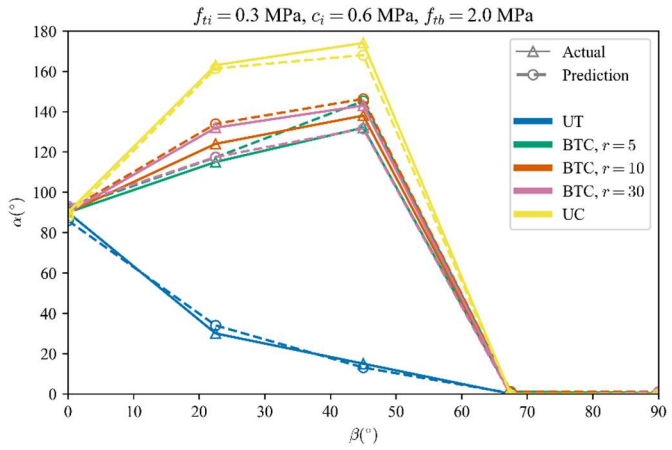

Fig. 7. Example of ANN prediction of average orientation of failure plane with respect to the bedding plane

3.3. Neural network for predicting macroscale elastic properties of masonry

In the present study, an independent neural network was developed to estimate the equivalent elastic properties of masonry based on elastic properties of constituents and their and geometric arrangement. For this purpose, a series of mesoscale uniaxial compression tests parallel and perpendicular to bed joint direction were simulated. The variables in the simulations were Young's moduli of bricks (E_b) and mortar (E_m) and their and Poisson's ratios (ν_b, ν_m). The former variables were chosen in the range of 1.0-10.0 GPa and 0.1-7.0 GPa, respectively, while the corresponding Poisson's ratios were varied between 0.1-0.25 and 0.05-0.2. The geometric variables were the length and heigh of bricks as well as thickness of mortar. The constituents were arranged again in a running bond pattern.

Given the combination of properties above, a total of 1,155 data points were generated. In order to prepare the data for a neural network, the Young's moduli were normalized using their relevant

minimum and maximum values. Additionally, the geometric inputs were represented by ratio of brick height to brick length ($r_b = H_b/L_b$) and mortar thickness to brick height ($r_m = t_m/H_b$) and were used along with the Poisson's ratios as inputs for a neural network with 5 layers including 10 neurons each, with *Hyperbolic Tangent* activation function. Table 3 summarizes the dimensions of constituents and their respective ratios. Assuming a transversely isotropic behaviour for homogenized masonry, the output of the network consisted of equivalent Young's moduli in the direction of bed joints (E_{xx}) and direction of head joints (E_{yy}) as well as the shear modulus G_{xy} and the two corresponding Poisson's ratios.

Table 3. Dimensions of constituents in elastic mesoscale simulations

L_b (mm)	H_b (mm)	t_m (mm)	r_b	r_m
115	35	10	0.30	0.29
190	90	5	0.47	0.06
200	110	15	0.55	0.14
220	70	10	0.32	0.14
250	120	20	0.48	0.17

Approximately 70% of the datapoints were randomly selected for training the network while the remaining data was used for the verification purposes. Fig. 8 shows the ANN predictions of the equivalent Young's moduli for the masonry for 346 testing data points. The maximum error among the predictions was approximately 10%.

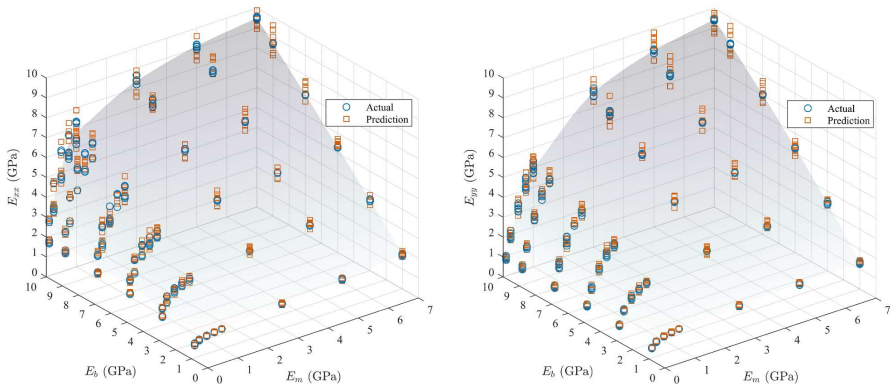

Fig. 8. ANN prediction of transversely isotropic elastic moduli based on elastic properties of bricks and mortar (running bond masonry pattern; x and y refer to direction of bed joints and head joints, respectively).

4. Macroscale approach

In the macroscale approach, masonry is considered as an equivalent continuum with inherent anisotropy. Its mechanical properties are described by implementing the microstructure tensor approach [29], which incorporates scalar anisotropy parameters that are function of the orientation of principal stress axes in relation to the predefined material axes, the latter defined by the arrangement of material microstructure (i.e. orientation of bed/head joints). As mentioned earlier, the approximation coefficients embedded in this representation are identified using the ANN predictions of the ultimate strength in biaxial tests for a given set of properties of constituents.

4.1. Overview of plasticity formulation

In order to maintain the consistency with the underlying mesoscale model, the conditions at failure are defined by Mohr-Coulomb criterion with Rankine cut-off in tensile regime, both functions enhanced by the notion of orientation-dependency of strength parameters. Thus, the failure criterion $F = 0$ assumes the form

$$F = max\,(F_1, F_2) = 0; \quad F_1 = q - \eta_f g_1(\theta)(p + C) = 0; \quad F_2 = g_2(\theta)q - (p + \sigma_t) = 0 \tag{5}$$

where $q = (3\,\mathrm{J}_2)^{1/2}$, $p = -\mathrm{I}_1/3$, $\theta = \frac{1}{3} sin^{-1}\left(\frac{-2}{2}\frac{\mathrm{J}_3}{q^3}\right)$ and

$$g_1(\theta) = \frac{3 - \sin\phi}{2\sqrt{3}\cos\theta - 2\sin\theta\sin\phi};\ \eta_f = \frac{6\sin\phi}{3 - \sin\phi};\ C = \frac{c}{\tan\phi};\quad g_2(\theta) = \frac{2}{3}\sin\left(\theta + \frac{2\pi}{3}\right) \tag{6}$$

where I, J are the basic invariants of the stress tensor and its deviatoric part, respectively, θ is the Lode's angle, ϕ is the friction angle, and c is the cohesion. For an anisotropic material, the parameter C, which is associated with hydrostatic pressure, is a constant while the scalar parameters η_f and σ_t are defined in a polynomial form as

$$\eta_f = \hat{\eta}_f(1 + \xi + b_{c1}\xi^2 + b_{c2}\xi^3 + b_{c3}\xi^4 + \cdots);\quad \sigma_t = \hat{\sigma}_t(1 + \xi + b_{t1}\xi^2 + b_{t2}\xi^3 + b_{t3}\xi^4 + \cdots) \tag{7}$$

Here, b_{ti} and b_{ci} $(i = 1,2, ...)$ are the approximation coefficients while $\xi = \boldsymbol{\ell} \cdot \boldsymbol{A} \cdot \boldsymbol{\ell}$ is the dyadic product of a symmetric traceless tensor $\boldsymbol{A}$, whose principal directions are coaxial with material axes, and a unit 'loading vector' $\boldsymbol{\ell}$. The latter is defined as

$$\boldsymbol{\ell} = \frac{\boldsymbol{L}}{(\boldsymbol{L}\cdot\boldsymbol{L})^{1/2}}, \qquad L_{(i)} = \left(\boldsymbol{t}^{(i)}\cdot\boldsymbol{t}^{(i)}\right)^{1/2} = \left\{\left(\boldsymbol{e}^{(i)}\cdot\boldsymbol{\sigma}\right)\cdot\left(\boldsymbol{e}^{(i)}\cdot\boldsymbol{\sigma}\right)\right\}^{1/2} \tag{8}$$

where $\boldsymbol{L} = L_{(i)}\boldsymbol{e}^{(i)}$ and $\boldsymbol{e}^{(i)}$ are the base vectors of the principal material system ($i = 1,2,3$). Thus, the components of $\boldsymbol{L}$ define the magnitudes of traction vectors $\boldsymbol{t}^{(i)}$ acting on planes perpendicular to the material axes.

Plasticity formulation incorporates the notion of a yield/loading surface which is defined in a functional form similar to that of eq. (5), i.e.

$$f_1 = q - \eta g_1(\theta)(p + C) = 0;\ \eta = \eta(\kappa) = \eta_f \frac{\zeta\kappa}{B + \kappa}; \qquad f_2 = F_2 = 0 \tag{9}$$

where B and ζ are material constants, and κ is the hardening parameter identified with accumulated plastic distortion. The latter is defined in terms of the deviatoric part of plastic strain increment ($\dot{\boldsymbol{e}}^p$) as

$$\kappa = \int \left(\frac{2}{3}\dot{\boldsymbol{e}}^p : \dot{\boldsymbol{e}}^p\right)^{1/2} dt \tag{10}$$

The hardening rule employed in representation (9) implies that $\eta \to \zeta\eta_f$ for $\kappa \to \infty$. Here, the parameter ζ, defined as $\zeta > 1$, is used to determine the onset of localized deformation that is said to occur when $\eta = \eta_f$, so that the conditions of failure are consistent with Mohr-Coulomb criterion (i.e. $f_1 = F_1$). Apparently, other more general criteria may be employed in this respect. In the tensile regime, the material is considered as elastic-brittle with the transition to brittle response occurring at $F_2 = 0$.

The plastic flow is governed by a non-associated flow rule for which the plastic potential is defined as

$$\psi = q + \eta_c g_1(\theta)(p + C)\ln\left(\frac{p+C}{\overline{p}}\right) = 0. \tag{11}$$

Here, η_c is a parameter defining the transition from compaction to dilation and the auxiliary variable $\overline{p}$ is determined from the condition that the current stress state satisfies $\psi = 0$. Note that, in general, there is $\eta_c \sim \eta_f$, so that this parameter may also be perceived as orientation-dependent (cf. Eq. 7).

The constitutive relation, in the range of homogeneous deformation, is formulated following the standard plasticity procedure. The latter entails the use of consistency condition, additivity postulate and the Hooke's law in the range of anisotropic deformation. At the onset of localization, the outward unit vector **n** normal to the discontinuity surface is defined. For that purpose, the ANN described in Section 3.2 is used relating the average orientation of this plane to the stress state and the orientation of material axes. The analysis is then carried out using the CLED formulation analogous to that outlined in Section 3.1.

4.2. Specification of orientation-dependent strength parameters

In order to identify the material functions employed in failure criteria (5) it is convenient to express them in terms of principal stresses. Thus,

$$F_1 = \frac{1}{2}(\sigma_1 - \sigma_2) + \frac{1}{2}(\sigma_1 + \sigma_2)\sin\phi(\xi) - C\sin\phi(\xi) = 0;$$
$$F_2 = \sigma_1 - \sigma_t(\xi) = 0; \quad \sigma_1 > \sigma_3 > \sigma_2 \tag{12}$$

where the tensile stress is considered as positive. Referring now to Fig. 2, the components of loading vector $\boldsymbol{L}$ for plane stress conditions are defined as

$$L_1^2 = \cos^2\beta\,\sigma_1^2 + \sin^2\beta\,\sigma_2^2\,; \quad L_2^2 = \cos^2\beta\,\sigma_2^2 + \sin^2\beta\,\sigma_1^2\,; \quad L_3^2 = 0 \tag{13}$$

and the corresponding components of the unit vector $\boldsymbol{\ell}$ take the form

$$\ell_1^2 = \frac{\cos^2\beta\,\sigma_1^2 + \sin^2\beta\,\sigma_2^2}{\sigma_1^2 + \sigma_2^2}\,; \quad \ell_2^2 = \frac{\cos^2\beta\,\sigma_2^2 + \sin^2\beta\,\sigma_1^2}{\sigma_1^2 + \sigma_2^2} \tag{14}$$

Assume, for simplicity, that masonry under in-plane loading may be considered as a transversely isotropic material. In this case, the principal components of the second-order traceless tensor $\boldsymbol{A}$ satisfy $tr(\boldsymbol{A}) = 0,\ A_2 = A_3$, so that the dyadic product $\xi = \boldsymbol{\ell}\cdot\boldsymbol{A}\cdot\boldsymbol{\ell}$ reduces to

$$\xi = \boldsymbol{\ell}\cdot\boldsymbol{A}\cdot\boldsymbol{\ell} = A_1(\ell_1^2 - 2\ell_2^2) = A_1\left[\frac{\sigma_1^2(1 - 3\sin^2\beta) + \sigma_2^2(1 - 3\cos^2\beta)}{\sigma_1^2 + \sigma_2^2}\right] \tag{15}$$

in which A_1 is the single independent eigenvalue of $\boldsymbol{A}$.

The first step in identification procedure is the specification of material constant C, viz. Eq. (6). Note that C has no direct physical significance as the strength in tension regime is governed by the cut-off criterion $F_2 = 0$ in which $maxF_2 < C$. Thus, an assessment of C is required only to enable the specification of material function $\eta_f(\xi)$. Fig. 9 shows the linear best-fit approximations to a set of data generated through mesoscale simulations for some selected values of constituent properties at different orientation of bed joints. The data is plotted in the affined space $\frac{1}{2}(\sigma_1 - \sigma_2)\ vs.\ \frac{1}{2}|\sigma_1 + \sigma_2|$. In each case, an estimate of C was obtained by taking the maximum value over the set of orientations considered.

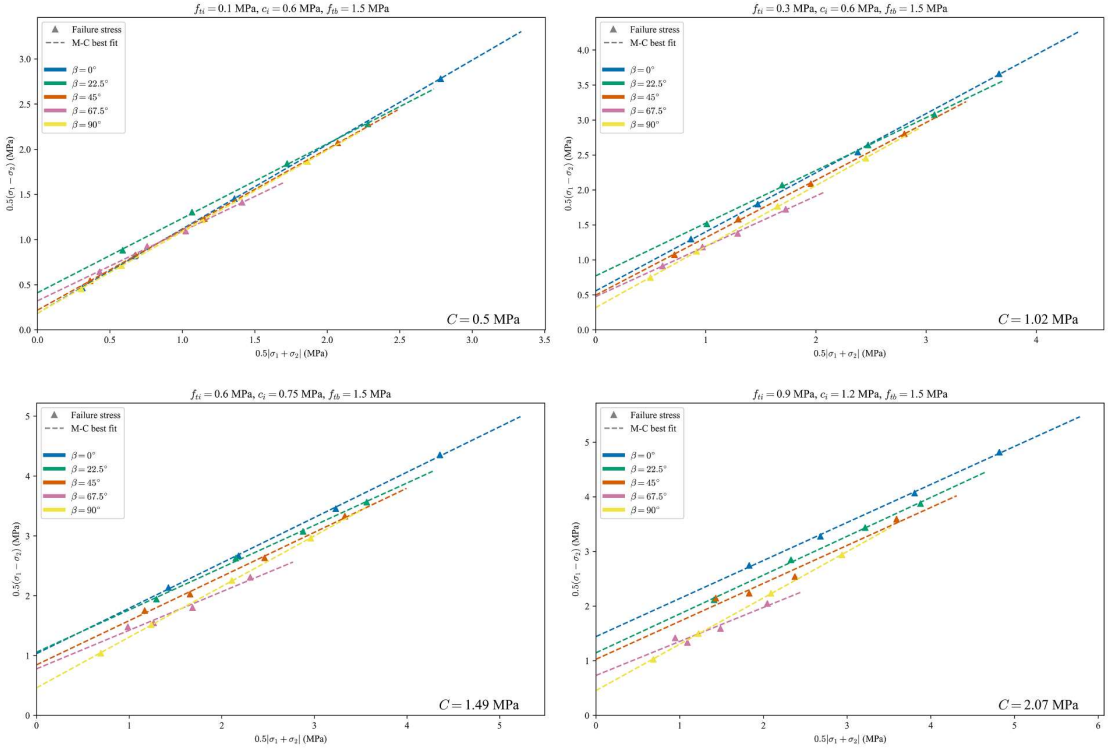

Fig. 9. Examples of Mohr-Coulomb best fit approximations for different bed joint orientations

Given the value of C and the corresponding stress state at failure, the pairs of $\{\eta_f, (\ell_1^2 - 2\ell_2^2)\}$ can be evaluated for the purpose of identification of the function $\eta_f(\xi)$. This is illustrated in Fig. 10, which shows the best-fit approximations to this function over the selected range of values of the constituent properties.

In order to complete the identification procedure, the spatial distribution of tensile strength of masonry $\sigma_t(\xi)$ needs to be determined. This is achieved by best fitting the results of uniaxial tension tests, generated again through mesoscale simulations, for masonry panels at different orientations of bed joints. It should be noted that for the uniaxial tension there is $\ell_1^2 - 2\ell_2^2 = 1 - 3\cos^2\beta$, so that the variation of tensile strength can be plotted explicitly against the orientation of bed joints, viz. the angle β, as shown in Fig. 11. The summary of the set of fourth order polynomial approximation coefficients for the selected examples is provided in Table 4.

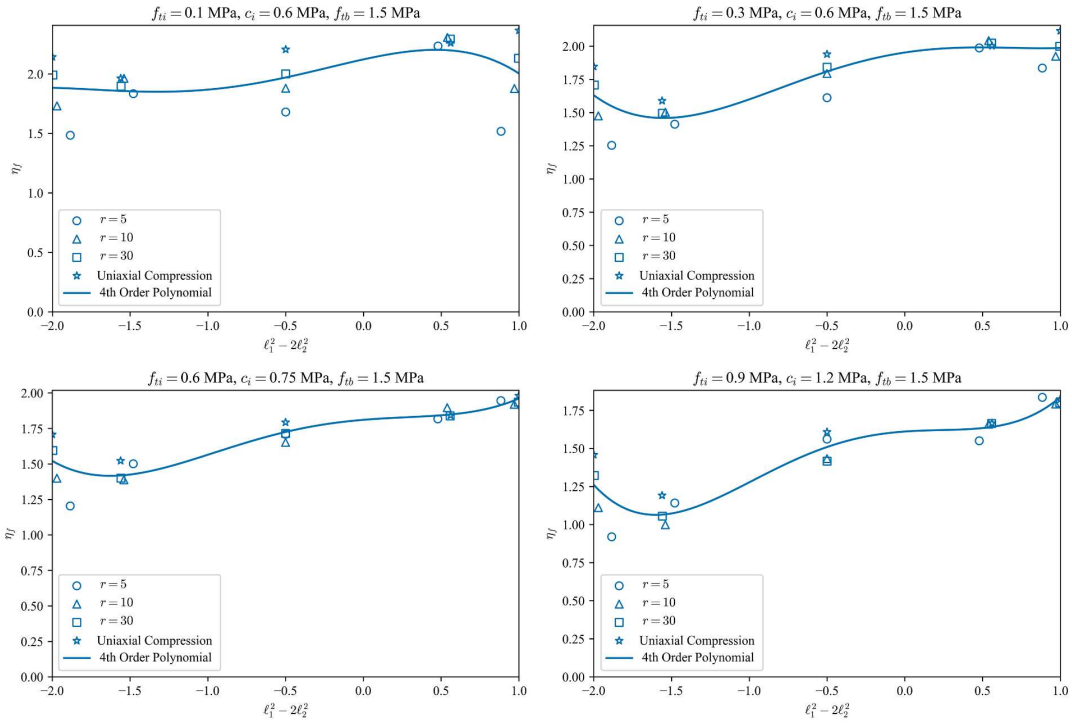

Fig. 10. Examples of best-fit approximations of function $\eta_f(\xi)$

Table 4. Coefficients of best-fit approximation of material functions $\eta_f(\xi)$ and $\sigma_t(\xi)$ for selected examples

f_{tm} (MPa)	c_m (MPa)	f_{tb} (MPa)	$\hat{\eta}_f$	A_{c1}	b_{c1}	b_{c2}	b_{c3}	$\hat{\sigma}_t$ (MPa)	A_{t1}	b_{t1}	b_{t2}	b_{t3}
0.1	0.6	1.5	2.122	0.135	-3.382	-41.952	-79.359	0.132	-0.533	3.041	2.325	-2.715
0.3	0.6	1.5	1.952	0.091	-13.997	10.959	499.670	0.458	-0.518	0.492	-0.482	-0.387
0.6	0.75	1.5	1.811	0.050	-27.789	469.803	6857.848	0.743	-0.196	-0.514	0.238	-12.960
0.9	1.2	1.5	1.611	0.045	-58.687	1394.272	20727.191	1.178	-0.310	-1.181	-4.494	5.153

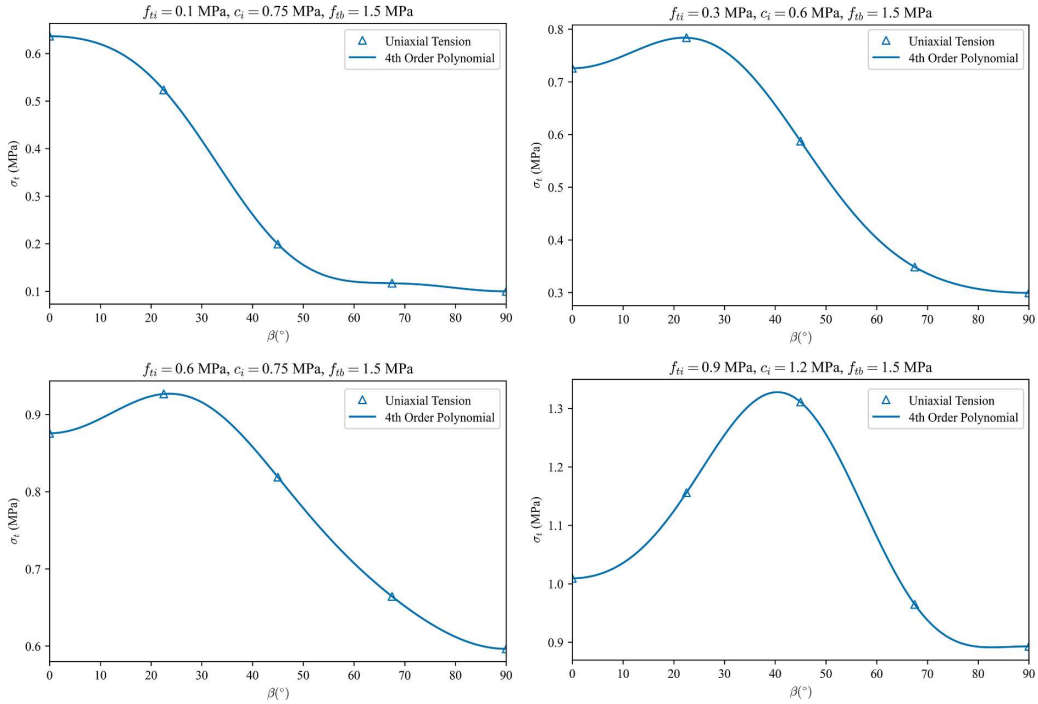

Fig. 11. Examples of best-fit approximations of $\sigma_t(\xi)$ function

(i) Verification of predictions based on ANN

In practical implementations, the same identification procedure may be followed using the ANN generated data, instead of mesoscale FEM simulations. In this way, the approximation coefficients appearing in both material functions $\eta_f(\xi)$ and $\sigma_t(\xi)$ can be specified directly from a prescribed set of basic strength properties of bricks and brick-mortar bond. This is illustrated in Figs. 12-13, which compares the best-fit approximations generated using ANN predictions and those obtained from FEM simulations. Apparently, the degree of accuracy is fairly reasonable here.

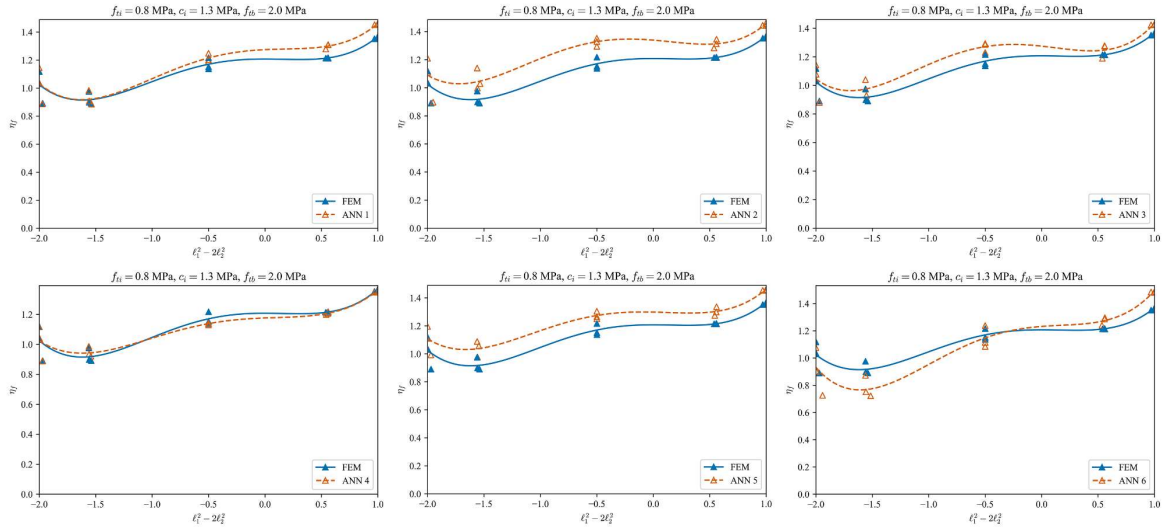

Fig. 12. Best-fit approximations of function $\eta_f(\xi)$ using the ultimate strength predictions of different ANN architectures

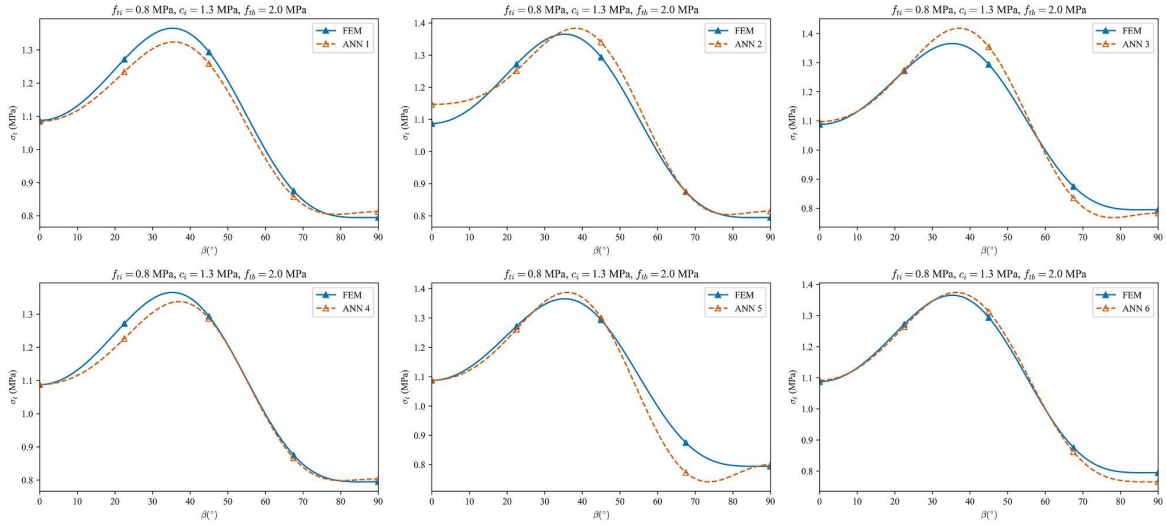

Fig. 13. Best-fit approximations of function $\sigma_t(\xi)$ using the ultimate strength predictions of different ANN architectures

4.3. Specification of parameters governing the deformation at macroscale

Description of the deformation process at macroscale requires the specification of anisotropic elastic constants as well as the parameters governing the deformation in the elastoplastic range,

viz. Eqs. (9-11). The equivalent elastic properties of masonry are estimated using the trained neural network as described in Section 3.3, which estimates their values based on properties of bricks and mortar joints and their geometric arrangement.

The definition of the plastic potential function, viz. Eq. (11), requires the identification of parameter η_c which governs the onset of dilatancy. As mentioned earlier, the transition from compaction to dilatancy is strongly correlated with the conditions of global failure, implying that $\eta_c \rightarrow \eta_f$. Given this fact, it was assumed that $\eta_c = \eta_c(\xi) = 0.99\,\eta_f(\xi)$.

The hardening parameter B, Eq. (9), may also exhibit a directional dependency. However, given the fact that the predominant effect of anisotropy is the orientation-dependence of strength properties, which in itself affects the deformation response, its value was assumed here to remain constant. It should be emphasized that this is a pragmatic simplification and there is no conceptual difficulty in considering this parameter as a spatial variable. For a given set of constituent properties, the value of B has been assessed by finding the best-fit approximation to a set of virtual (mesoscale FEM) data plotted in the affine space $\{\eta, \kappa\}$. Note that the latter requires the notion of additivity of the rates of elastic and plastic deviatoric strain for assessing the values of κ, viz. Eq. (10). As an illustration, Fig. 14 shows the deviatoric stress-strain characteristics for UC tests obtained from mesoscale FEM analyses and macroscale point-integration scheme. The results correspond to constant values of parameter B and $\eta_f(\xi)$ approximated using only UC load tests for each given combination of constituent properties.

Finally, for the purpose of practical engineering applications, another auxiliary ANN has been developed which enables specification of the value of hardening parameter B for a given set of constituent properties. In this case, approximately 70% of the mesoscale FEM data was used for training purposes while the remaining set was utilized for the verification process. The network consisted of 3 layers with 10 neurons each, using the *Hyperbolic Tangent* activation function. The summary of all neural networks used for bridging meso and macroscale, including the one used for specification of the average orientation of discontinuity plane, is presented in Fig. 15.

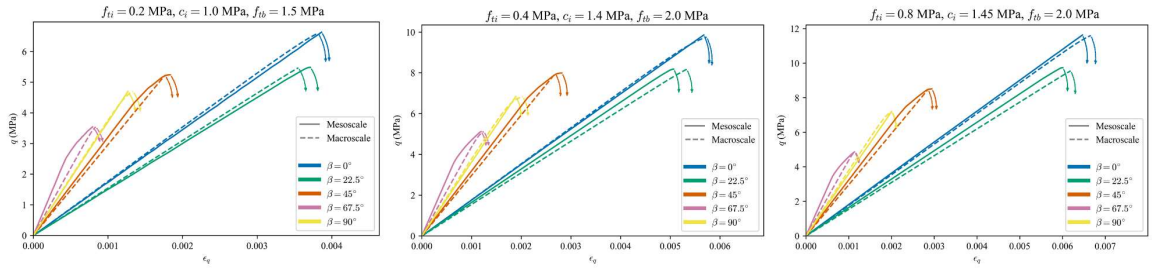

Fig. 14. Comparison between mesoscale and macroscale simulations of uniaxial compression tests for $\eta_f(\xi)$ approximated using UC tests only. From left to right, $B = 1.2 \times 10^{-6}, 1.5 \times 10^{-6}, 2.1 \times 10^{-6}$.

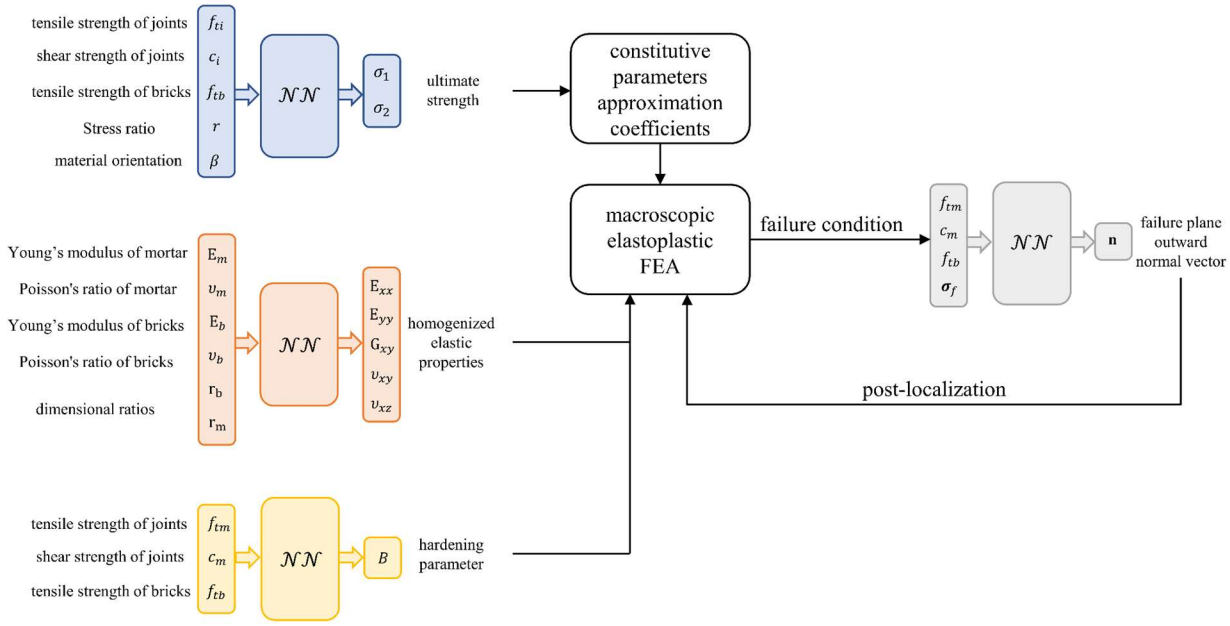

Fig. 15. Overview of the proposed procedure for macroscale analysis of masonry structures.

5. Numerical example

In this section, the proposed computational framework has been applied to finite element analyses of a large masonry wall with multiple window openings. It is noted that the main limitation in terms of verification of the macroscale approach is the lack of relevant experimental data, which stems from the scale of the problem. Therefore, in this work the performance of the macroscale

approach was assessed by comparing the results with a detailed mesoscale analysis which was used as a benchmark.

The analysis involved an unreinforced masonry wall with the span of 43.5 m, the height of 15m and the thickness of 0.3m. The structure incorporated two rows of large openings with dimensions of 1.5m x 1.9m, cf. Fig. 16. In the numerical analysis, the wall was fixed at the base and was initially subjected to a gravitational load corresponding to unit weight of 20 kN/m^3, as well as a uniformly distributed vertical load of 60 kN/m applied at the top. In the second stage, a lateral load was applied at the top of the wall until the ultimate conditions were reached. The same geometry and boundary conditions were used for both the mesoscale and macroscale analysis. The analyses were performed in a load-controlled setting and the evolution of horizontal displacement at the point of lateral load application was recorded.

(i) Mesoscale model

The bricks had the dimensions of 200mm×100mm and were arranged in a running-bond pattern. The elastic and strength properties of constituents are reported in Table 5. The mesh for the finite element analyses was structured by progressively increasing the element size with the distance from mortar joints. The geometry of the wall and details of the FEM discretization are shown in Fig. 16. A total of 1,104,863 8-noded cubic elements were used in the analysis.

Table 5. Constituent properties for mesoscale simulations

	Bricks	Brick-mortar bond
Young's Modulus, E (MPa)	6750	N/A
Poisson's ratio, υ	0.17	N/A
Tensile Strength, f_t (MPa)	2.0	0.2
Angle of internal friction, ϕ (◦)	35	35
Cohesion, c (MPa)	4.0	0.4
Interface normal stiffness, k_n (N/m)	N/A	1.3×10^8
Interface shear stiffness, k_t (N/m)	N/A	6.2×10^8

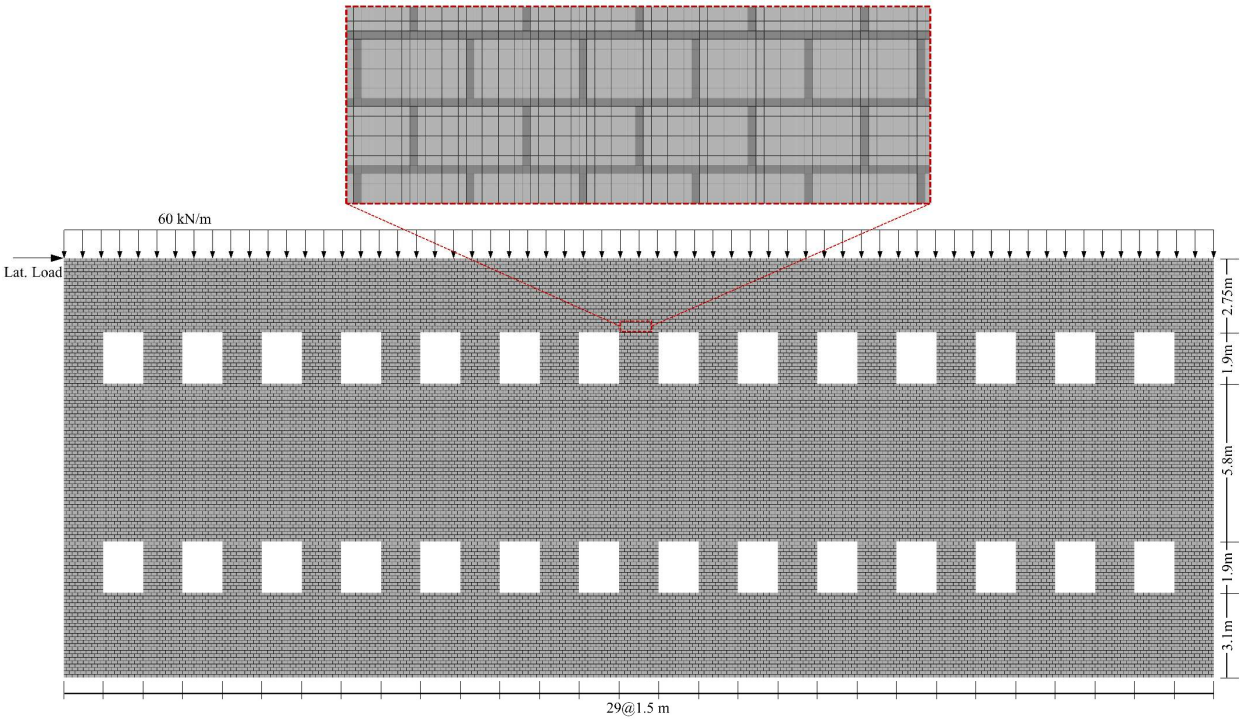

Fig. 16. Geometry of the wall and arrangement of bricks for mesoscale FEM simulations. A magnified sample of the FEM mesh is shown.

Macroscale model

The discretization of the macroscale finite element model of the wall incorporated an element size of 0.75m, which covers a similar number of bricks as that used in the mesoscale analyses of masonry panels (Fig. 17). A finer mesh consisting of cubic elements with the size of 0.5m was also used in order to investigate the sensitivity of the model to mesh size. The number of 8-node cubic elements for coarse and fine mesh configurations were 1,108 and 2,448, respectively.

The elastic properties at the macroscale were assumed to be transversely isotropic and were obtained using the trained neural network described in Section 3.2. A complete set of material parameters, which includes the approximation coefficients for the strength variables, is reported in Table 6.

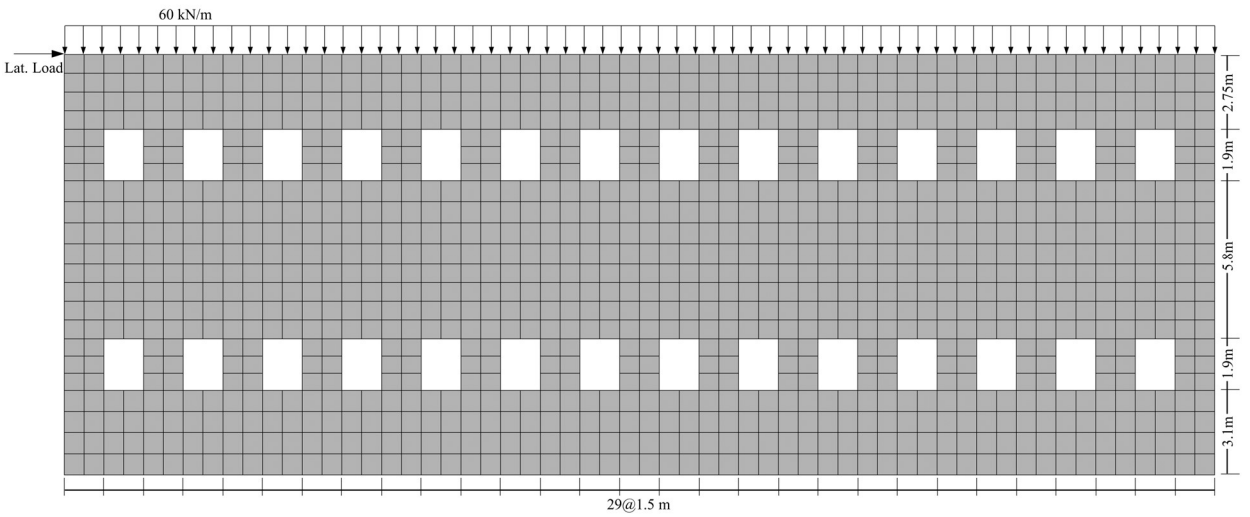

Fig. 17. Geometry of the wall and FEM mesh for macroscale simulations.

Table 6. Model parameters used for macroscale FEM simulations

Elastic Properties		Mohr-Coulomb		Tension cut-off		Hardening	
E_x (MPa)	5090	$\hat{\eta}_f$	1.984	$\hat{\sigma}_t$ (MPa)	0.269	ζ	1.025
E_y (MPa)	5370	A_{c1}	0.152	A_{t1}	-0.551	B	1.2×10^{-6}
ν_{xy}	0.12	b_{c1}	-5.684	b_{t1}	2.453		
ν_{xz}	0.14	b_{c2}	2.251	b_{t2}	1.079		
G_{xy} (MPa)	2270	b_{c3}	86.675	b_{t3}	-2.935		

Once the conditions of failure were met, the stress components were input into the ANN developed in Section 3.1.3 to estimate the orientation of the failure plane. In order to facilitate the online application of the trained network in macroscale FEM simulations, a Fortran-Keras Deep Learning Bridge [52] was employed to transfer data between the FEM and ANN. The post-localization behaviour was then modeled using CLED formulation (cf. Eqs. 3-4) with a smeared crack approach. The strength properties along the macrocrack were progressively reduced using an exponential degradation function defined in terms of opening/sliding along the discontinuity plane. The mathematical form of these functions was analogous to that employed in the mesoscale formulation (cf. [33]).

The results of numerical simulations are presented in Figs. 18-19 below. During the initial loading stages, the damaged zones started to form around the corners of the openings. These zones then expanded between the openings and bottom left corner of the wall. Finally, ultimate shear capacity was reached when damage regions propagated between the two rows of openings and the top and bottom section of the wall. The evolution of failure pattern obtained from meso and macroscale analyses is compared in Fig. 18. The relation between the displacement measured at the top of the wall and the lateral shear force applied is shown in Fig. 19. For the mesoscale model, the ultimate value of the shear force was 6400 kN. On the other hand, the values based on macroscale models with coarse and fine mesh were equal to 5750 kN and 5840 kN, respectively, which represents approximately 8-10% error.

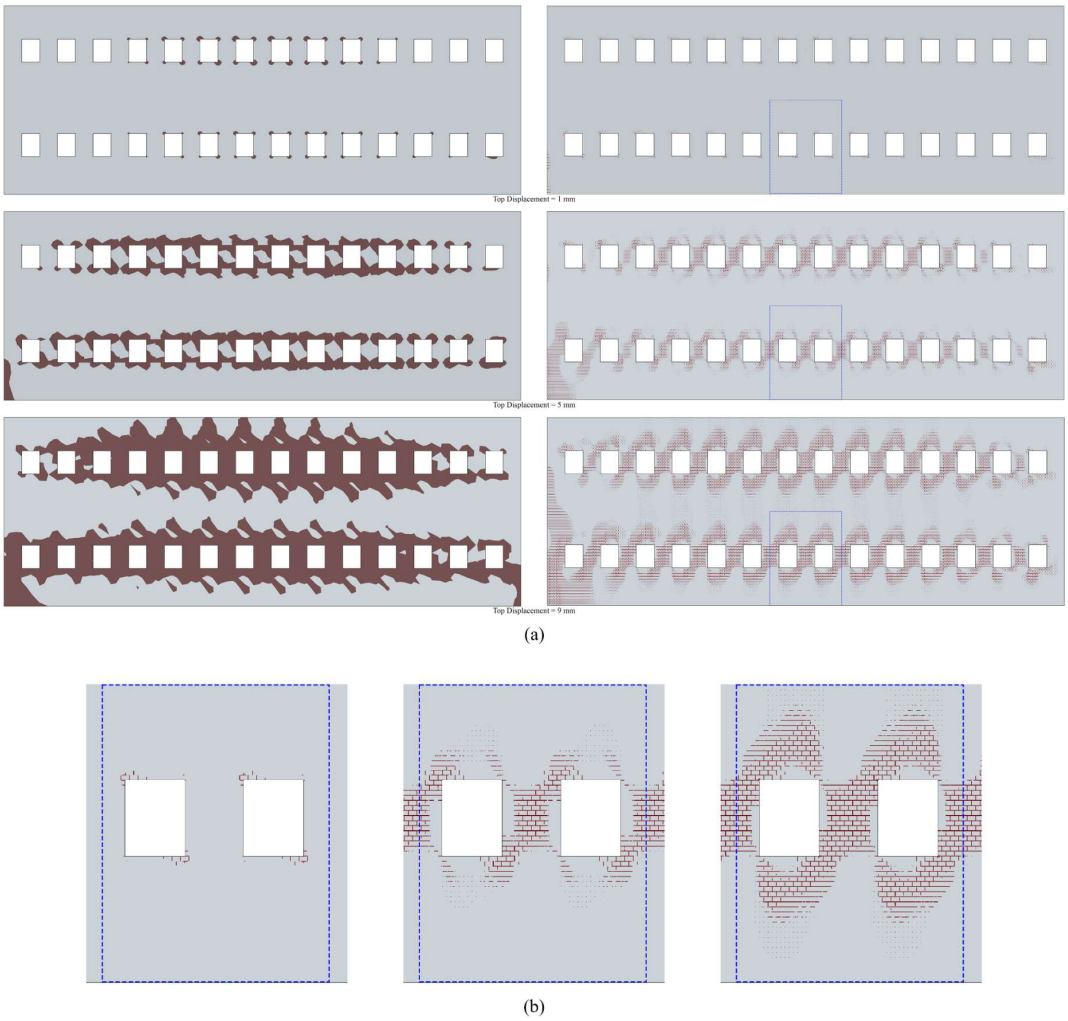

Fig. 18. (a) Comparison between mesoscale (right) and macroscale (left) progression of material failure (colored in red). (b) Magnified sections of the mesoscale model.

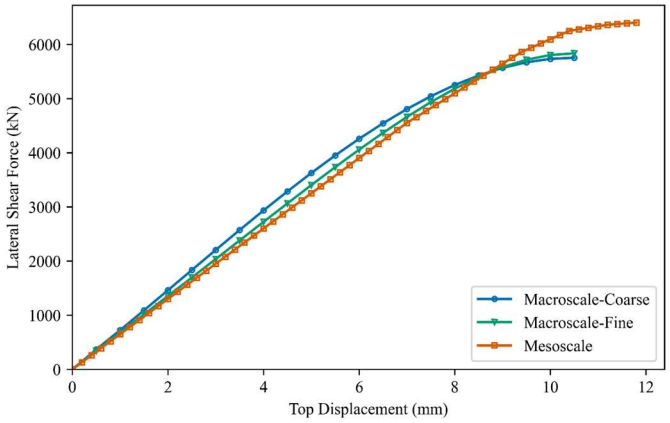

Fig. 19. Comparison between load-deformation characteristics of mesoscale and macroscale models. Coarse element size:0.75m, fine element size: 0.5m

6. Summary and discussions

In order to assist in an effective implementation of a continuum framework in analysis of large-scale masonry structures, a series of artificial neural networks were trained in which the material properties of constituents were used to predict the 'equivalent' macroscopic characteristics of masonry. The following steps summarize the present approach:

i. Mesoscale finite element analyses of masonry panels under biaxial tension-compression were conducted, using variable constituent properties and bed joint orientations, in order to generate 'virtual data' comprising the load-displacement characteristics, ultimate strength, and the average orientation of macrocracks at the failure.

ii. Artificial neural networks were trained and tested using this data set to predict the ultimate strength of masonry as well as the averaged orientation of global failure plane for a given a set of constituent properties and loading conditions.

iii. Using the information on the ultimate strength, the approximation coefficients were identified for the polynomial functions that estimate the orientation-dependent strength parameters for macroscale constitutive model.

iv. Mesoscale finite element analyses of masonry panels were conducted in elastic range to estimate the transversely isotropic properties for macroscale masonry model.

v. Using these results, an artificial neural network was trained and tested for predicting 'equivalent' elastic properties for a given combination of elastic and geometric properties of constituents.
vi. Hardening parameters of macroscopic plasticity formulation were estimated using the averaged deformation characteristics of mesoscale finite element simulations of step (i).
vii. An artificial neural network was trained to predict the hardening parameter of macroscale model based on a given set of constituent properties.

With the trained networks, all necessary parameters for macroscale model can be explicitly obtained from mechanical properties of constituents without the need for mesoscale analysis. The example provided in the last section showed a fairly good agreement between the results of macro and mesoscale analysis, the former requiring significantly less computational effort. The growth of fractured zones in mesoscale model may seem to be ahead of that in the macroscale model only because of the difference in scale between the relevant element sizes. However, the main characteristics of the fracture pattern, i.e. the formation of fractured zones in the corners of the wall, between the two rows of openings, and in the vicinity of the openings show quite a good agreement between the two models. The agreement is even more evident when comparing the load-displacement response; the stiffness and the ultimate load are very similar in both methodologies.

In the present study, the primary function of the developed neural networks is the bridging between meso and macroscale masonry models. Apparently, more comprehensive 'virtual data' generation scheme may be incorporated, in which more variables and more complex geometrical arrangements of masonry are considered. Consequently, the architecture of the networks and input and output vectors can be changed to reflect the availability of data.

One of the advantages of the present approach, compared to other hybrid FEM-ANN schemes, is that the neural networks are external to the macroscale simulations. The only ANN that is explicitly embedded in the analysis is that employed for the assessment of the orientation of localization plane. The latter, however, is used only once at a given integration point at the onset of failure. This is in contrast to other approaches where neural networks are called at every load increment during the numerical analysis.

7. References

[1] Anthoine A. Derivation of the in-plane elastic characteristics of masonry through homogenization theory. Int J Solids Struct 1995;32:137–63. https://doi.org/10.1016/0020-7683(94)00140-R.

[2] Urbanski A, Szarlinski J, Kordecki Z. Finite element modeling of the behavior of the masonry walls and columns by homogenization approach. Comput Methods Struct Mason 1995;3:32–41.

[3] Sacco E. A nonlinear homogenization procedure for periodic masonry. Eur J Mech - ASolids 2009;28:209–22. https://doi.org/10.1016/j.euromechsol.2008.06.005.

[4] de Buhan P, de Felice G. A homogenization approach to the ultimate strength of brick masonry. J Mech Phys Solids 1997;45:1085–104. https://doi.org/10.1016/S0022-5096(97)00002-1.

[5] Cluni F, Gusella V. Homogenization of non-periodic masonry structures. Int J Solids Struct 2004;41:1911–23. https://doi.org/10.1016/j.ijsolstr.2003.11.011.

[6] Lourenço PB, Milani G, Tralli A, Zucchini A. Analysis of masonry structures: review of and recent trends in homogenization techniquesThis article is one of a selection of papers published in this Special Issue on Masonry. Can J Civ Eng 2007;34:1443–57. https://doi.org/10.1139/L07-097.

[7] Costa AA, Arêde A, Campos Costa A, Penna A, Costa A. Out-of-plane behaviour of a full scale stone masonry façade. Part 1: specimen and ground motion selection. Earthq Eng Struct Dyn 2013;42:2081–95. https://doi.org/10.1002/eqe.2313

[8] Costa AA, Arêde A, Costa AC, Penna A, Costa A. Out-of-plane behaviour of a full scale stone masonry façade. Part 2: shaking table tests. Earthq Eng Struct Dyn 2013;42:2097–111. https://doi.org/10.1002/eqe.2314

[9] Magenes G, Penna A, Galasco A. A full-scale shaking table test on a two-storey stone masonry building. 14th Eur Conf Earthq Eng Ohrid 2010.

[10] Magenes G, Penna A, Senaldi IE, Rota M, Galasco A. Shaking Table Test of a Strengthened Full-Scale Stone Masonry Building with Flexible Diaphragms. Int J Archit Herit 2014;8:349–75. https://doi.org/10.1080/15583058.2013.826299.

[11] Mazzon N. Influence of grout injection on the dynamic behaviour of stone masonry buildings. PhD Thesis. University of Padova, 2010.

[12] Salonikios T, Karakostas C, Lekidis V, Anthoine A. Comparative inelastic pushover analysis of masonry frames. Eng Struct 2003;25:1515–23. https://doi.org/10.1016/S0141-0296(03)00118-4.

[13] Lourenço PB, Rots JG, Blaauwendraad J. Continuum Model for Masonry: Parameter Estimation and Validation. J Struct Eng 1998;124:642–52. https://doi.org/10.1061/(ASCE)0733-9445(1998)124:6(642).

[14] Gambarotta L, Lagomarsino S. Damage Models for the Seismic Response of Brick Masonry Shear Walls. Part Ii: The Continuum Model and Its Applications. Earthq Eng Struct Dyn 1997;26:441–62. https://doi.org/10.1002/(SICI)1096-9845(199704)26:4<441::AID-EQE651>3.0.CO;2-0.

[15] Brasile S, Casciaro R, Formica G. Multilevel approach for brick masonry walls – Part I: A numerical strategy for the nonlinear analysis. Comput Methods Appl Mech Eng 2007;196:4934–51. https://doi.org/10.1016/j.cma.2007.06.021.

[16] Brasile S, Casciaro R, Formica G. Multilevel approach for brick masonry walls – Part II: On the use of equivalent continua. Comput Methods Appl Mech Eng 2007;196:4801–10. https://doi.org/10.1016/j.cma.2007.06.020.
[17] Masiani R, Trovalusci P. Cosserat and Cauchy materials as continuum models of brick masonry. Meccanica 1996;31:421–32. https://doi.org/10.1007/BF00429930.
[18] Pietruszczak S, Niu X. A mathematical description of macroscopic behaviour of brick masonry. Int J Solids Struct 1992;29:531–46. https://doi.org/10.1016/0020-7683(92)90052-U
[19] Mori T, Tanaka K. Average stress in matrix and average elastic energy of materials with misfitting inclusions. Acta Metall 1973;21:571–4. https://doi.org/10.1016/0001-6160(73)90064-3
[20] Maier G, Nappi A, Papa E. Damage models for masonry as a composite material: a numerical and experimental analysis. Const Laws Eng Mater 1991:427–32.
[21] Plevris V, Asteris PG. Modeling of masonry failure surface under biaxial compressive stress using Neural Networks. Constr Build Mater 2014;55:447–61. https://doi.org/10.1016/j.conbuildmat.2014.01.041.
[22] Asteris PG, Plevris V. Anisotropic masonry failure criterion using artificial neural networks. Neural Comput Appl 2017;28:2207–29. https://doi.org/10.1007/s00521-016-2181-3.
[23] Aguilar V, Sandoval C, Adam JM, Garzón-Roca J, Valdebenito G. Prediction of the shear strength of reinforced masonry walls using a large experimental database and artificial neural networks. Struct Infrastruct Eng 2016;12:1661–74. https://doi.org/10.1080/15732479.2016.1157824.
[24] Zhou Q, Zhu F, Yang X, Wang F, Chi B, Zhang Z. Shear capacity estimation of fully grouted reinforced concrete masonry walls using neural network and adaptive neuro-fuzzy inference system models. Constr Build Mater 2017;153:937–47. https://doi.org/10.1016/j.conbuildmat.2017.07.171.
[25] Carozza S, Cimmino M. Artificial neural network implementation for masonry compressive strength estimation. Proc Inst Civ Eng - Struct Build 2020;173:635–45. https://doi.org/10.1680/jstbu.18.00089.
[26] Asteris PG, Argyropoulos I, Cavaleri L, Rodrigues H, Varum H, Thomas J, et al. Masonry Compressive Strength Prediction Using Artificial Neural Networks. In: Moropoulou A, Korres M, Georgopoulos A, Spyrakos C, Mouzakis C, editors. Transdiscipl. Multispectral Model. Coop. Preserv. Cult. Herit., Cham: Springer International Publishing; 2019, p. 200–24. https://doi.org/10.1007/978-3-030-12960-6_14.
[27] Garzón-Roca J, Marco CO, Adam JM. Compressive strength of masonry made of clay bricks and cement mortar: Estimation based on Neural Networks and Fuzzy Logic. Eng Struct 2013;48:21–7. https://doi.org/10.1016/j.engstruct.2012.09.029.
[28] Pietruszczak S, Mroz Z. Formulation of anisotropic failure criteria incorporating a microstructure tensor. Comput Geotech 2000;26:105–12. https://doi.org/10.1016/S0266-352X(99)00034-8
[29] Pietruszczak S, Mroz Z. On failure criteria for anisotropic cohesive-frictional materials. Int J Numer Anal Methods Geomech 2001;25:509–24. https://doi.org/10.1002/nag.141
[30] Dhanasekar M, Kleeman PW, Page AW. Biaxial stress-strain relations for brick masonry. J Struct Eng U S 1985;111:1085–100. https://doi.org/10.1061/(ASCE)0733-9445(1985)111:5(1085).

[31] Page AW. The biaxial compressive strength of brick masonry. Proc Inst Civ Eng 1981;71:893–906. https://doi.org/10.1680/iicep.1981.1825.
[32] Page AW. The strength of brick masonry under biaxial tension-compression. Int J Mason Constr 1983;3:26–31.
[33] Koocheki K, Pietruszczak S, Haghighat E. A computational framework for meso and macroscale analysis of structural masonry. Int J Solids Struct 2022;236–237:111342. https://doi.org/10.1016/j.ijsolstr.2021.111342.
[34] Pietruszczak S. On homogeneous and localized deformation in water-infiltrated soils. Int J Damage Mech 1999;8:233–53. https://doi.org/10.1177%2F105678959900800302
[35] Haghighat E, Pietruszczak S. On modeling of discrete propagation of localized damage in cohesive-frictional materials. Int J Numer Anal Methods Geomech 2015;39:1774–90. https://doi.org/10.1002/nag.2368
[36] Rosenblatt F. The perceptron: a probabilistic model for information storage and organization in the brain. Psychol Rev 1958;65:386. https://psycnet.apa.org/doi/10.1037/h0042519
[37] Haykin S. Neural Networks and Learning Machines. 3rd Edition. Pearson; 2009.
[38] Russell S.J., Norvig P., Canny J.F., Malik J.M., Edwards D.D. Artificial intelligence: a modern approach. Prentice Hall 1995.
[39] Jang DP, Fazily P, Yoon JW. Machine learning-based constitutive model for J2- plasticity. Int J Plast 2021;138:102919. https://doi.org/10.1016/j.ijplas.2020.102919.
[40] Karapiperis K, Stainier L, Ortiz M, Andrade JE. Data-Driven multiscale modeling in mechanics. J Mech Phys Solids 2021;147:104239. https://doi.org/10.1016/j.jmps.2020.104239.
[41] Kirchdoerfer T, Ortiz M. Data-driven computational mechanics. Comput Methods Appl Mech Eng 2016;304:81–101. https://doi.org/10.1016/j.cma.2016.02.001.
[42] Mozaffar M, Bostanabad R, Chen W, Ehmann K, Cao J, Bessa MA. Deep learning predicts path-dependent plasticity. Proc Natl Acad Sci 2019;116:26414–20. https://doi.org/10.1073/pnas.1911815116.
[43] Settgast C, Hütter G, Kuna M, Abendroth M. A hybrid approach to simulate the homogenized irreversible elastic–plastic deformations and damage of foams by neural networks. Int J Plast 2020;126:102624. https://doi.org/10.1016/j.ijplas.2019.11.003.
[44] Bock FE, Aydin RC, Cyron CJ, Huber N, Kalidindi SR, Klusemann B. A Review of the Application of Machine Learning and Data Mining Approaches in Continuum Materials Mechanics. Front Mater 2019;6.
[45] Tao F, Liu X, Du H, Yu W. Learning composite constitutive laws via coupling Abaqus and deep neural network. Compos Struct 2021;272:114137. https://doi.org/10.1016/j.compstruct.2021.114137.
[46] Zhang X, Garikipati K. Machine learning materials physics: Multi-resolution neural networks learn the free energy and nonlinear elastic response of evolving microstructures. Comput Methods Appl Mech Eng 2020;372:113362. https://doi.org/10.1016/j.cma.2020.113362.
[47] Fernández M, Rezaei S, Rezaei Mianroodi J, Fritzen F, Reese S. Application of artificial neural networks for the prediction of interface mechanics: a study on grain boundary constitutive behavior. Adv Model Simul Eng Sci 2020;7:1. https://doi.org/10.1186/s40323-019-0138-7.

[48] Ghavamian F, Simone A. Accelerating multiscale finite element simulations of history-dependent materials using a recurrent neural network. Comput Methods Appl Mech Eng 2019;357:112594. https://doi.org/10.1016/j.cma.2019.112594.
[49] Le BA, Yvonnet J, He Q -C. Computational homogenization of nonlinear elastic materials using neural networks. Int J Numer Methods Eng 2015;104:1061–84. https://doi.org/10.1002/nme.4953.
[50] Hambli R, Katerchi H, Benhamou C-L. Multiscale methodology for bone remodelling simulation using coupled finite element and neural network computation. Biomech Model Mechanobiol 2011;10:133–45. https://doi.org/10.1007/s10237-010-0222-x.
[51] Haghighat E, Juanes R. SciANN: A Keras/TensorFlow wrapper for scientific computations and physics-informed deep learning using artificial neural networks. Comput Methods Appl Mech Eng 2021;373:113552.
[52] Ott J, Pritchard M, Best N, Linstead E, Curcic M, Baldi P. A Fortran-Keras Deep Learning Bridge for Scientific Computing. Sci Program 2020;2020:8888811. https://doi.org/10.1155/2020/8888811.

Mesoscale analysis of fracture process in brick masonry structures

K. Koocheki, S. Pietruszczak*
McMaster University, Hamilton, ON, Canada

Abstract

This paper deals with mesoscale analysis of masonry structures, which involves fracture propagation in brick units as well as along the masonry joints. The brick-mortar interfaces are incorporated in standard finite elements by employing a constitutive law with embedded discontinuity. Macrocracks in bricks are modeled in a discrete way using the same methodology, without any a priori assumptions regarding their orientation. The proposed approach is computationally efficient as it does not explicitly require the discretization of joints. The accuracy of the approximation is first assessed by comparing the solution with a detailed mesoscale model incorporating interface elements. Later, a comprehensive numerical study is provided involving simulation of various experimental tests conducted on small masonry assemblages, as well as full-scale masonry walls. The results clearly demonstrate the predictive abilities of the proposed simplified approach.

Keywords: brick masonry; mesoscale modelling; embedded discontinuity

1. Introduction

Masonry systems are amongst the oldest types of engineering structures that include historical heritage and strategic buildings. The masonry assemblies have a significant compressive strength, however their shear and tensile resistance is limited, which is of particular concern in case of structures that are subjected to lateral loads induced by seismic events [1, 2]. Numerical investigations into the mechanical behaviour of existing masonry structures enable the detection of vulnerabilities and assist in the design of retrofitting techniques [3]. Computational models are generally developed either at meso or macroscale. The former approach considers the geometric arrangement of masonry units and mortar joints, and often incorporates the brick-mortar interfaces (cf. [4–7]). On the other hand, in macroscale approach the masonry is perceived as an equivalent homogenous and anisotropic continuum [8–11]. Homogenization procedures [12–14] or multiscale approaches [15–18] are typically considered as a bridging between the two scales. In general, despite the existing body of scientific research, the development of reliable and efficient

*Corresponding author: pietrusz@mcmaster.ca

strategies for modelling mechanical behaviour of structural masonry still remains a challenge [19–21].

The *macroscale* modeling of nonlinear behavior of masonry assemblies usually involves continuum approaches, such as as plasticity, damage mechanics, non-local damage plasticity [22–27]. In this case, the relevant data comes from experimental investigations. The latter have been conducted in the past not only on brick masonry but also on concrete and stone panels (cf. [28–30]). However, the tests at this scale are expensive and require a broad range of loading and boundary conditions. More importantly, in case of existing historical and strategic masonry buildings, acquiring specimens that are representative in terms of assessment of macroscopic behaviour is virtually impossible. On the other hand, the *mesoscale* models incorporate only the mechanical properties of individual constituents. This information can be acquired in-situ without affecting the integrity of existing structures, as it entails standard material tests. The main challenge in mesoscale models of masonry is incorporation of strain-softening response describing localized deformation associated either with sliding/separation along the brick-mortar interface or cracking of bricks/mortar. In general, the nonlinearity in mechanical behaviour of masonry is triggered by displacement discontinuities that develop at the interface between bricks and mortar [31] in either tensile or shear failure modes, i.e. Mode I and Mode II of crack propagation [32]. The latter has motivated the development of simplified mesoscale models that usually consider bricks as an elastic continuum [33], while accounting for the interface behaviour through plasticity [34–37] or combined damage-plasticity models [6, 38–40].

The current paper addresses the issue of modelling of damage propagation in structural masonry. The analysis employs a mesoscale approach in which the brick-mortar interfaces are considered as being embedded in the adjacent intact material and their mechanical properties are accounted for through a constitutive law with embedded discontinuity [41, 42]. The main objective here is the verification of the accuracy of this simplified approach against other methodologies, and its comprehensive validation against the existing experimental data. For this purpose, a series of numerical simulations are carried out involving various structural components of masonry, such as couplets/triplets, beams as well as masonry walls, subjected to different loading histories. The fracture patterns involving both the sliding/separation along brick-mortar interface as well as formation of discrete macrocraks in the brick units are investigated.

2. Mathematical formulation

A detailed mesoscale analysis of masonry requires discretization of the mortar region to account for development of cracks within this domain, as well as modelling of the brick-mortar interfaces, cf. Fig. 1. The simulations typically employ a graded unstructured mesh together with a set of interface elements. This impairs the computational efficiency, especially for larger structures, and may lead to numerical instabilities.

A simpler and pragmatic approach, which is advocated here, involves accounting for the presence of brick-mortar interfaces, which represent the weakest link in structural masonry, through a constitutive law with embedded discontinuity (CLED). Fig. 1a shows an example of FE mesh with a schematic representation of the discontinuities embedded in elements representing the joints. It is noted that the orientation of interfaces is known a-priori and their mechanical response is defined in terms of a rate form of a traction – displacement discontinuity relation (cf. [43]). Thus, in this case, for elements containing interfaces the discretization is the same as in the adjacent bricks, however the constitutive relation assigned is that based on the CLED formulation. For elements at the intersection of bed and head joints, the orientation of prevailing discontinuity will depend on the mode of failure. In this case, the components of traction along those two directions are used to check the failure criterion and the dominant mode is chosen. The orientation of the cracks in brick units can be assessed by specifying the orientation which maximizes the failure function or by employing the bifurcation criterion (cf. [44]). Their discrete propagation is then monitored via a level-set method.

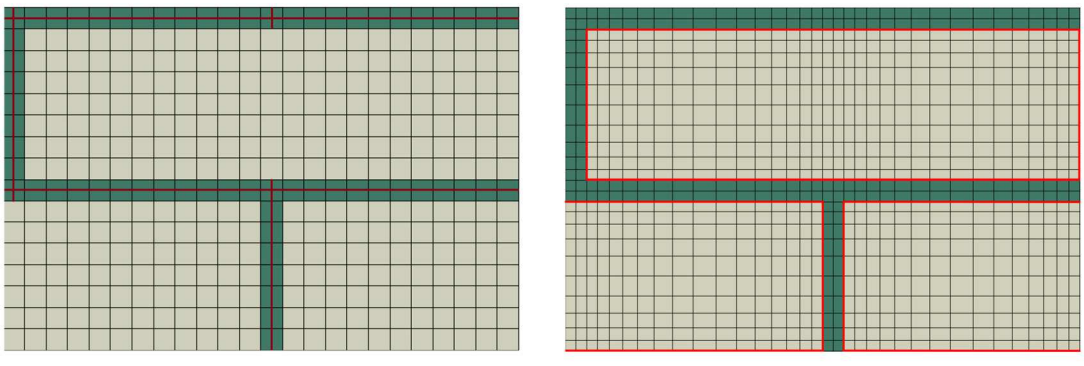

Fig. 1 Mesoscale finite element model of masonry: (a) elements with embedded brick-mortar interfaces (present approach); (b) discretized brick and mortar units bonded via interface elements (detailed approach)

In the present approach, the averaged mechanical properties of a referential volume containing a discontinuity are defined by a constitutive relation (cf. [41])

$$\dot{\sigma}_{ij} = \overline{\mathcal{D}}_{ijkl}\dot{\varepsilon}_{kl} \tag{1}$$

where

$$\overline{\mathcal{D}}_{ijkl} = \mathcal{D}_{ijkl} - \chi\mathcal{D}_{ijpq}\, C_{qr} n_p n_s \mathcal{D}_{rskl}; \qquad C_{ij} = \left(K_{ij} + \chi\mathcal{D}_{ijkl} n_k n_l\right)^{-1} \tag{2}$$

Here, $\mathcal{D}_{ijkl}$ is the fourth-order stiffness tensor which defines the properties of the intact material, n_i is the unit normal to the discontinuity surface, K_{ij} is the interfacial stiffness operator, and $\chi = \mathrm{A}/\mathrm{V}$ is an internal length scale parameter for a finite element of volume V intercepted by a discontinuity with a surface area A.

In the present study, the brick material is assumed as elastic-brittle and the onset of failure is determined by Mohr-Coulomb criterion with Rankine tension cut-off (cf. [43]). Thus, in this case, $\mathcal{D}_{ijkl} = \mathcal{D}^{e}_{ijkl}$ prior to the onset of localization. The interfaces are also considered as elastic prior to the onset of irreversible deformation, and the transition is governed by a similar form of failure criterion, i.e. Coulomb with tension cut-off

$$F = \begin{cases} \tau + \mu(\sigma - C), & \sigma < f_t \\ \sigma - f_t\,, & \sigma \geq f_t \end{cases} \tag{3}$$

Here, f_t is the tensile strength, C and μ are the shear strength parameters, while τ and σ are the components of the shear and normal traction acting at the brick-mortar interface. Upon the crack activation in tension, the strength of the material is assumed to undergo exponential decay as a function of irreversible part of crack opening ($\tilde{g}_N$) and Mode I fracture energy release rate (G_f^I), i.e.

$$f_t = f_t^o \exp\left(-\frac{f_t^o}{G_f^I}\tilde{g}_N\right) \tag{4}$$

where f_t^o is the tensile strength prior to the onset of failure. By analogy to representation (4), the degradation of the strength parameter in shear failure mode is assumed to take the form

$$\mu = \mu_r + (\mu_o - \mu_r)\exp\left(-\frac{c}{G_f^{II}}\tilde{g}_T\right) \tag{5}$$

where $c = C\ \mu_o$ is the cohesion, μ_o and μ_r are initial and residual internal friction coefficients, G_f^{II} is the fracture energy release rate in shear, and $\tilde{g}_T$ is the irreversible part of tangential component of displacement jump. Note that both the separation and sliding modes are associated with irreversible parts of the respective components of displacement discontinuity.

(i) Numerical integration scheme

Given the state of stress at pseudo-time step *n*, i.e. $\sigma_{ij}^{(n)}$, and invoking the additivity postulate, the constitutive relation (1) may be expressed in an equivalent form

$$\sigma_{ij}^{(n+1)} = \sigma_{ij}^{(n)} + \mathcal{D}_{ijkl}(\Delta\varepsilon_{kl} - \Delta\tilde{\varepsilon}_{kl}) \tag{6}$$

Here, $\Delta\tilde{\varepsilon}_{ij} = \frac{1}{2}\chi(n_i\Delta g_j + n_j\Delta g_i)$, where Δg_i is the displacement jump across the discontinuity. Apparently, if the intact material, within the referential volume, is elastic prior to localization then $\mathcal{D}_{ijkl} = \mathcal{D}^e_{ijkl}$.

The incremental form of the constitutive relation for the interfacial zone may be written as

$$t_i^{(n+1)} = t_i^{(n)} + K_{ij}^e\left(\Delta g_j - \Delta\tilde{g}_j\right) \tag{7}$$

where $\Delta\tilde{g}_i = \Delta\lambda\frac{\partial\psi}{\partial t_i}$ and $\psi = f(t_i)$ is the plastic potential function that defines the non-associated flow rule. Invoking the consistency condition and solving for the unknown interfacial stiffness operator results in

$$\Delta F = \frac{\partial F}{\partial t_i}\Delta t_i + \frac{\partial F}{\partial\tilde{g}_i}\Delta\tilde{g}_i = 0 \Rightarrow K_{ij} = K_{ij}^e - \frac{K_{ik}^e\frac{\partial\psi}{\partial t_k}K_{jl}^e\frac{\partial F}{\partial t_l}}{K_{ij}^e\frac{\partial\psi}{\partial t_i}\frac{\partial F}{\partial t_j} - \frac{\partial F}{\partial\gamma}} \tag{8}$$

where γ is the strain softening parameter, which for the tensile and shear failure mode is identified with $\tilde{g}_N$=$\tilde{g}_i n_i$ and $\tilde{g}_T = |\tilde{g}_i - \tilde{g}_i n_i|$, respectively. The return-mapping algorithm for an active loading process associated with crack opening/sliding can be written in terms of the residuals of traction and strain as

$$R_i^{(k)} \equiv \sigma_{ij}^{(n+1,k)}n_j - t_i^{(n+1,k)} \tag{9a}$$

$$S_{ij}^{(k)} \equiv \tilde{\varepsilon}_{ij}^{(n)} - \tilde{\varepsilon}_{ij}^{(n+1,k)} + \frac{1}{2}\chi\left(n_i\Delta g_j^{(n+1,k)} + n_j\Delta g_i^{(n+1,k)}\right) \tag{9b}$$

which can be linearized to the form

$$R_i^{(k)} + \frac{\partial R_i^{(k)}}{\partial \sigma_{ij}} \delta\sigma_{ij}^{(n+1,k)} + \frac{\partial R_i^{(k)}}{\partial g_j} \delta g_j^{(n+1,k)} = 0 \tag{10a}$$

$$S_{ij}^{(k)} + \frac{\partial S_{ij}^{(k)}}{\partial \sigma_{kl}} \delta\sigma_{kl}^{(n+1,k)} + \frac{\partial S_{ij}^{(k)}}{\partial g_j} \delta g_j^{(n+1,k)} = 0 \tag{10b}$$

Substituting the derivatives of the residuals leads to

$$R_i^{(k)} + \delta\sigma_{ij}^{(n+1,k)} n_j - K_{ij} \delta g_j^{(n+1,k)} = 0 \tag{11a}$$

$$S_{ij}^{(k)} + \mathcal{C}_{ijlm} \delta\sigma_{lm}^{(n+1,k)} + \frac{1}{2}\chi\left(n_i \delta g_j^{(n+1,k)} + n_j \delta g_i^{(n+1,k)}\right) = 0 \tag{11b}$$

where $\mathcal{C}_{ijkl}$ is the fourth-order compliance tensor. Solving Eq. (11) and neglecting the second-order derivatives, the incremental corrections to stress and displacement discontinuity can be obtained as

$$\sigma_{ij}^{(n+1,k+1)} = \sigma_{ij}^{(n+1,k)} + \delta\sigma_{ij}^{(n+1,k)} \tag{12a}$$

$$g_i^{(n+1,k+1)} = g_i^{(n+1,k)} + \delta g_i^{(n+1,k)} \tag{12b}$$

where

$$\delta\sigma_{ij}^{(n+1,k)} = -\mathcal{D}_{ijlm}\left(S_{lm}^{(k)} + \frac{1}{2}\chi\left(n_l \delta g_m^{(n+1,k)} + n_m \delta g_i^{(n+1,k)}\right)\right) \tag{13a}$$

$$\delta g_i^{(n+1,k)} = \left(K_{ij} + \chi \mathcal{D}_{ijpq}^{e} n_p n_q\right)^{-1} (R_j^{(k)} - \mathcal{D}_{jlrs}^{(k)} S_{rs}^{(k)} n_l) \tag{13b}$$

which completes the numerical implementation of this approach.

3. Assessment of the level of approximation of simplified approach

In order to assess the accuracy of the simplified mesoscale approach its performance was first verified against the solution based on a detailed model that incorporates interface elements. The examples presented here involve simulation of tension and biaxial compression-tension tests on half-scale masonry panels, similar to those used in experimental investigations reported in ref. [45]. The masonry arrangement consists of nine rows of bricks placed in a running-bond pattern to form a panel 360×360×50 mm in size. The bricks have dimensions of 115×35×50 mm with a mortar thickness of 5 mm.

In the simplified approach, the brick-mortar joints were considered as being embedded in the adjacent intact material and were modeled using the CLED approach, viz. Eqs.(1-2). The solution was then compared to a detailed model that incorporated all constituents, i.e. bricks, mortar, as well as the brick-mortar interfaces. In this case, the interfaces were modelled using the surface-based cohesive contact algorithm [46]. The latter is primarily intended for describing the debonding process but can also incorporate the frictional behaviour. Here, the traction-separation/sliding laws were adopted in the form that is analogous to that in Eqs. (4-5). This allows a direct comparison of both methodologies.

The simulations were carried out for uniaxial tension parallel to the bed joints and biaxial compression-tension with a fixed ratio of compressive to tensile load of 2. In the former case, the analysis was displacement-controlled, while in the latter case a load-controlled scheme was employed. The geometry and the boundary conditions are shown in Fig. 2. For biaxial test, the load was applied to the top and right boundaries of the panel, while the opposing surfaces were fixed in the direction of the imposed load. Figs. 2a and 2b show the FE mesh for both the proposed embedded interface approach and the detailed model including the mortar and the cohesive interfaces. It is noted that in the simplified approach, there are no specific restrictions on the element size. Thus, in this case a coarser structured mesh can be employed, and the interfaces are embedded in elements which are at the location of mortar joints. The approach incorporates the internal length scale parameter, so that there is no systemic sensitivity to the mesh size/alignment. The material properties used in numerical analysis are summarized in Table 1. Note that for simulating biaxial compression-tension the tensile strength of bricks was reduced to 0.5 MPa so that to allow the failure mode which includes the onset and propagation of cracks in the brick units.

Table 1. Material parameters for masonry panel simulations

	Brick	Mortar	Interface
Young's modulus, E (MPa)	20000	15000	N/A
Poisson's ratio, υ	0.2	0.1	N/A
Tensile strength, f_t (MPa)	3.5	0.6	0.5
Internal friction coefficient, μ	0.8	0.7	0.6
Cohesion, c (MPa)	4.0	0.8	0.8
Normal stiffness, K_N (MPa/mm)	N/A	N/A	100
Shear stiffness, K_T (MPa/mm)	N/A	N/A	50
Tensile fracture energy release rate, G_f^{I} (N/m)	100	15	15
Shear fracture energy release rate, G_f^{II} (N/m)	500	80	80

The results for uniaxial tension along the bed joints are presented in Figs. 2c-2f. Fig. 2f shows the global characteristics in terms of average stress (i.e. magnitude of resultant reaction force over the area) and average strain. It is evident that the ultimate strength of the panel as predicted by the embedded interface approach is nearly the same as that obtained in the detailed model. It is noted that in the former case, two sets of simulations were carried out in which the joints were assumed to be embedded either in the brick material or in the mortar. In both settings, the CLED approximation was used, viz. Eqs. (1-2). As expected, the elastic properties of the intact material (i.e. brick vs mortar) had only a marginal effect on the global stiffness, while the ultimate load remained the same. For all cases considered, the failure mode involved a zig-zag pattern, in which the head joint experienced the tensile debonding, while the bed joint underwent a shear induced failure. Fig. 2c shows the initial fracture pattern obtained in a detailed model, superimposed on the scaled displacement field. A similar picture showing the displacement field at the ultimate load is provided in Fig. 2d. Note that the deformation scales in both these figures and not equal. The crack pattern obtained from embedded interface approach, which was similar to that of the detailed model, is provided in Fig. 2e.

As mentioned earlier, the simulations for biaxial tension-compression (BTC) were carried under load- controlled conditions. In this case, the ultimate strength of the panels was determined by examining the evolution of a stability parameter (SP) defined as the ratio of the second rate of internal work normalized with respect to the elastic solution

$$\mathrm{SP} = \frac{\int \dot{\sigma}_{ij}\dot{\varepsilon}_{ij}dV}{\int \dot{\sigma}^{e}_{ij}\dot{\varepsilon}_{ij}dV} \tag{14}$$

In general, the stability parameter remains within the range $1 \geq \mathrm{SP} \geq 0$, and $\mathrm{SP} = 0$ implies the singularity in the global stiffness operator, i.e. the loss of stability.

The results of the numerical analysis are shown in Fig 3. In this case, the global fracture pattern involves the tensile failure in head joints combined with the onset and propagation of cracks through the brick units. The latter have been traced in a discrete way using the level-set method (cf. [43]). Since the ratio of compressive to tensile load is fixed here at a constant value of 2, only the load-displacement characteristics in tension are shown (Fig. 3d). The general conclusions are similar to those that stem from the previous example. It is evident that the ultimate load at failure

is similar in both the simplified and detailed models. Its assessment is not visibly affected by the elastic properties of intact material in which the joints are said to be embedded. The crack pattern, as shown in Figs, 3a-b and 3c, is also in a fairly good agreement for both approaches used.

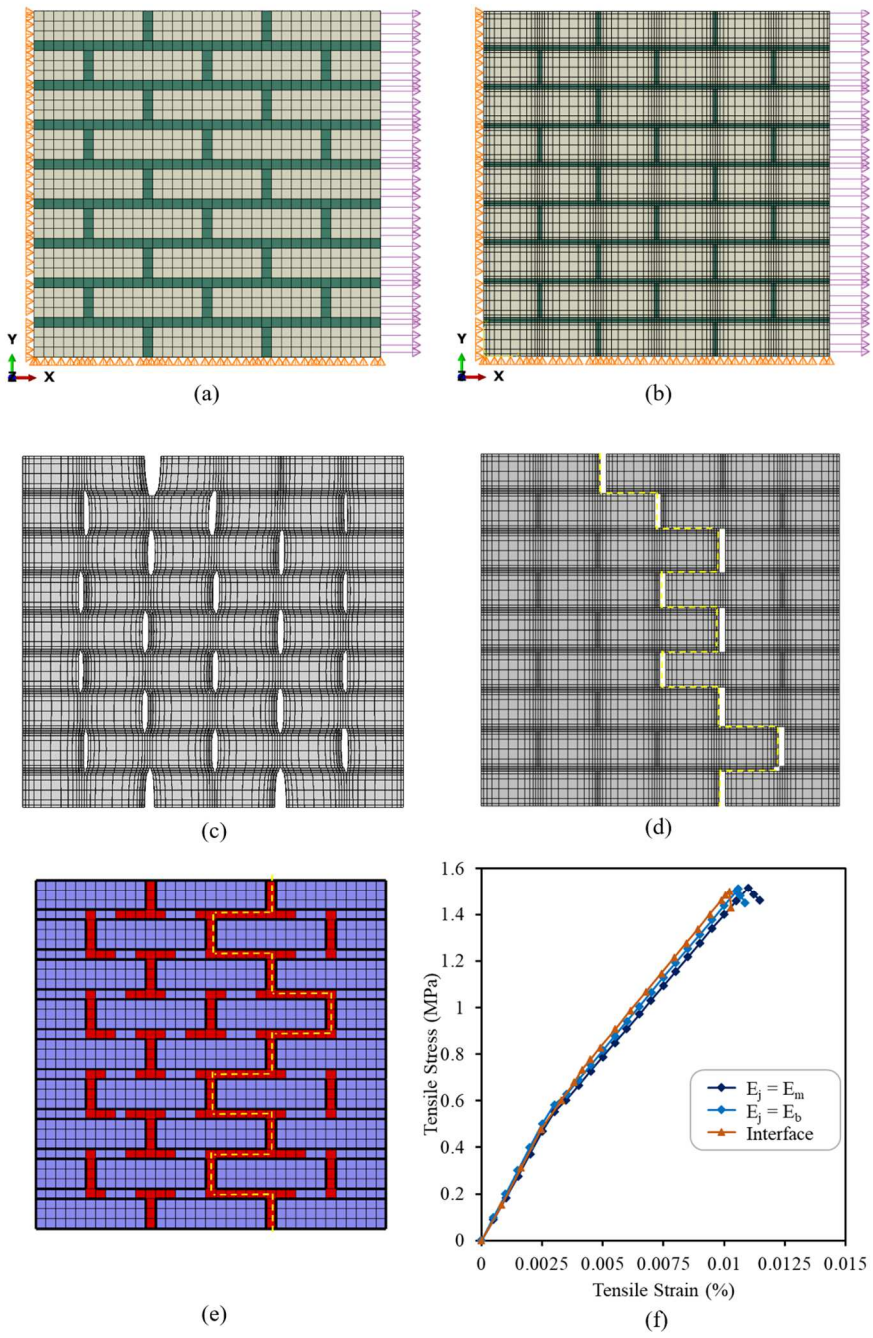

Fig. 2 Finite element mesh and boudnary conditions for (a) embedded interface approach and (b) detailed model with interfaces; (c) initial and (d) final crack pattern for detailed model, superimposed on displacement field [note that the deformation scales are not equal]; (e) crack pattern at the ultimate load for embedded interface approach; (f) average stress-strain response of the panel

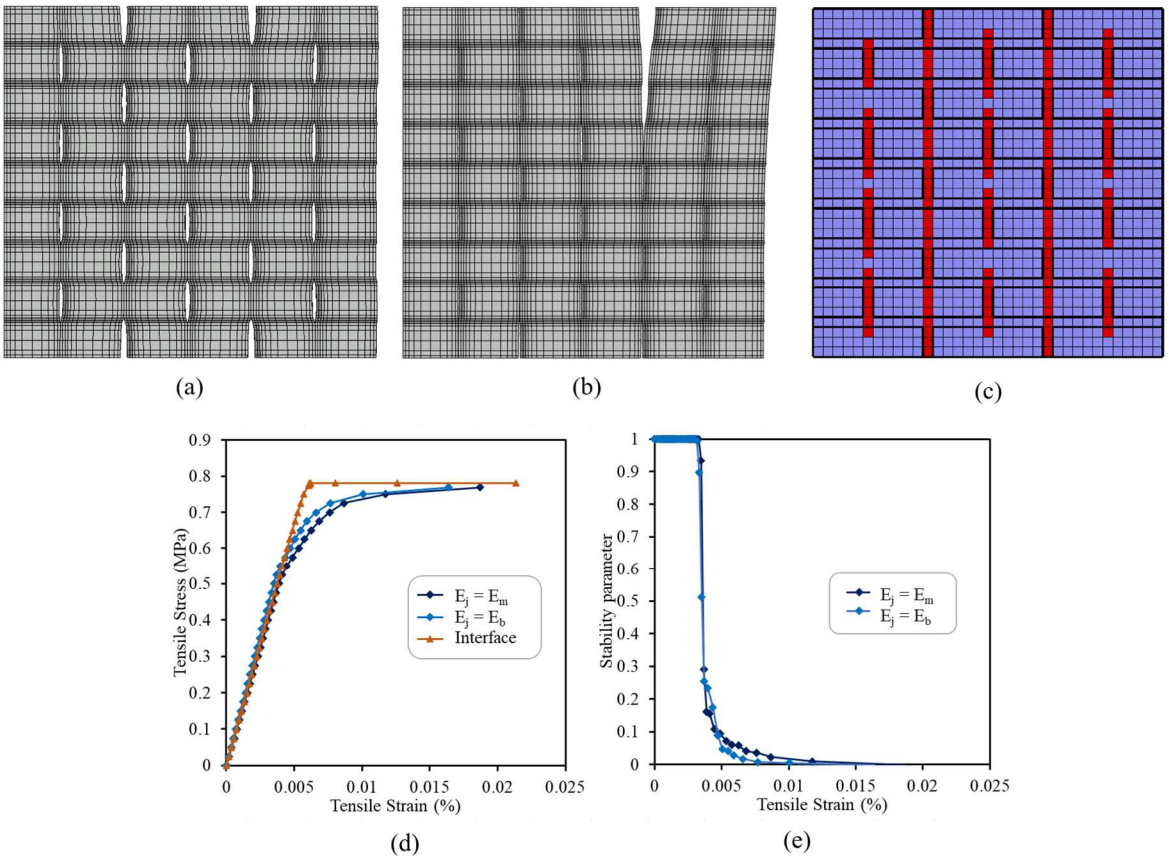

Fig. 3 (a) initial and (b) final crack pattern in detailed model with interfaces [note that the deformation scales are not equal]; (c) crack pattern at the ultimate load for embedded interface approach; (d) average tensile stress-strain response of the panel; (e) evolution of stability parameter (SP), Eq. (14)

4. Numerical analysis involving small-scale experimental set-ups

In this section a series of numerical examples is provided involving simulation of shear tests on masonry triplets/couplets. The tests incorporate different loading conditions, including cyclic loading, and the prevailing failure mode involves the propagation of damage along the brick-mortar bonds. The latter is modeled using the proposed embedded interface approach.

4.1. Simulation of shear tests on masonry triplets

The tests simulated here were part of a comprehensive study on the mechanical characteristics of masonry conducted in ref. [47]. The tests employed a set up consisting of three bricks with dimensions of 170×120×55 mm that were arranged vertically and separated by two rows of 10 mm

thick mortar joints. The masonry triplets were loaded in vertical direction to reach normal compressive stress of 0.12 MPa, 0.4 MPa, 0.8 MPa, and 1.25 MPa, respectively, and subsequently sheared to induce shear failure in bed joints. The geometry of the finite element model and the respective boundary conditions are shown in Fig. 4a. The mesh consisted of a total of 726 eight-noded cubic elements. The bottom brick was fixed in both horizontal and vertical directions and the normal stress was applied at the top of the assembly. After reaching the prescribed value of the normal stress, the top brick was also fixed in place while lateral displacement was applied incrementally to the middle brick. The simulations were carried out using material parameters consistent with those reported in ref. [47]. In particular, the values of elastic constants for the brick material were taken as E = 2500 MPa and υ = 0.2. The components of the interfacial elastic stiffness moduli were assumed as $K_N = K_T$ = 250 MPa/mm, while the shear strength parameters were c_o = 0.35 MPa and μ_o = 0.8, with $\mu_r = 0.7\mu_o$ as the residual friction coefficient. Since the experimental observations suggest that Mode II fracture energy release rate is dependent on the normal compressive stress [48], this parameter was adjusted by trial and error within the range of 50-200 N/m.

In order to compare the numerical results to those of experiments, average shear stress and lateral strain were calculated based on the dimensions of the specimen. Fig. 4b shows the deformed mesh including the elements with embedded interface representing the two rows of bed joints in the assembly. The predicted mechanical characteristics, corresponding to different values of normal compressive stress, are shown in Fig. 4c. Here, the results of the simulations are compared with the upper and lower limits of the experimental data obtained for different pre-compression stress values. It is evident that the predictions, in terms of the ultimate shear stress at different compressive loads, as well as the post-peak degradation of strength, are fairly consistent with the experimental evidence.

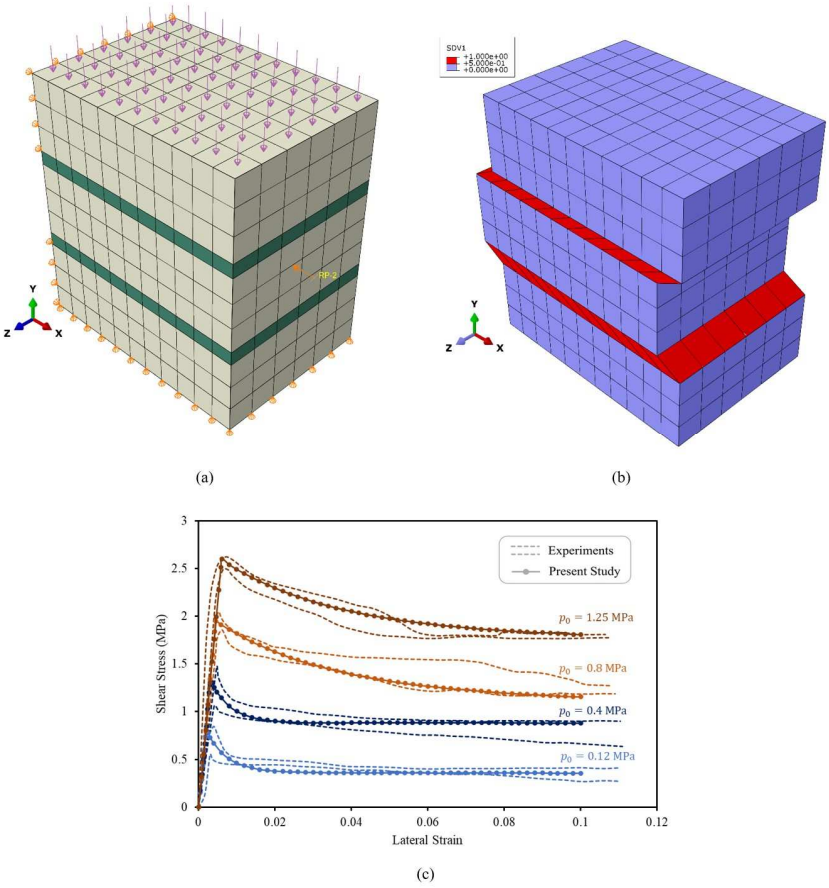

Fig. 4 (a) Finite element mesh for masonry triplet under compressions and shear; (b) deformed mesh showing the cracked elements with embedded interface; (c) load-displacement response compared with experimental data

4.2. Simulation of shear test on a masonry couplet involving unloading-reloading cycles

The next set of simulations was focused on finite element analysis of experiments conducted in ref. [49]. The tests involved brick couplets subjected to shear displacement unloading-reloading cycles under a prescribed normal stress. The specimens included two bricks with dimensions of 230×51×110 mm separated by a layer of mortar with a thickness of 10 mm. The FE model consisted of 825 eight-noded cubic elements, as shown in Fig. 5a. To simulate the actual loading conditions, the bottom surface of the specimen was fixed in vertical direction and a vertical load was applied at the top to generate a normal compressive stress of 0.51 MPa. In the next step, the bottom surface of the specimen was fixed in lateral direction as well, and the shear displacement was applied at the top of the assembly. During the loading process, the shear displacement was

reversed multiple times to induce unloading-reloading cycles until the maximum lateral displacement of 1.95 mm was reached.

The material parameters were again selected based on experimental data provided in ref. [49]. The elastic constants for the brick material were E = 14500 MPa and υ = 0.06, while the normal and tangential components of the interfacial elastic stiffness were 50.0 MPa/mm and 5.0 MPa/mm, respectively. Furthermore, the interfacial shear strength parameters were c_o = 0.3 MPa and μ_o = 0.7, while the tensile strength of the joints was f_t = 0.1 MPa. Mode II fracture energy release rate was chosen as G_f^{II} = 70 N/m.

The predicted shear stress versus lateral displacement characteristic is provided in Fig, 5b and the results are compared with the experimental data. The figure also shows the deformed finite element mesh. It is evident that both the ultimate and residual shear strengths are in a good agreement with the recorded experimental values. Also, the predicted post-peak deformation, for both an active process as well as the unloading-reloading cycles, is fairly consistent with the experimentally observed response.

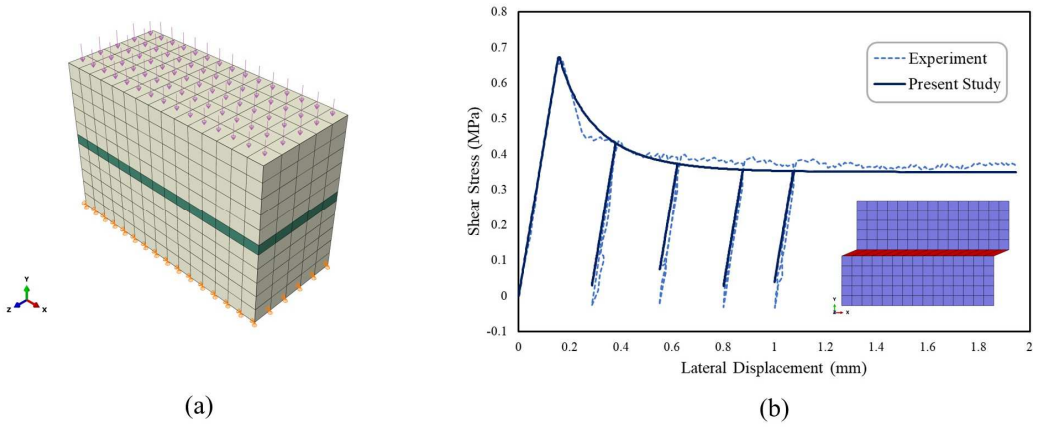

(a) (b)

Fig. 5 (a) Finite element model for brick couplets; (b) load-displacement response compared with the experimental results

4.3. Cyclic shear test on a masonry couplet

The laboratory experiments simulated here involved cyclic direct shear tests on two rows of bricks arranged in a running-bond pattern [50]. Two types of bricks, referred to as ‘old’ and ‘new’, were used with dimensions of 208×100×64 mm and 193×92×55 mm, respectively. Thickness of

mortar joints used for these two types of bricks was 13 mm and 7 mm. The pre-compression stress for the 'old' and 'new' brick specimens were 0.33 MPa and 1.34 MPa, respectively.

The geometry and the boundary conditions are shown in Fig. 6a. The finite element model employed a total of 1925 elements. The bottom boundary was fixed and the compressive load was applied at the top of the assembly. This was followed by application of lateral displacement applied in one and a half cycles. The material parameters used for these simulations are summarized in Table 2.

The results of the analysis are shown in Fig. 6b. The predicted initial ultimate strength as well as the strain-softening branch are very close to those recorded in the experiments. Once the residual shear strength is reached, the load-displacement curve follows the same path in both directions of the shear load. Overall, the basic trends, including the dependence of peak and residual shear strength on the value of the compressive stress, are consistent.

Table 2. Material parameters for cyclic shear test simulations

	Brick ('new')	Brick ('old')	Embedded interface
Young's modulus, E (MPa)	14700	8800	N/A
Poisson's ratio, υ	0.22	0.16	N/A
Tensile strength, f_t (MPa)	3.0	3.0	0.7
Internal friction coefficient, μ	0.8	0.8	0.65
Cohesion, c (MPa)	2.5	2.5	1.2
Normal stiffness, K_N (MPa/mm)	N/A	N/A	80
Shear stiffness, K_T (MPa/mm)	N/A	N/A	40
Tensile fracture energy release rate, G_f^{I} (N/m)	100	100	50
Shear fracture energy release rate, G_f^{II} (N/m)	500	500	100

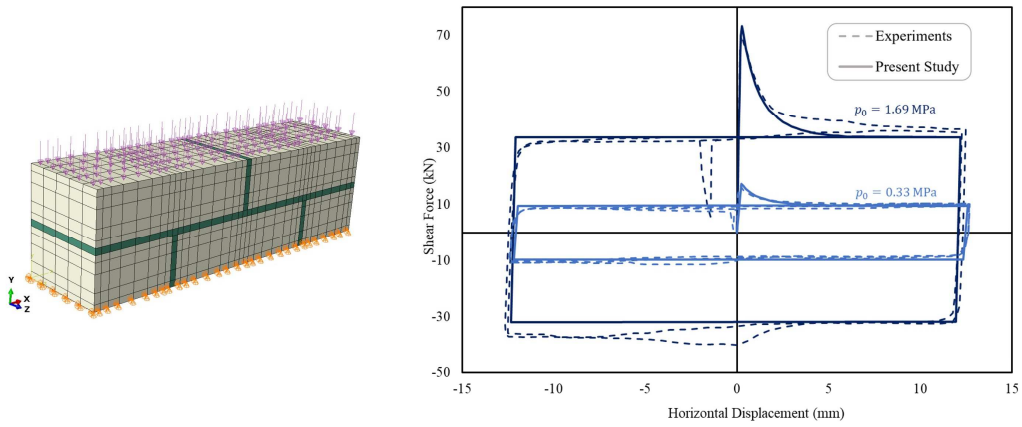

(a) (b)

Fig. 6 (a) Discretized model of the two-leaf masonry assembly; (b) load-displacement response for the cyclic shear loading compared with the experimental results for two different normal compressive loads

4.4. Simulation of a three-point bending test on a masonry beam

This section provides the numerical analysis of a three-point bending test on a masonry beam consisting of four rows of bricks arranged in a running-bond pattern. The simulations were carried out on the basis of the experimental results reported in ref. [49]. The masonry beam consisted of bricks measuring 230×76×110 mm in size with mortar joint thickness of 10 mm. The total length of the beam was 1430 mm and the depth was 334 mm.

The model was discretized into a total of 11,206 eight-noded cubic elements, as shown in Fig. 7a. One row of nodes in the middle part of the bottom left brick was fixed in the horizontal and vertical directions while the opposing row of nodes, on the right side of the beam, was fixed only in the vertical direction. The displacements were applied incrementally to the two rows of nodes at the top of the brick located in the middle of the beam. The direction of applied displacement was reversed twice during the simulation to model the cyclic loading component of the experiment. The material parameters were again selected based on the information provided in the original reference and their values are summarized in Table 3.

The main results of analysis are provided in Fig.7. Fig. 7b shows the deformed mesh and the cracked region at the end of the simulation. The latter is compared to the schematic (Fig. 7c) and the actual (Fig. 7d) crack pattern observed in the experiments. The crack mode includes tensile cracking of head joints in the bottom portion of the beam, as well as a combined tensile or

compressive shear cracking of bed joints and head joints. In order to obtain the crack propagation as observed in the experiment, an imperfection was introduced consisting of a minor reduction in the strength parameters of constituents in the right half of the beam. This was required since otherwise the cracks would propagate symmetrically through the beam, as the loading and boundary conditions are both symmetric.

It is evident that the load-displacement response, shown in Fig. 7e, has been predicted quite well. There is a slight reduction in the slope of the curve prior to reaching the ultimate load, which can be attributed to the development of the tensile crack in the head joint located at the bottom of the beam. The post-peak strain softening response starts to form later as the cracks develop further through the depth of the beam towards the top.

Table 3. Material parameters for three-point bending test simulation

	Brick	Embedded interface
Young's Modulus, E (MPa)	14500	N/A
Poisson's ratio, υ	0.06	N/A
Tensile Strength, f_t (MPa)	2.8	0.1
Internal friction coefficient, μ	0.8	0.7
Cohesion, c (MPa)	2.0	0.45
Normal stiffness, K_N (MPa/mm)	N/A	80
Shear stiffness, K_T (MPa/mm)	N/A	40
Tensile fracture energy release rate, G_f^{I} (N/m)	250	15
Shear fracture energy release rate, G_f^{II} (N/m)	900	80

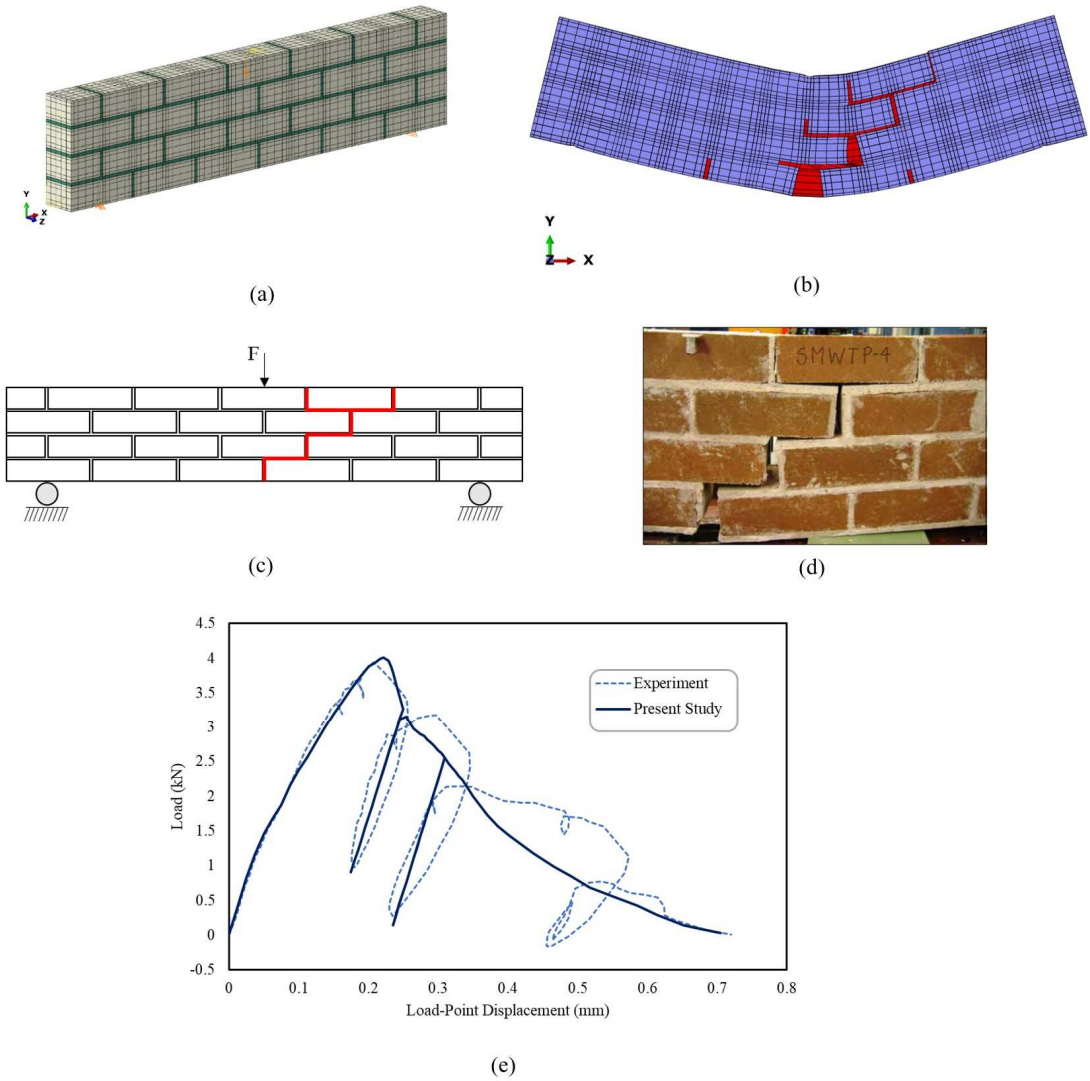

Fig. 7 (a) Finite element model of the three-point bending test on masonry beam; (b) deformed mesh showing the final crack pattern; (c) schematic illustration of the experimentally observed crack pattern; (d) picture of the damage pattern; (e) load-displacement curve compared with experimental data

5. Numerical analysis involving tests on masonry walls

5.1. Masonry wall under monotonic shear and compressive load

In this section the experimental tests on scaled masonry walls are simulated using the proposed simplified approach with interfaces embedded in the adjacent bricks. The first example deals with tests carried out in refs. [51, 52]. The experiments were conducted on walls made of bricks with

dimensions of 210×52×100 mm and mortar joints with 10 mm thickness. The bricks were arranged in a running-bond pattern in 18 rows, with top and bottom rows being confined in the loading platens. The length of the wall was 1000 mm and its height, excluding the top and bottom rows, was 990 mm.

The experiments were carried out on walls with and without an opening. In the first stage, a compressive load of intensity 0.4 MPa (for solid wall) and 0.3 MPa (wall with opening) was applied. After the normal load was in place, a lateral displacement was imposed through the top platen while the vertical displacement was prevented using the vertical loading jacks. Fig. 8a shows the experimental setup in which the loading frame and actuators induced the boundary conditions for the two steps mentioned earlier (cf. Fig. 8b-c). The roller support shown in Fig. 8c represents the active vertical loading through jacks 2-4 which prevented vertical movements of the top of the wall during the shear loading.

The FE simulations presented in this section were performed using two structured meshes with different size of elements in order to investigate the mesh sensitivity of the solution incorporating the proposed methodology. The model with a fine mesh consisted of 33,822 eight-noded cubic elements, while the coarser mesh incorporated 8,272 elements. Fig. 8d-e show both models, i.e. with fine and coarse discretization, for the wall with an opening. A similar mesh was used for the solid wall as well. In the analysis, the bottom edge of the walls was fixed, and the normal compressive load was applied to the top boundary. After reaching the desired intensity, the vertical displacement at the top of the wall was constrained while lateral displacement was applied. At this stage, the evolution of shear force was recorded. The simulations were carried out using the material parameters listed in Table 4, which again were selected based on the data provided in the original reference.

Fig. 9a shows the load-displacement response for the finite element model of the solid wall with two different mesh sizes. The results are compared with the experimental upper and lower bounds. The representative crack pattern of a solid wall in the experiment is reproduced in Fig. 9b and is compared with crack patterns obtained from finite element simulations shown in Fig. 9c-d for fine and coarse mesh, respectively. Fig. 10 shows the experimental and numerical results for the wall with an opening. Here again, the load-displacement curves and the fracture mode are compared. For the experimental part, the upper and lower bounds of the experimental results are included.

Table 4. Model parameters for simulating walls under shear

	Brick	Embedded interface
Young's Modulus, E (MPa)	16700	N/A
Poisson's ratio, υ	0.15	N/A
Tensile Strength, f_t (MPa)	2.0	0.25
Internal friction coefficient, μ	0.7	0.75
Cohesion, c (MPa)	3.5	1.4
Normal stiffness, K_N (MPa/mm)	N/A	100
Shear stiffness, K_T (MPa/mm)	N/A	50
Tensile fracture energy release rate, G_f^{I} (N/m)	80	18
Shear fracture energy release rate, G_f^{II} (N/m)	200	80

The numerical predictions seem to be in agreement with the experimental data in all key factors that include the ultimate bearing capacity and the crack pattern which develops in both the brick-mortar joints as well as the brick units. For the solid wall, the top right and bottom left sections show tensile horizontal cracks in bed joints. In the rest of the domain, the experimental data shows a zig-zag pattern of fracture involving cracking in the bricks as well as brick-mortar joints. This is particularly evident at the top left and bottom right as well as in the middle part of the wall. The numerical results display a similar trend.

For walls with an opening, the experimental results show more distinguishable zig-zag crack patterns in the top-left and bottom-right corners of the opening that propagate to the corners of the walls. Numerical simulations display a similar effect in terms of the overall orientation of the diagonal macrocracks. Cracking within the bricks takes place near the top-left and bottom-right corners of the walls which is consistent with the experimental observation.

As expected, the ultimate bearing capacity for the walls with opening is significantly smaller compared to the solid walls (cf. Figs. 9a and 10a). The same conclusion applies to the initial stiffness. The mesh size appears to have a negligible effect on the solution, which stems primarily from incorporation of the internal length scale parameter. The models with finer mesh give a slightly lower assessment of the ultimate load while the stiffness degradation that stems from propagation of localized damage is very similar.

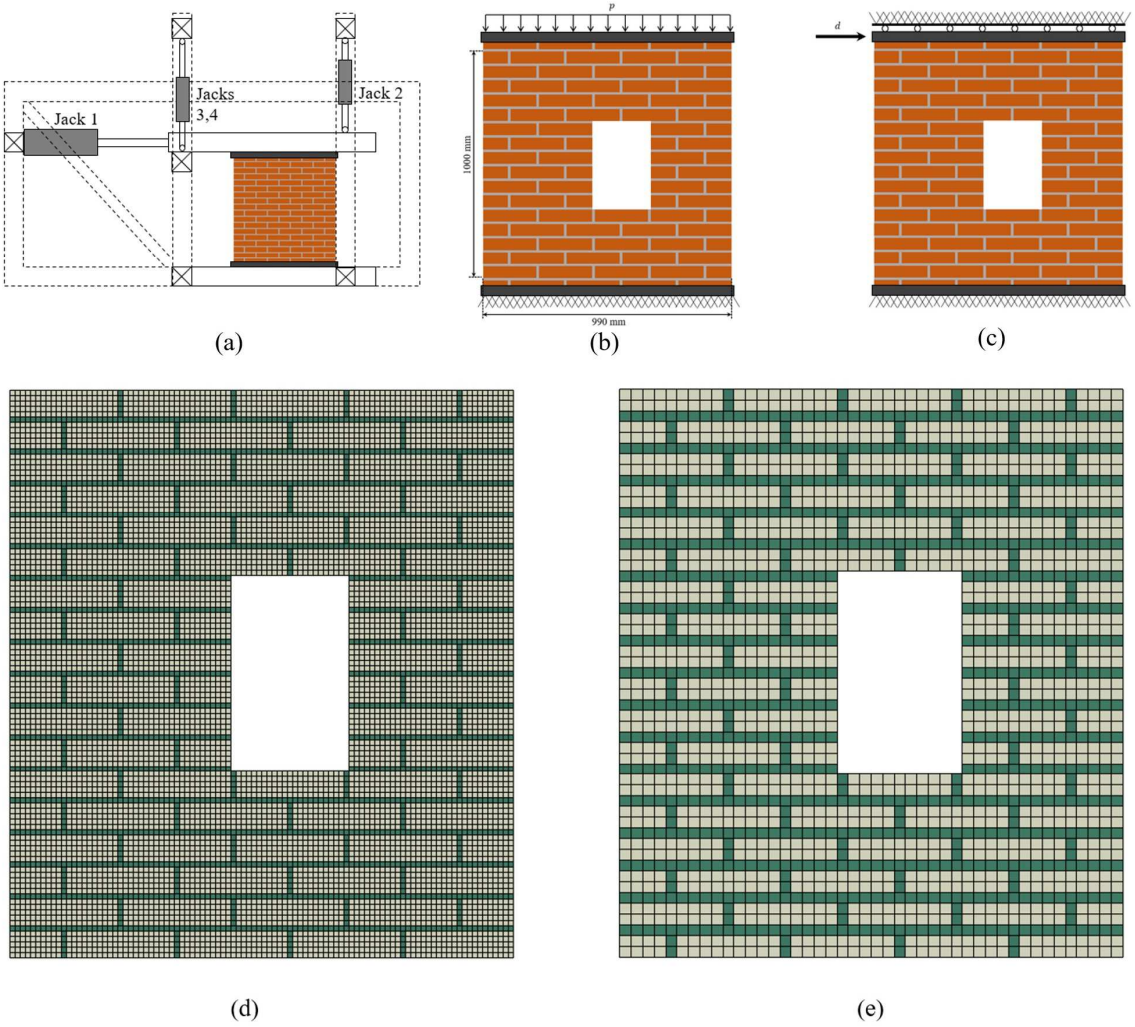

Fig. 8 (a) schematic diagram of the experimental set-up; (b-c) boundary conditions for the two loading steps; (d-e) fine and coarse mesh for the FE analysis

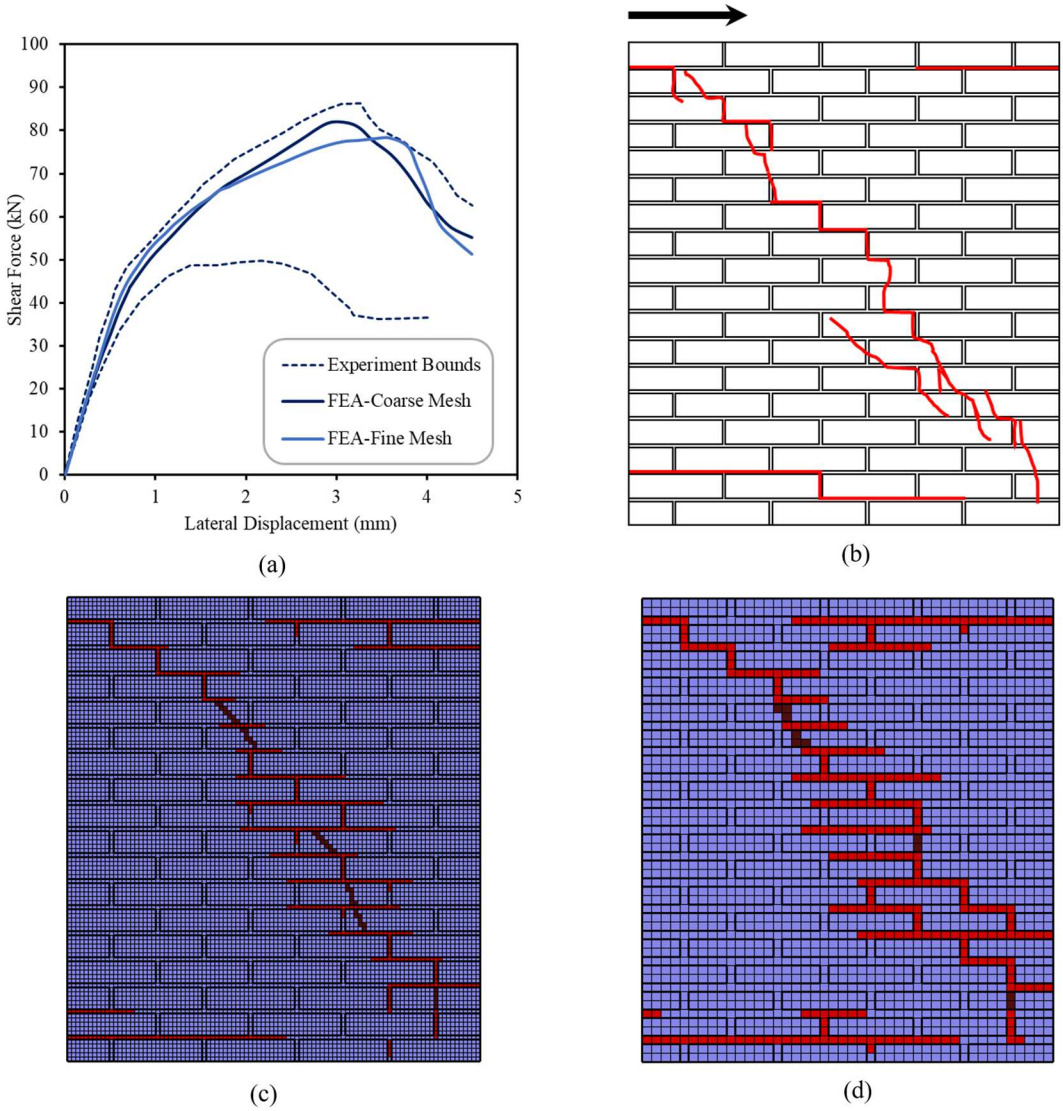

Fig. 9 (a) load-displacement curves compared with upper and lower bounds of the experiments; (b) schematics of fracture pattern as reported in experiments; (c-d) crack pattern obtained using fine and coarse mesh (cracks developed in bricks are shown in darker shade).

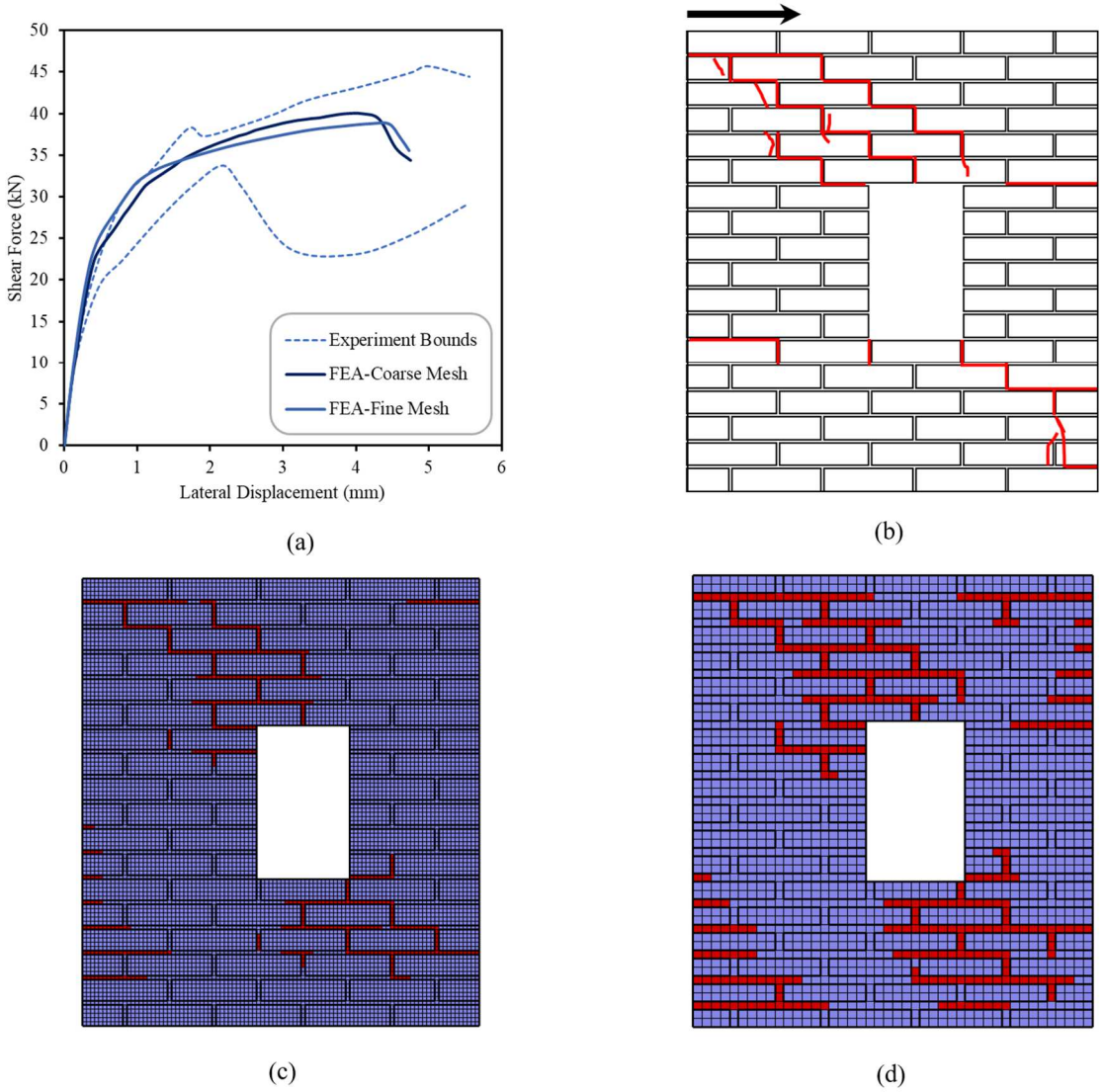

Fig. 10 (a) load-displacement curves compared with upper and lower bounds of the experiments; (b) schematics of fracture pattern as reported in experiments; (c-d) crack pattern obtained using fine and coarse mesh.

5.2. Full-scale masonry wall under shear and compressive load

The last example provided here deals with simulation of tests on unreinforced masonry walls conducted in ref. [53]. The experiments were carried out on 3.07×2.70×0.10m walls that were glued to the bottom of a loading frame. The specimens were loaded via a steel beam that was attached to the top of the wall. The loading process consisted of applying the own weight of the material and a vertical stress of intensity 0.12 MPa, followed by a shear stage that involved

application of lateral displacements. The walls had an opening with an embedded concrete lintel at the top of the free span extending approximately 100 mm on each side. The dimensions of bricks were 210× 50 ×100 mm with mortar thickness of 10 mm.

Fig. 11a shows the geometry and the finite element discretization of the wall. The mesh incorporated the total of 79,800 eight-noded cubic elements. The boundary nodes at the base of the model were fixed in horizontal and vertical directions. In order to simulate the boundary conditions associated with the presence of the top steel beam, the top boundary nodes were kinematically tied to a reference point [46] at which the monotonically increasing lateral displacement was applied. The material parameters, which are summarized in Table 5, were chosen in accordance with the information provided in ref. [53]. Since the experimental data did not show any crack development in the brick units, the bricks themselves were considered as elastic, with Young's modulus of 4600 MPa and Poisson's ratio of 0.14. Moreover, the elastic properties of the concrete lintel at the top of the opening were taken as E=30 GPa and υ=0.15.

Table 5. Material parameters used in the finite element simulation of monotonic shear loading of masonry wall

	Embedded bed joints	Embedded head joints
Tensile Strength, f_t (MPa)	0.09	0.05
Internal friction coefficient, μ	0.85	0.85
Cohesion, c (MPa)	0.14	0.14
Normal stiffness, K_N (MPa/mm)	70.0	50.0
Shear stiffness, K_T (MPa/mm)	35.0	25.0
Tensile fracture energy release rate, G_f^{I} (N/m)	8.0	5.0
Shear fracture energy release rate, G_f^{II} (N/m)	60.0	40.0

Fig. 11b shows the deformed finite element model together with the obtained crack pattern. Note that the finite element mesh is not shown here to improve the clarity of the results. The fracture mechanism appears to be in a good agreement with the experimental observation, the latter shown schematically in Fig. 11c. There are three major cracked domains that develop in the bottom left of the wall, as well as the top left and bottom right corners of the opening. The load-displacement curve for the shear stage is shown in Fig. 11d. Here, in addition to experimental data, the results of numerical simulations conducted in ref. [53], which were based on meso and macroscale models, are also included. It is evident that the simplified methodology proposed in

this work, in which the presence of joints is accounted for via the constitutive law with embedded discontinuity, i.e. Eqs.(1-2), is fairly accurate and requires less computational effort as the interfaces are explicitly embedded in the adjacent referential volume.

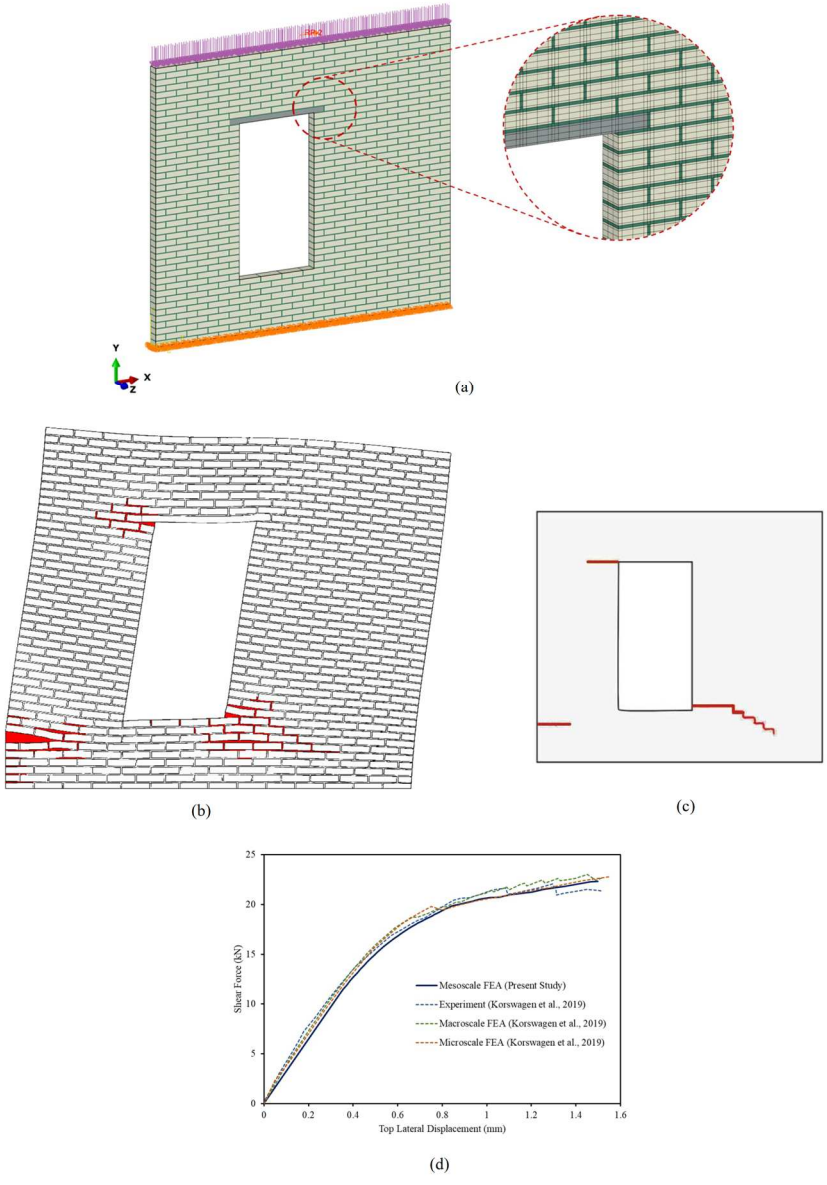

Fig. 11 (a) finite element model with an enlarged portion showing the details of the mesh; (b) crack pattern from the FE analysis; (c) schematic illustration of the crack pattern observed at the end of experiment on TUD-Comp 41 specimen; (d) load-displacement characteristics compared with the experimental data as well as numerical studies reported in ref. [53]

6. Concluding remarks

In this work, the application of the constitutive law with embedded discontinuity for modelling the mechanical response of masonry at mesoscale was extensively studied. Since the interfaces between the brick units and mortar joints generally act as planes of weakness, their presence was accounted for through a homogenization procedure incorporating the volume averaging. This approach is pragmatic and efficient in implementation and adequately captures the complex behaviour of masonry in boundary value problems. Its primary advantage lies in the fact that the same formulation can be used for capturing the fracture propagation in brick units as well. The difference between the crack initiation process in bricks compared to elements with embedded interface is that the crack orientation in bricks is not known a priori and needs to be identified by means of a suitable criterion.

The proposed approach is practical for analysis of existing small and medium-sized masonry structures since it requires a limited amount of information regarding the mechanical properties of the constituents. The required properties can be obtained from simple laboratory experiments (i.e., tensile and direct shear tests) on small samples acquired from parts of the existing structure.

The numerical implementation of the framework incorporated an implicit integration scheme to attain the stress equilibrium and to assess the embedded crack opening/sliding at the element level. The use of the implicit integration scheme ensures the stability of the analysis and the numerical convergence. The proposed methodology employing embedded interfaces was first verified against a detailed analysis incorporating the mortar joints and the brick-mortar interface elements. It was demonstrated that the level of approximation in the proposed simplified approach does not markedly impair the accuracy and, at the same time, enhances its computational efficiency.

The proposed formulation was validated through a comprehensive numerical study involving simulation of a series of monotonic and cyclic tests on masonry triplets and couplets under tensile and shear loading conditions. The results showed a good agreement with the experimental data published in literature. Later, a more complex examples involving masonry walls under compression and shear were considered and the results were again compared with those recorded in the experiments.

Various examples given in the present study showed that the most frequent mode of fracture involves failure along the brick-mortar interfaces, while for some problems the cracking took place also within the brick units. Cracks in bricks develop mainly in the tensile splitting mode, although in some cases they may also undergo a frictional failure. In general, in a typical masonry layout, the crack propagation process can transfer from bricks towards the brick-mortar interface but is less likely to follow the opposite path. The cracks also form at the junction between the bed and head joints. In this case, the assessment of the dominant crack direction can be assessed based on the values of the failure function along these two respective orientations.

Acknowledgement

The research presented here was supported by the Natural Sciences and Engineering Research Council of Canada through a Collaborative Research and Development Grant (CRD) in partnership with Hydro-Quebec.

Declaration of Conflicting Interests

The authors declare that there is no conflict of interest.

6. References

[1] Haach VG, Vasconcelos G, Lourenço PB. Parametrical study of masonry walls subjected to in-plane loading through numerical modeling. *Eng Struct* 2011; 33: 1377–1389.

[2] Benedetti D, Carydis P, Limongelli MP. Evaluation of the seismic response of masonry buildings based on energy functions. *Earthq Eng Struct Dyn* 2001; 30: 1061–1081.

[3] Malena M, Portioli F, Gagliardo R, et al. Collapse mechanism analysis of historic masonry structures subjected to lateral loads: A comparison between continuous and discrete models. *Comput Struct* 2019; 220: 14–31.

[4] D'Altri AM, de Miranda S, Castellazzi G, et al. A 3D detailed micro-model for the in-plane and out-of-plane numerical analysis of masonry panels. *Comput Struct* 2018; 206: 18–30.

[5] Dolatshahi KM, Aref AJ. Two-dimensional computational framework of meso-scale rigid and line interface elements for masonry structures. *Eng Struct* 2011; 33: 3657–3667.

[6] Minga E, Macorini L, Izzuddin BA. A 3D mesoscale damage-plasticity approach for masonry structures under cyclic loading. *Meccanica* 2018; 53: 1591–1611.

[7] Nie Y, Sheikh A, Visintin P, et al. An interfacial damage-plastic model for the simulation of masonry structures under monotonic and cyclic loadings. *Eng Fract Mech* 2022; 271: 108645.

[8] Shieh-Beygi B, Pietruszczak S. Numerical analysis of structural masonry: mesoscale approach. *Comput Struct* 2008; 86: 1958–1973.

[9] Gambarotta L, Lagomarsino S. Damage Models for the Seismic Response of Brick Masonry Shear Walls. Part Ii: The Continuum Model and Its Applications. *Earthq Eng Struct Dyn* 1997; 26: 441–462.

[10] Lourenço PB, Rots JG, Blaauwendraad J. Continuum Model for Masonry: Parameter Estimation and Validation. *J Struct Eng* 1998; 124: 642–652.

[11] Pietruszczak S, Ushaksaraei R. Description of inelastic behaviour of structural masonry. *Int J Solids Struct* 2003; 40: 4003–4019.

[12] Giambanco G, La Malfa Ribolla E, Spada A. Meshless meso-modeling of masonry in the computational homogenization framework. *Meccanica* 2018; 53: 1673–1697.

[13] Lourenço PB, Milani G, Tralli A, et al. Analysis of masonry structures: review of and recent trends in homogenization techniquesThis article is one of a selection of papers published in this Special Issue on Masonry. *Can J Civ Eng* 2007; 34: 1443–1457.

[14] Stefanou I, Sab K, Heck J-V. Three dimensional homogenization of masonry structures with building blocks of finite strength: A closed form strength domain. *Int J Solids Struct* 2015; 54: 258–270.

[15] Brasile S, Casciaro R, Formica G. Multilevel approach for brick masonry walls – Part II: On the use of equivalent continua. *Comput Methods Appl Mech Eng* 2007; 196: 4801–4810.

[16] Marfia S, Sacco E. Multiscale damage contact-friction model for periodic masonry walls. *Comput Methods Appl Mech Eng* 2012; 205–208: 189–203.

[17] Massart TJ, Peerlings RHJ, Geers MGD. An enhanced multi-scale approach for masonry wall computations with localization of damage. *Int J Numer Methods Eng* 2007; 69: 1022–1059.

[18] Petracca M, Pelà L, Rossi R, et al. Multiscale computational first order homogenization of thick shells for the analysis of out-of-plane loaded masonry walls. *Comput Methods Appl Mech Eng* 2017; 315: 273–301.

[19] Sacco E, Addessi D, Sab K. New trends in mechanics of masonry. *Meccanica* 2018; 53: 1565–1569.

[20] Addessi D, Marfia S, Sacco E, et al. *Modeling Approaches for Masonry Structures*. 2014.

[21] Lourenço PB. *Computational strategies for masonry structures*. Ph.D. Thesis, Delft University of Technology, 1997.

[22] Berto L, Saetta A, Scotta R, et al. An orthotropic damage model for masonry structures. *Int J Numer Methods Eng* 2002; 55: 127–157.

[23] Brasile S, Casciaro R, Formica G. Finite Element formulation for nonlinear analysis of masonry walls. *Comput Struct* 2010; 88: 135–143.

[24] Lourenço PB. *An orthotropic continuum model for the analysis of masonry structures*. Report 03-21-1-31-27, Delft University of Technology, 1995.

[25] Pegon P, Anthoine A. Numerical strategies for solving continuum damage problems with softening: Application to the homogenization of masonry. *Comput Struct* 1997; 64: 623–642.

[26] Pelà L, Cervera M, Roca P. An orthotropic damage model for the analysis of masonry structures. *Constr Build Mater* 2013; 41: 957–967.

[27] Toti J, Gattulli V, Sacco E. Nonlocal damage propagation in the dynamics of masonry elements. *Comput Struct* 2015; 152: 215–227.

[28] Celano T, Argiento LU, Ceroni F, et al. Literature Review of the In-Plane Behavior of Masonry Walls: Theoretical vs. Experimental Results. *Materials* 2021; 14: 3063.

[29] Drysdale RG, Khattab MM. In-plane behavior of grouted concrete masonry under biaxial tension-compression. *Struct J* 1995; 92: 653–664.

[30] Vasconcelos G, Lourenço PB. In-Plane Experimental Behavior of Stone Masonry Walls under Cyclic Loading. *J Struct Eng* 2009; 135: 1269–1277.

[31] Angelillo M, Lourenço PB, Milani G. Masonry behaviour and modelling. In: Angelillo M (ed) *Mechanics of Masonry Structures*. Vienna: Springer Vienna, pp. 1–26.

[32] Barenblatt GI. The Mathematical Theory of Equilibrium Cracks in Brittle Fracture. In: Dryden HL, von Kármán Th, Kuerti G, et al. (eds) *Advances in Applied Mechanics*. Elsevier, pp. 55–129.

[33] Page AW. Finite Element Model for Masonry. *J Struct Div* 1978; 104: 1267–1285.

[34] Giambanco G, Rizzo S, Spallino R. Numerical analysis of masonry structures via interface models. *Comput Methods Appl Mech Eng* 2001; 190: 6493–6511.

[35] Kumar N, Amirtham R, Pandey M. Plasticity based approach for failure modelling of unreinforced masonry. *Eng Struct* 2014; 80: 40–52.

[36] Lotfi HR, Shing PB. Interface model applied to fracture of masonry structures. *J Struct Eng* 1994; 120: 63–80.

[37] Lourenço PB, Rots JG. Multisurface interface model for analysis of masonry structures. *J Eng Mech* 1997; 123: 660–668.

[38] Alfano G, Sacco E. Combining interface damage and friction in a cohesive-zone model. *Int J Numer Methods Eng* 2006; 68: 542–582.

[39] Nazir S, Dhanasekar M. A non-linear interface element model for thin layer high adhesive mortared masonry. *Comput Struct* 2014; 144: 23–39.

[40] Spada A, Giambanco G, Rizzo P. Damage and plasticity at the interfaces in composite materials and structures. *Comput Methods Appl Mech Eng* 2009; 198: 3884–3901.

[41] Pietruszczak S. On homogeneous and localized deformation in water-infiltrated soils. *Int J Damage Mech* 1999; 8: 233–253.

[42] Pietruszczak ST, Mroz Z. Finite element analysis of deformation of strain-softening materials. *Int J Numer Methods Eng* 1981; 17: 327–334.

[43] Koocheki K, Pietruszczak S, Haghighat E. A computational framework for meso and macroscale analysis of structural masonry. *Int J Solids Struct* 2022; 236–237: 111342.

[44] Rudnicki JW, Rice JR. Conditions for the localization of deformation in pressure-sensitive dilatant materials. *J Mech Phys Solids* 1975; 23: 371–394.

[45] Page AW. The strength of brick masonry under biaxial tension-compression. *Int J Mason Constr* 1983; 3: 26–31.

[46] Dassault Systems. ABAQUS/Standard User's Manual, Version 6.9.

[47] Binda L, Mirabella Roberti G, Tiraboschi C, et al. Measuring masonry material properties. *Proc US Italy Workshop Guidel Seism Eval Rehabil Unreinforced Mansory Build* 1994; 3–24.

[48] Van der Pluijm R. Shear behaviour of bed joints. *6th North Am Mason Conf 6-9 June 1993 Phila Pa USA* 1993; 125–136.

[49] Chaimoon K. *Numerical simulation of fracture in unreinforced masonry*. UNSW Sydney, 2007.

[50] Atkinson RH, Amadei BP, Saeb S, et al. Response of Masonry Bed Joints in Direct Shear. *J Struct Eng* 1989; 115: 2276–2296.

[51] Raijmakers T, Vermeltfoort AT. Deformation controlled tests in masonry shear walls. *Delft Rep B-92-1156 TNO-Bouw*.

[52] Vermeltfoort AT, Raijmakers T, Janssen HJM. Shear tests on masonry walls. In: Hamid AA, Harris HG (eds) *6th North American Masonry Conference, 6-9 June 1993, Philadelphia, Pennsylvania, USA*. Technomic Publ. Co., 1993, pp. 1183–1193.

[53] Korswagen PA, Longo M, Meulman E, et al. Crack initiation and propagation in unreinforced masonry specimens subjected to repeated in-plane loading during light damage. *Bull Earthq Eng* 2019; 17: 4651–4687.

5. Closure

The conclusions to the present work as well as suggestions for potential future work are summarized in the present chapter. Given the nature of the sandwich thesis format, some overlap between the introductory sections (i.e. methodology, formulation, etc.) of the included papers is expectedly unavoidable. Since the presented papers also include detailed discussions and concluding remarks regarding the findings, advantages, and shortcomings of the proposed methodologies, the present chapter deals with a broader overview of the present work.

5.1. Concluding remarks

There are three major contributing components in the present work: mesoscale analysis, macroscale analysis, and the bridging of the two. The proposed methodology for mesoscale analysis of masonry using the constitutive law with embedded discontinuity has several advantages compared to other methodologies in masonry modelling such as the detailed models including brick-mortar interfaces. Treating the brick-mortar interface as a pre-defined plane of weakness embedded in the adjacent material, while including the ‘length scale’ parameter in the constitutive law with discontinuity, enables the use of an unstructured coarser mesh and allows for a reduction in the number of constituent properties needed for the mesoscale analysis. Using this approach proved to be an efficient tool for analysis of masonry assemblages and small-scale masonry walls, providing an accurate load-deformation response and detailed information regarding discrete location of cracked zones that are comparable to the experimental observations.

In contrast to other methodologies used for discrete fracture propagation, such as XFEM or strong discontinuity approach which require the introduction of additional degrees of freedom or changes to the shape function, the proposed formulation does not require any modifications to finite element formulation and can be implemented in commercial and open-source FEM codes via user-defined constitutive laws. Moreover, the introduction of the internal length scale parameter, which is defined based on the finite element mesh and the orientation of the crack, renders the formulation insensitive to discretization.

The proposed framework for macroscale modelling of masonry was developed based on the notion of microstructure tensor approach, describing the orientation-dependent strength properties of masonry as a continuum while maintaining anisotropic mechanical response prior to the onset of failure. The main challenges in developing a suitable constitutive model for masonry at macroscale are the identification of material parameters and the development of macrocracks that extend beyond numerous individual constituents to form failure planes that are distinguishable at the scale of large structures. The former challenge requires experiments on masonry assemblages under various loading combinations that provide extensive information on the macroscopic mechanical behaviour of masonry. Since the experimental programs at this scale are very expensive, and virtually impossible to conduct without affecting the structural integrity of existing and historical masonry buildings, numerical simulations conducted at mesoscale were used to replace the experiments and provide the data needed to assess the macroscale strength parameters.

One of the major challenges in directly using mesoscale numerical simulations for extracting macroscale constitutive parameters is the sensitivity of the results to small changes in the constituent properties (e.g., constituent size and arrangement, strength characteristics, etc.). To address this challenge, and to further reduce the number of mesoscale simulations needed for adequate characterization of macroscale constitutive parameters, artificial neural networks were developed to predict the macroscopic anisotropic elastic properties and strength characteristics based on the properties of the constituents. These neural networks were used offline and only to predict the anisotropic elastic properties and biaxial ultimate strength of masonry panels using the elastic properties and strength parameters of constituents as input. Furthermore, a separate network was trained to predict the orientation of average failure plane at macroscale based on the constituent properties and the state of stress at the onset of failure at macroscale. The trained networks were used during the macroscale finite element analyses. To verify the procedure, the results of mesoscale and macroscale simulations of lateral loading on a large-scale masonry wall were compared and good agreement between the predictions was shown.

5.2. Suggestions for future work

The proposed framework for mesoscale analysis of masonry is general in nature and is not limited to a specific arrangement of masonry constituents. Despite these capabilities, the masonry assemblages investigated in the present work only consisted of a single layer of bricks along the thickness of masonry walls. The mesoscale framework could be utilized to model masonry panels consisting of several layers of bricks in the dimension

perpendicular to the face of the wall. Furthermore, more complex types of strength degradation factors may be explored, namely a combined chemo-mechanical formulation, to account for the effect of various chemical interactions on the strength of masonry constituents (e.g., alkali-aggregate reaction, salt crystallization, etc.). With regards to the mechanical behaviour of individual constituents, nonlinear response prior to onset of fracture may be used to replace the current linear elastic model. The proposed methodology for implementing artificial neural networks as a bridge between the meso and macro scales may be improved by including various out-of-plane arrangements of constituents. A similar point can be made with respect to prediction of orientation of the failure plane at macroscale, which may include the out-of-plane fracture mechanisms as well. The approach proposed herein provides a strong framework for future models to account for the additional factors mentioned above, while being practical for analysis of existing masonry structures using a streamlined approach.